# A Free-Carrier Based Silicon on Insulator Waveguide Attenuator

**Cynthia Wilson, B. Eng.**
**McGill University, Montreal**

**September, 2001**

**A Thesis Submitted to the Faculty of Graduate Studies and Research in Partial Fulfillment of the Requirements of the Degree of Master of Engineering**

0-612-75285-2

## Abstract

All solid-state switches and attenuators are becoming increasingly popular over their mechanical counterparts. Their advantages include smaller size, no moving parts, and faster response times. The device presented here is a silicon on insulator waveguide attenuator, its operation is based on free-carrier absorption of photons. Free-carriers are provided by forward biasing a PIN diode structure integrated in a single mode rib waveguide where the guided mode propagates in the intrinsic region. The device was optimized optically using CAD tools to provide off-state losses of less than 1dB. The PIN diode electrical structure was also optimized to for a maximum power consumption of 1W at maximum attenuation. Good agreement of the theory developed was found when compared to experimental measurements of fabricated prototypes of similar structure. Fabrication and testing of devices according to the specifications arrived at in this thesis is suggested for future work.

## Résumé

Les commutateurs et les atténuateurs optiques intégrés deviennent de plus en plus populaires face à leurs équivalents opto-mécaniques. Ils sont avantageux au niveau de leur taille réduite, du fait qu'ils ne comportent pas de parties mobiles et de leur meilleur temps de réponse. Le composant présenté ici est un guide d'ondes atténuateur en silicium sur matériau isolant, dont l'opération repose sur l'absorption des photons par porteurs libres. Les porteurs libres sont obtenus par injection de courant dans une structure diode P-I-N intégrée dans un guide canal monomode où le mode se propage dans la région intrinsèque. Le composant a été optimisé avec des outils logiciels pour obtenir des pertes du composant au repos de moins de 1 dB. La structure électrique de la diode P-I-N a aussi été optimisée pour obtenir une consommation de puissance de 1 Watt au maximum d'atténuation. Un bon accord avec la théorie a été obtenu par comparaison avec des mesures expérimentales sur des prototypes de structure similaire. La fabrication et le test de composants correspondant aux spécifications fournies à la fin de cette thèse sont suggérés comme travaux futurs.

## Acknowledgments

Many people are due thanks for helping make this work possible. First and foremost, my supervisor Barrie Keyworth at JDS Uniphase Corp. for his enthusiasm in taking on this project and myself as a graduate student. His time and patience in many fruitful discussions are greatly appreciated. My other supervisor, David Plant at McGill University is also thanked for his supervision. Also appreciated were the time and effort of Heather Hnatiuk, Vincent Delisle, and Alan Hnatiw of JDS Uniphase. Without their help with the theory and proofreading I never would have finished writing.

Thanks also to my husband, Chad, for his support, encouragement and understanding when the end was far from sight. I also owe thanks to my mother and father for constantly reminding me to finish writing my thesis or I would pay tuition for the rest of my life. And a scratch behind the ears for my cats, Clemens and Pee Wee, for hanging out with me those late nights when I was up writing.

## Table of Contents

# 1 Introduction

## *1.1 Variable Optical Attenuators and Optical Communication Systems*

Communications over optical fibres has become the preferred method for many applications such as data, voice, and video transfer over long and short area networks. Optical communications offers tremendous transmission capacity, long distances between repeaters, and immunity to electromagnetic interference. As the number of channels increase and loss introduced by components decrease, attenuators are becoming a practical necessity in controlling excess power in communication systems. Variable attenuators are also essential in controlling the non-linear behavior of other components such as fibre amplifiers. Due to the exponential increase in the bandwidth and usage of optical communication systems [1], the demand for faster, smaller, lower loss, lower cost components is increasing. With the improvements to semiconductor and solid-state devices, attenuator technologies are no longer limited to traditional bulk optics. High performance attenuators are now possible by expanding the applications of these semiconductor devices from conventional sources and modulators to attenuators.

## *1.2 Applications of Variable Optical Attenuators*

There are numerous applications of variable attenuators in optical communications systems, ranging from network analysis to power control. Variable attenuators are used in three main areas; wavelength division multiplexed (WDM) optical networks, test and measurement instrumentation, and optical power control. Each application requires different performance characteristics from the variable attenuator, such as wavelength flatness, optical power dissipation, and/or speed. Figure 1-1 shows several applications of variable optical attenuators in a dense wavelength division multiplexed (DWDM) network.

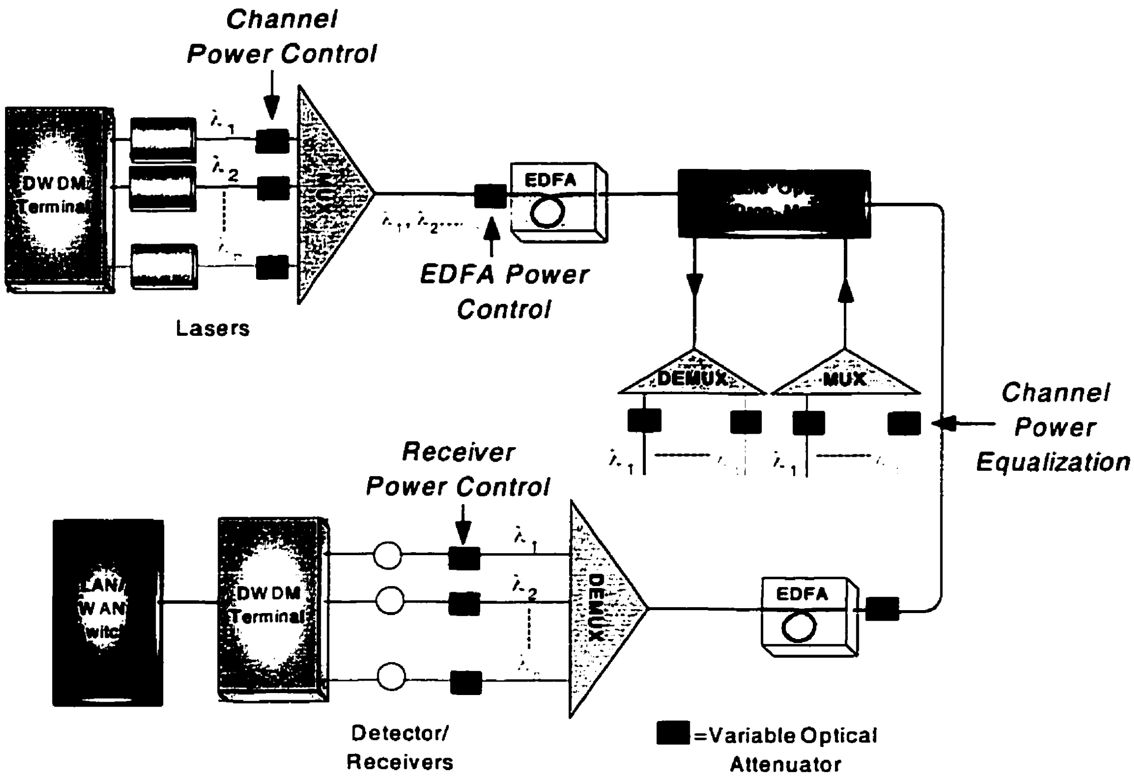


**Figure 1-1: Variable optical attenuators in a DWDM network. Variable attenuators are used for power control after a bank of lasers and before an erbium doped fibre amplifier (EDFA). Channel power equalization is performed at demultiplexing and multiplexing units (MUX and DEMUX). Attenuators are used before receivers to avoid saturation. The number of attenuators and where they are used in a system depends on many network parameters such as the power budget and component specifications.**

### 1.2.1 Wavelength Division Multiplexed Optical Networks

Fibre-optic long haul trunk networks are faced with the dilemma of accumulated losses and signal degradation due the inherent properties of optical fibres and components. Until the early 1990s, all amplification was performed electronically. Electronic repeaters first translate the optical signal to an electronic one, retime, reshape and regenerate these signals electronically, and subsequently transmit them optically. With the advent of Erbium Doped Fibre Amplifiers (EDFAs), all-optical broadband amplification and thus higher operating speeds, lower cost and better reliability could be realized. Unfortunately, the EDFA wavelength spectrum is not flat, which has a detrimental effect on long distance WDM-based optical networks where many such devices are cascaded. Channels lying at a minimum in the EDFA spectrum will not be amplified the same amount as those at a maximum, thus each channel will have different gain. Each time the signal passes through an EDFA, the power variation between channels will increase. Optical attenuators are needed in WDM-based networks employing EDFAs for dynamic power equalization since the gain of EDFAs changes with age and input power. Arrays of attenuators are used with EDFAs to attenuate those channels that fall in the higher amplification range of the EDFA spectrum. Figure 1-2 shows the EDFA gain spectrum after 5 passes and a 16 channel demultiplexing unit spectrum after power equalization [2].

Attenuators used in power equalization should be waveloength insensitive, have efficient power dissipation properties and small size. Wavelength insensitivity is an important characteristic in WDM applications since ideally, the same attenuator is used for each channel at the front end of an EDFA without special adjustment with respect to wavelength. These attenuators could be used to dissipate high power levels thus they should perform linearly over a large power range. Small size is also an important factor since the attenuators must be easily fabricated into arrays for multi-wavelength systems.

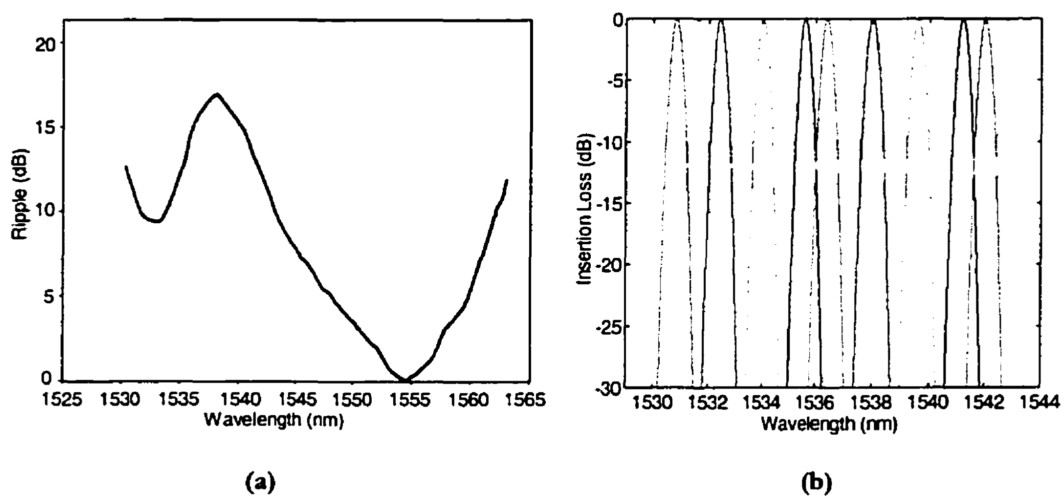


**Figure 1-2. (a) Accumulated ripple of a typical EDFA gain spectra after 5 passes [2]. (b) 16 Channel demultiplexing unit spectra with equal channel power [2]. Attenuators are needed to equalize the power level across every channel in the demux after passing through the amplifier. After passing through 5 EDFAs, the differential channel loss could reach as high as 17dB.**

## 1.2.2 Test and Measurement Instrumentation

Optical attenuators are also used in the testing and analysis of other optical components. In production testing and quality assurance, attenuators are used in verifying the operating range of components by variably attenuating the input optical power level of the device under testing. The linearity and dynamic range of several different components such as photodetectors, power meters, and modulators can be determined.

Another important application of variable optical attenuators is in network analysis and simulations. A variable attenuator can be inserted into a newly installed link to verify the performance monitoring messages generated by the receiver. Other system performance metrics such as bit-error-rate (BER), system loss, and receiver sensitivity analysis can be tested by using variable attenuators in network analysis equipment to attenuate the power level entering a system.

Attenuators used in testing the characteristics of other devices and analyzing network performance must be highly linear in their attenuation characteristic to keep the same resolution at different attenuation levels and have a very large dynamic range. This is essential to ensure any non-ideal behavior is a result of the device or system under testing and not the attenuator.

### 1.2.3 Optical Power Control

Optical fibre systems are being used increasingly in short distance applications such as local area networks, central office switching, and cable television. Light sources and optical fibres, however, have been developed to maximize throughput power in order to achieve long distance communications. In these shorter distance applications, variable attenuators are needed at the input of receivers to control excessive power to protect the receivers (which have a limited dynamic range) from becoming saturated.

Optical power level control is also required at the output of laser sources. If the power level of a laser is beyond the power budget of a system, it must be attenuated accordingly. It is important to use a variable attenuator in this instance because over the laser's lifetime, its power level will decrease and the attenuation level of the output power must be decreased as well. Furthermore, it is imperative that the insertion loss of the attenuator in the off state must be as low as possible when it is not needed to attenuate the laser power. In a multi-wavelength system, an array of variable attenuators can be inserted directly at the output of an array of laser sources in order to adjust or provide stable power levels to each channel.

To avoid saturation and non-linear behavior, an attenuator must be placed at the input of an EDFA to ensure that the input power is kept below a certain level such that the EDFA will not reach saturation. For example, if the maximum output level of an EDFA is 25dBm and its maximum gain is 20dB, an input signal of 10dBm would need to be attenuated by 5dB to avoid saturation. In addition to static power control, dynamic control of the average input power may be necessary if many WDM channels are added or dropped. For example, a system of 16 channels would have a higher aggregate power than 8 channels, thus power control is required.

Attenuators used in optical power control must not only be able to attenuate high power levels but also be able to dissipate the unwanted power quickly and efficiently without affecting its performance. For example, an attenuator that increases in temperature with the amount of optical power absorbed would not be a good choice for this application since temperature effects could lead to non-linear behavior. A better choice of attenuator for optical power control is one that reflects or guides away the unwanted light such that its behavior is independent of the input power level. Speed is also an important characteristic that attenuators must possess in optical power control, especially in systems where channels are added and dropped frequently. The attenuator used to protect the EDFA from gain saturation must be able to respond quickly to increasing power levels entering the EDFA as channels are added. Attenuators used to attenuate excess power from laser sources and protect receivers from saturation in short-distance networks must be able to react promptly if there is a sudden change in the transmitter laser's power level or change in the total power level of the system.

In all of the applications discussed, polarization insensitivity is also an important feature of an optical attenuator. The attenuator must not introduce polarization dependence with attenuation. If this were the case, polarization mode dispersion would be introduced into the system and will lead to pulse spreading.

## *1.3 Variable Optical Attenuator Technologies*

There are many different physical effects that can be used to create optical attenuation. They can be classified into four main categories; opto-mechanic, opto-electronic, thermo-optic, and liquid crystal. Furthermore, these physical effects can be implemented into many different architectures to form attenuators. The main attenuator architectures are guiding, reflecting, interfering and absorbing. Guiding and reflecting attenuators guide or reflect away the unwanted light. Interfering attenuators use destructive interference to decrease the optical power. Absorbing attenuators use a physical absorbing effect to attenuate the unwanted light. These technologies are also used in the production of switches and modulators, however any switch or modulator can be used as an attenuator. Figure 1-3 shows where free-carrier absorption is positioned with respect to other physical effects.

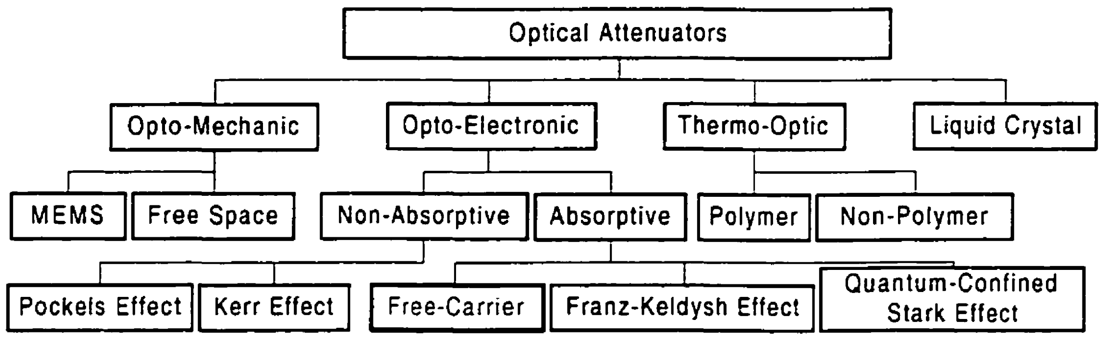


**Figure 1-3: Possible technologies and phenomena which can be exploited to fabricate variable optical attenuators. The free-carrier effect is an absorptive type of opto-electronic variable optical attenuator.**

### 1.3.1 Opto-Mechanical Attenuators

Opto-Mechanical attenuators are devices using either bulk optic components or micro-electro-mechanical systems (MEMS). Bulk optic attenuators may use components such as lenses, mirrors, variable mirrors, or prisms to block or re-direct a beam of light. These types of attenuators are usually controlled manually by adjusting a set screw or turning a knob. Some bulk optic attenuators use motors to move the attenuation mechanism, thus employing electronic control. Bulk optic attenuators employ reflecting or absorbing architectures. The light is either reflected away from the output path by a movable mirror or prism or absorbed by a filter which can be moved in and out of the beam. A commercially available bulk optic voltage controlled attenuator by JDS Uniphase [3] has a 30dB attenuation range, 0.1dB resolution, an operating wavelength range of 1525 to 1575nm, insertion loss of 0.6dB, wavelength flatness of 0.2dB, 100ms response speed, and polarization dependent loss of 0.2dB.

This is a reflection type attenuator, which uses a voltage-controlled stepper motor to move a mirror.

MEMS attenuators are similar in operation to bulk optic attenuators, with the main difference being that the components are integrated onto the same chip and are usually on the order of tens to hundreds of microns in size. Attenuation of the optical signal is attained in response to an applied voltage when a mirror flips up or a beam blocker moves due to an electrostatic force. Figure 1-4 illustrates one type of MEMS optical attenuator reported by Marxer et al [4]. This device has an insertion loss of 1.5dB, a 5ms response time, a maximum attenuation level of 57dB, and a maximum applied voltage of 32V. MEMS attenuators offer the advantages of speed and ease of assembly over bulk optic attenuators due to the small size and integration of the components used. Disadvantages of MEMS devices include high initial costs, low resistance to shocks and vibrations, and a high level of manufacturing difficulty since precise, complex fabrication techniques are required.

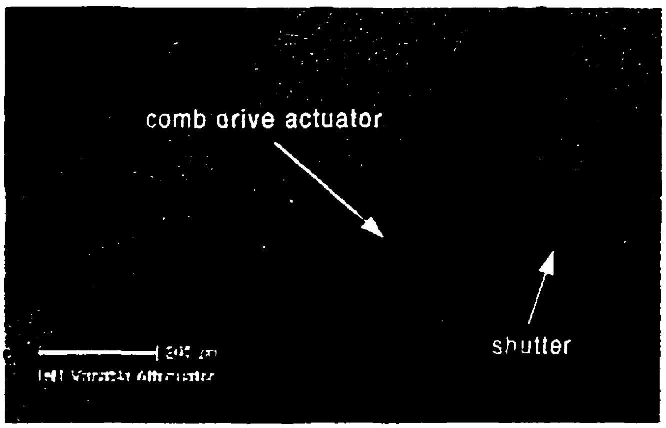


**Figure 1-4: SEM Photograph of a micromechanical variable actuator chip [4]. An electrostatic comb drive actuator is used to drive the shutter into the optical path. Attenuation can be varied with the shutter position.**

### 1.3.2 Opto-Electronic Attenuators

Attenuators using opto-electronic effects are very fast, efficient, and reliable since they have no moving parts and usually only require a small amount of power. Opto-electronic attenuators are separated into two groups, polarizing and absorbing. Either the Kerr effect or the Pockels effect can be used to make a polarizing attenuator in semiconductor materials that normally have isotropic optical properties.

In the Kerr effect, an electric field applied across a crystal in a direction transverse to a light beam propagating through it will induce birefringence, linearly proportional to the square of the applied electric field [5]. The semiconductor will then become biaxial. If the electric field vector of a polarized beam of light propagating through the crystal is inclined at 45° to the applied electric field, the light will emerge elliptically polarized. The Pockels effect can be used in a similar fashion. In semiconductors which are normally optically anisotropic, the application of an electric field will induce biaxial birefringence, linearly proportional applied electric field . When an electric field is applied along one direction, the index of refraction of the transverse plane is altered by an amount proportional to the applied electric field. Again, linearly polarized light will emerge elliptically polarized.

An interferometer architecture can be employed in polarizing electro-optic attenuators since a beam of light passing through a material exhibiting the Pockels and/or Kerr effects will experience phase change. Lithium niobate has large electro-optic coefficients and is a popular material used for Mach-Zehnder waveguide modulators. When a voltage is applied to one arm of the modulator, the light propagating through it will experience a phase change and cause constructive or destructive interference upon re-combining with the light from the other arm, depending on the relative phase between the two signal paths. With the appropriate applied voltage the output signal intensity can be varied sinusoidally. The main disadvantage with this approach is that the attenuation is both a non-linear and periodic function of the applied voltage as the relative phase of the light propagating in the two arms oscillates between 0 and $\pi$. Noguchi et al [6] has reported a Lithium Niobate Mach-Zehnder broadband modulator with a half-wave drive voltage (voltage of maximum attenuation) of 5.1V, a modulation bandwidth of 70GHz, an insertion loss of 5.6dB, an extinction ratio of 20dB, and an operational wavelength of 1550nm. The configuration of this device is shown in Figure 1-5.

Free-carrier absorption, the Franz-Keldysh effect, and the quantum confined Stark effect can be used to create absorbing opto-electronic variable attenuators. Free-carrier absorption, the focus of this work, is the process whereby incident photons are absorbed by free-carriers in the conduction band of a semiconductor [5].

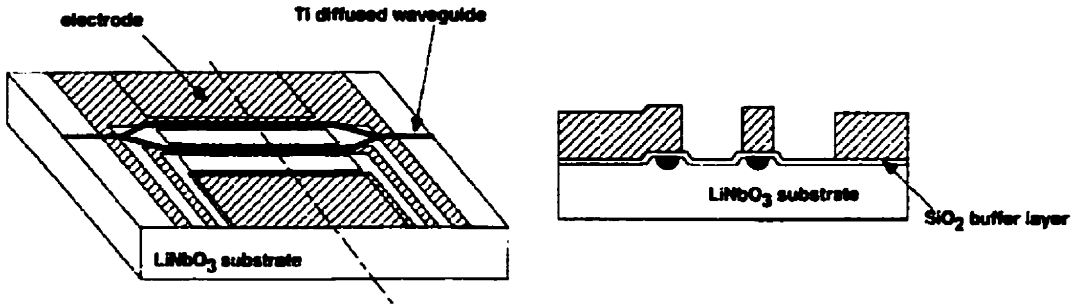


**Figure 1-5: Configuration of a Lithium Niobate Mach-Zehnder modulator [6]. The phase of the optical wave traveling through one arm is altered by application of a voltage to the electrode which induces a relative change in the extraordinary and ordinary refractive indices of the crystal. The waveguide is created by diffusing titanium into the lithium niobate crystal.**

By injecting free-carriers into a material, variable attenuation can be achieved. A free-carrier absorptive intensity modulator has been reported by Zhao et al [7]. This device has an insertion loss of 5.2dB, a modulation depth of 18dB, and a response time of 160ns. The configuration of this device is shown in Figure 1-6.

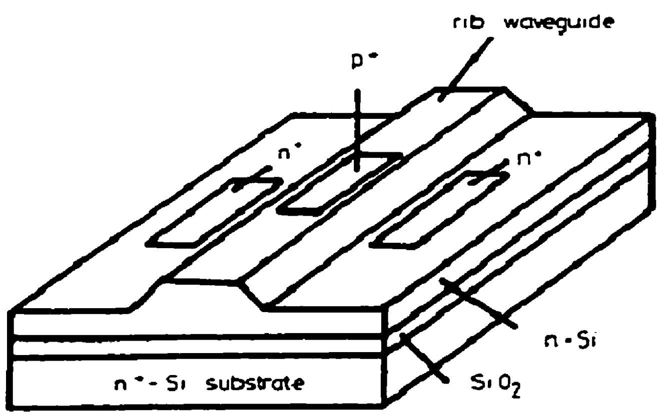


**Figure 1-6: Silicon on insulator optical intensity modulator [7]. When the p⁺n junction is forward biased, holes and electrons will enter the waveguide region and absorb light energy propagating through that section.**

The free carrier effect also causes a change in the material's refractive index. This effect has been exploited by Zhao et al [8] who reported a Mach-Zehnder interferometer operating at a wavelength of 1.3μm, with an insertion loss of 6.4dB, an operating voltage of 0.95V, a response time of 0.2ps, and a modulation depth of 35dB. This device operates similarly to the Mach-Zehnder in Figure 1-5, however the change in refractive index is caused by the free-carrier effect. The change in index is $\Delta n=5\times10^{-}$

[3] for an injected carrier density of $\Delta N=1x10^{18}$. The free-carriers arise from forward biasing a $p^+n$ junction in one arm, similar to Figure 1-6. Another device exploiting the refractive index change is a 1x2 switch reported by Liu et al [9]. The configuration of this device is shown in Figure 1-7. A PIN diode is integrated into each arm; when one of the diodes is forward biased, the refractive index will decrease and the waveguide will be in a cut-off regime. The light will not propagate through this arm since the waveguide no longer supports a guided mode at the operating wavelength. Consequently, the mode will propagate through the other arm. This device has an insertion loss of 8.2dB, a response time of 0.2ps, and 22.3dB extinction with 290mA of injected current with an operating wavelength of 1.3μm.

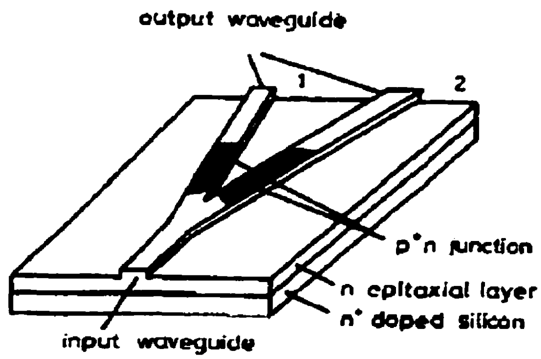


**Figure 1-7: Silicon 1x2 optical switch [9]. If the p⁺n junction of branch 2 is forward biased, free-carriers will cause a decrease in the index due to the free-carrier effect. Light will propagate through branch 1 as a result since it has a higher index.**

The Franz-Keldysh effect creates an absorptive material by applying an electric field to a direct-gap semiconductor. This decreases the effective band gap of the semiconductor and increases the overlap between the electron and hole wave functions, allowing band-to-band transitions of electrons with absorption of photons. Absorption of longer wavelength photons can be varied with the magnitude of the applied electric field. An attenuator integrated with a photodetector using this effect has been proposed by Yokouchi et al [10]. By applying a voltage to the GaInAsP waveguide, attenuation for a given wavelength is achieved. This device, shown in Figure 1-8, had an attenuation range of 11dB with an applied voltage of 32V.

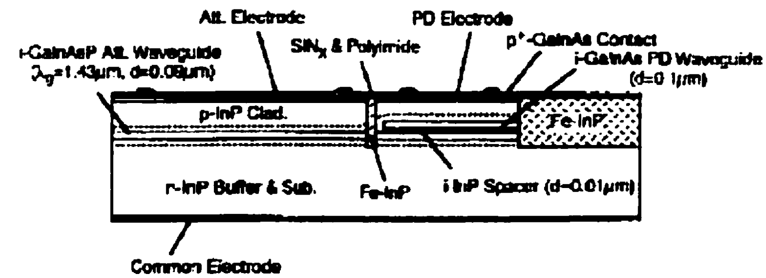


**Figure 1-8: Attenuator integrated photodetector [10]. The aim of this device was to reduce distortion at the receiver due to high input power. Saturation can be avoided through electrical feedback from the photodetector. Attenuation is achieved by varying the applied voltage across the GaInAsP layer.**

The quantum-confined Stark effect is also an absorptive process [5]. In semiconductor multi-quantum well (MQW) structures, strong absorption peaks due to excitons can be observed. An exciton is a free hole and a free electron pair experiencing a coulombic attraction. In direct-gap materials, excitons can be formed by absorbing the energy of photons entering the material, thus contributing a component to the absorption coefficient. When an electric field is applied perpendicular to the quantum well layers, the potential well in which the exciton is trapped becomes asymmetric. One of the sides is lowered, and thus it is easier to ionize the excitonic pair. Ionization of the pair occurs due to the absorption of energy from an incident photon. The excitonic peak remains even at very high applied fields because the walls of the quantum well prevent the electron-hole pair of the exciton from being pulled apart by the electric field. As a result, the excitonic absorption peak can be shifted to longer wavelengths depending on the strength of the applied electric field. This shift in the exciton absorption peak is known as the Stark shift, shown in Figure 1-9. This effect can be exploited to make a modulator in a quantum well structure by varying an applied electric field. An electroabsorption modulator with a MQW structure has been reported by Yoshino et al [11], having an insertion loss of 5dB, modulation speed of 46GHz, and an extinction ratio of 50dB.

Electro-optic absorptive attenuators are more attractive than bulk optic or polarizing attenuators because they are fast, compact, have no moving parts, and the attenuation varies linearly with applied current or electric field. However, these types of attenuators exhibit wavelength dependant absorption, which may be an unwanted characteristic when used for channel power equalization in a WDM system and higher coupling losses due to restricted waveguide structures.

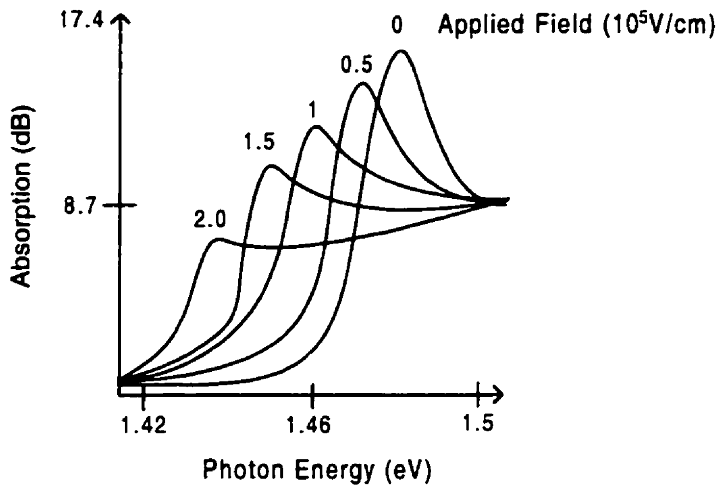


**Figure 1-9: Absorption spectra for electric fields perpendicular to the QW layer plane of a 94Å wide GaAs QW [11]. The exciton absorption peak shifts to lower photon energies as the applied field is increased.**

### 1.3.3 Thermo-Optic Attenuators

Some materials exhibit a considerable change in index when heated, due to lattice expansion in semiconductors or density changes in polymers. As the temperature of a semiconductor increases, the lattice expands and the oscillations of the atoms about their equilibrium lattice points increase. This leads to a change in the energy gap and broadening of the energy levels, which subsequently leads to a change in the material's refractive index [12]. If a polymer is heated, its density will decrease and cause a decrease in its refractive index.

A Mach-Zehnder thermo-optic interferometric switch fabricated in silica-on-silicon has been reported by Syahriar et al [12], shown in Figure 1-10. This device has an insertion loss of 2dB, extinction ratio of 10dB, polarization dependent loss of 1dB, switching time of 0.5ms, and a power consumption of 0.5W, optimized for a wavelength of 1.523μm. An increase in refractive index ($\Delta n=5\times10^{-3}$) is induced by heating one arm of the Mach-Zehnder. A polymer digital optical switch has been reported by Moosburger [13], with an insertion loss of 3dB, an extinction ration of 20dB, power consumption of 200mW, optimized for a wavelength of 1.55um. The configuration of this switch is shown in Figure 1-11. By heating one branch of the 1x2 switch, a decrease in the refractive index causes the optical mode to propagate through the opposite branch with a higher index, and switching is achieved. This type of switch could be used as a guiding attenuator.

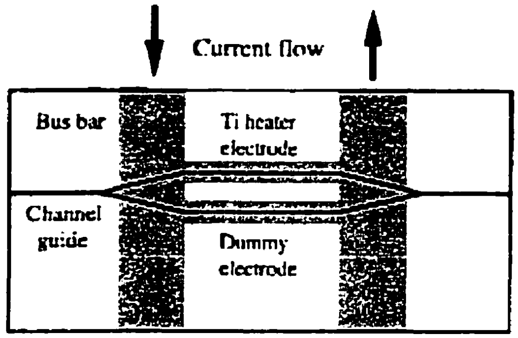


**Figure 1-10: Mach-Zehnder silica thermo-optic switch [12]. When a current is applied to the device, the heater electrode heats one arm of the Mach-Zehnder and increases its refractive index. By turning the current flow on and off, the device can be switched between the on and off state.**

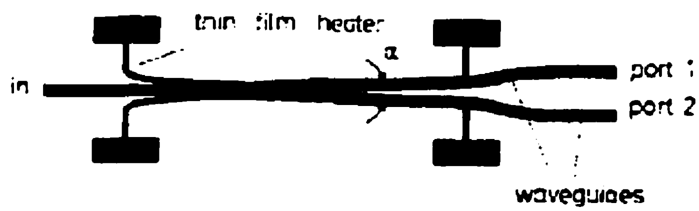


**Figure 1-11: Polymer digital optical switch [13]. When heat is applied to one of the branches, the fundamental mode will be pulled over to the other branch. The refractive index decreases as the temperature of the polymer increases.**

Thermo-optic attenuators are slower than absorbing or polarizing attenuators, typically in the millisecond range, because the response time is limited by the material's heat transfer properties. However, thermo-optic attenuators are desirable for applications which require attenuation of high power levels since guiding attenuators are possible. Power consumption of thermo-optic polymer devices is lower than semiconductor thermo-optic devices due to larger thermo-optic coefficients, thus larger index changes are possible. The thermo-optic effect is also invariant of the polarization of the optical signal. However, the stability of many polymers is of concern, especially at elevated temperatures and humidity levels due to low glass transition temperatures and high water absorption rates.

### 1.3.4 Liquid Crystal Attenuators

Liquid Crystals can also be used to fabricate variable optical attenuators. These often use liquid crystal cells which are thin layers of twisted nematic liquid crystal placed between two parallel plates. Transparent electrodes applied to both sides of the cell allow for control of the crystals. With no electric field applied to the cell, the polarization state will be rotated by the twisted crystals by 90°. When an electric field is applied to the cell, electric dipoles are induced and the resultant electric forces exert torque on the molecules, causing them to untwist. The polarization state of the light propagating through the cell will remain unchanged. A 1x8 switch composed of liquid crystal cells and birefringent crystals has been reported by Noguchi [14], exhibiting insertion losses of 6.8dB, PDL of 0.1dB, and crosstalk of 57dB. The configuration of this device is shown in Figure 1-12. The liquid crystal cells and calcite crystals are cascaded along the collimated optical beam path. Each liquid crystal modulator switches the polarization angle of the linearly polarized beam, causing the beam path to change as it propagates through the following crystal. At the end of the switch, a beam router consisting of two oppositely oriented calcite crystals recombines the eight extraordinary and ordinary rays to form a polarization independent switch. A 1x2 version of this switch could be used as an attenuator by varying the electric field applied to the liquid crystal cell. This would vary the amount of light re-combined at the beam router achieving variable attenuation.

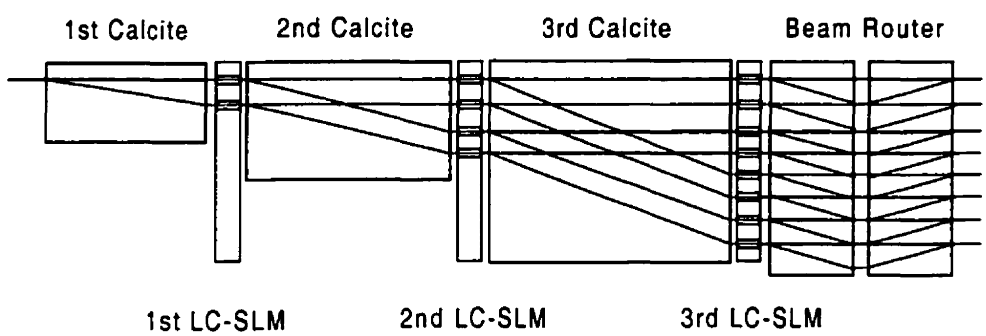


**Figure 1-12: 1x8 polarization insensitive liquid crystal switch [14]. Each liquid crystal spatial light modulator array (LC-SLM) switches the polarization angle of the beam, thus its path changes as it propagates through the next calcite crystal. A beam router at the end of the switch combines the extraordinary and ordinary rays to provide polarization independent switching.**

Liquid crystal switches would be a good choice for an attenuator used in high power applications since it can guide the unwanted light away. They are wavelength insensitive and have no moving parts. The response time of these devices is the response time of the liquid crystal cells, which is usually on the order of 50μs. Possible drawbacks of liquid crystal devices are high power consumption, reliability, and a limited operating temperature range.

Characteristics of all attenuator technologies discussed in section 1.3 are summarized in Table 1.

**Table 1: Comparison of variable attenuator technologies.**

| *Author* | *Technology* | *Architecture* | *PDL (dB)* | *IL (dB)* | *Speed (s)* | *Op. Temp. Range (°C)* | *Op. λ Range (nm)* | *Power Cons. (W)* | *Extinction (dB)* |
|---|---|---|---|---|---|---|---|---|---|
| JDSU [3] | Bulk | Reflecting | 0.2 | 0.6 | 100m | -5-70 | 1525-1575 | -- | 30 |
| Marxer [4] | MEMS | Reflecting | -- | 1.5 | 5m | -- | -- | -- | 57 |
| Noguchi [6] | Polarizing | Interfering | -- | 5.6 | 5p | 10-65 | -- | -- | 20 |
| Zhao [7] | Free Carrier | Absorbing | -- | 5.2 | 160n | -- | -- | -- | 18 |
| Zhao [8] | Free Carrier | Interfering | -- | 6.4 | 0.2p | -- | -- | -- | 35 |
| Liu [9] | Free Carrier | Guiding | -- | 8.2 | 0.2p | -- | -- | -- | 22 |
| Yokouchi [10] | Franz-Keldysh | Absorbing | -- | -- | -- | -- | -- | -- | 11 |
| Yoshino [11] | QCSE | Absorbing | -- | 5.0 | 7.6p | 0-60 | 1530-1570 | 50μ | 50 |
| Syahriar [12] | Thermo-Optic | Interfering | 1.0 | 2.0 | 0.5m | -- | -- | 0.5 | 10 |
| Moosburger [13] | Thermo-Optic | Guiding | -- | 3.0 | -- | -- | -- | 0.2 | 20 |
| Noguchi [14] | Liquid Crystal | Guiding | 0.1 | 6.8 | -- | -- | -- | -- | 57 |

## *1.4 History of Silicon Free-Carrier Based Devices*

There have been several types of free-carrier injection-based waveguide attenuators, modulators, and switches fabricated in silicon. Some use the free-carrier dispersion or index change of silicon, others use the free-carrier absorption properties of free-carriers in silicon, and some use both effects to their advantage.

The basic devices reported have been junction-based straight rib waveguides in which the optical mode propagates perpendicular or parallel to the direction of free-carrier injection. The earliest of these devices was reported in 1984 by Lorenzo et al [15], who used the refractive index change for phase modulation in an elongated diode on a ridge waveguide. Shortly afterwards Friedman et al [16] also used the electro-refractive effect to produce an improved phase modulator in an elongated transistor structure offering more degrees of freedom in its design and operation than Lorenzo's structure. Hemenway et al [17] reported a modulator for use in 1.3μm fibre-optic interconnects. This device was a forward biased horizontal PIN diode in a ridge waveguide which used free-carrier dispersion to diffract the optical beam. The first free-carrier based silicon Mach-Zehnder interferometer was reported by Treyz et al [18]. Modulation of the optical signal was achieved using free-carrier dispersion in forward biased vertical PIN diodes on the arms of the MZ in a rib waveguide structure. Treyz et al [19] also reported an absorption modulator using a PIN diode integrated into a rib waveguide structure.

Up to this point, vertical confinement of the optical mode was achieved by using a heavily doped epilayer in between the silicon substrate and waveguide. Three years later, Tang et al [20] and Zhao et al [21] reported a phase modulator and Mach-Zehnder interferometer, respectively, using free-carrier absorption. These devices were also vertical PIN diodes in rib waveguides, but this time a new method was used for vertical confinement, Silicon on Insulator (SOI), which uses a thin layer of silica in place of the heavily-doped epilayer. This new technology allowed for lower losses since the optical mode does not incur extra losses due to free-carrier absorption in the epilayer. Since then, several novel free-carrier modulators have been reported. Cutolo et al [22] reported a three-terminal device which can be used either as an intensity or phase modulator. Simulations of a novel Fabry-Perot intensity modulator which used free-carrier dispersion to modulate the reflectivity of a grating structure has been reported by Vonsovici et al [23].

The effect of free-carrier dispersion has also been used to realize several different types of switches. The first switching device in silicon using free-carrier dispersion was reported by Lorenzo et al [24]. A 2X2 PIN structure with confinement provided by a heavily doped epilayer provided the first evidence of switching at a wavelength of 1.3μm. Liu et al [25] reported a Y-branch 1 x 2 digital optical switch with vertical diodes in each branch. A four-port total internal reflection switch has also been reported by Liu et al [26], which uses free-carrier dispersion to re-direct light traveling through a ridge waveguide. Both of Liu's devices used a heavily doped epilayer to provide vertical confinement of the optical mode. Similar devices were described by Zhao et al [27],[28]using SOI technology.

## *1.5 Thesis Organization*

This thesis is organized into three main chapters: device design, experimental devices and results, and optimal device configuration. Chapter 2 describes the theoretical device design and is divided into three main sections. The first section briefly introduces the overall operation of the device, and the second and third describe in detail the optical and electrical theory and design. Chapter 3 discusses the experimental setup used to test devices and compares theoretical results from the previous section with experimental results. Chapter 4 concludes with a summary of all results, compares the resulting design with other commercially available variable attenuators, and provides suggestions for improvements and future work.

***References***


[1] J. Gowar, "Optical communication Systems", Prentice Hall, ISBN: 0136387276, 1993, pp. 16-17.

[2] Courtesy JDS Uniphase Corporation Fibreoptics Products Group, 3000 Merivale Road, Nepean, Ontario, Canada, K2G 5W8.

[3] JDS Uniphase VCB Series Voltage-Controlled Optical Attenuators

[4] C. Marxer, P. Griss, N. F. de Rooij, "A Variable Optical Attenuator Based on Silicon Micromechanics," IEEE Photonics Technology Letters, vol. 11, no. 2, pp. 233-235, Feb. 1999.

[5] J. Pankove, "Optical Processes in Semiconductors," Dover Publications, ISBN: 0486602753, 1972, pp. 34-86.

[6] K. Noguchi, O. Mitomi, H. Miyazawa, "Millimeter-Wave Ti:LiNbO3 Optical Modulators," IEEE Journal of Lightwave Technology, vol. 16, no. 4, pp. 615-619, Apr. 1998.

[7] C. Z. Zhao, E. K. Liu, G. Z. Li, L. Guo, "Silicon on Insulator Optical Intensity Modulator based on Waveguide Vanishing Effect," IEE Electronics Letters, vol. 32 issue 18, pp. 1667, Aug. 29 1996.

[8] C. Z. Zhao, G. Z. Li, E. K. Liu, Y. Gao, X. D. Liu, "Silicon on Insulator Mach-Zehnder Waveguide Interferometers Operating at 1.3μm," Applied Physics Letters vol. 67, no. 17, pp. 2448-2449, Oct. 23, 1995.

[9] Liu, "Silicon 1X2 Digital Optical Switch Using Plasma Dispersion," IEEE Electronics Letters, pp. 130-131, vol. 30, issue 2, Jan. 20, 1994.

[10] Yokouchi, "Attenuator Integrated Waveguide Photodetectors (AIPD) With Variable Sensitivity Range," IEEE Photonics Technology Letters vol. 19, no. 6, pp. 66-69, June 1998.

[11] K. Yoshino, T. Takeshita, I. Kotaka, S. Kondo, Y. Noguchi, R. Iga, K. Wakita, "Compact and Stable Electroabsorption Optical Modulator Modules," IEEE Journal of Lightwave Technology, vol. 17, no. 9, pp. 1700-1707, Sept. 1999.

[12] A. Syrahriar, R. Syms, T. Tate, "Thermooptic Interferometric Switches Fabricated by Electron Beam Irradiation of Silica on Silicon," IEEE Journal of Lightwave Technology, vol. 16 no. 5, pp. 841-846, May 1998.

[13] R. Moosburger, G. Fishbeck, C. Kostrzewa, K. Petermann, "Digital Optical Switch Based on Oversized Polymer Rib Waveguides," IEE Electronics Letters, vol. 32, issue 6 , pp. 544 –545, 14 Mar. 1996.

[14] K. Noguchi, "Optical Free-Space Multi-Channel Switches Composed of Liquid-Crystal Light-Modulator Arrays and Birefringent Crystals," IEEE Journal of Lightwave Technology, vol. 16, no. 8, pp. 1473-1481, Aug. 1998.

[15] J. Lorenzo, R. Soref, "Topical Meeting on Photonic Switching Technical Digest Series," vol. 13, pp. 65-67, 1986.

[16] L. Friedman, R. Soref, J. Lorenzo, "Silicon Double-Injection Electro-Optic Modulator With Junction Gate Control," Journal of Applied Physics, vol. 63 no. 6, pp. 1831-1839, 15 Mar.1988.

[17] B. R. Hemenway, O. Solgarrd, D. Bloom, "All-Silicon Integrated Optical Modulator for 1.3μm Fibre-Optic Interconnects," Applied Physics Letters, vol. 55, no. 4, pp 349-350, 24 Jul. 1989.

[18] G. Treyz, P. May, J. Halbout, "Silicon Mach--Zehnder Waveguide Interferometers Based on the Plasma Dispersion Effect, Applied Physics Letters, vol. 59, issue 7, pp. 771-773, 12 Aug. 1991.

[19] G. Treyz, P. May, "Silicon Optical Modulators at 1.3μm Based on Free-Carrier Absorption," IEEE Electron Device Letters, vol. 12, no. 6, June 1991.

[20] C. Tang, G. Reed, "Highly Efficient Optical Phase Modulator in SOI Waveguides," Electronics Letters, vol. 31, no. 6, pp. 451-452, 16 Mar. 1995.

[21] C. Zhao, E. Liu, G. Li, L. Guo, "Silicon-On-Insulator Optical Intensity Modulator Based On Waveguide-Vanishing Effect," Electronics Letters , vol. 32, issue 18, pp. 1667-1668, 29 Aug. 1996.

[22] A. Cutolo, M. Iodice, P. Spirito, L. Zeni, "Silicon Electro-Optic Modulator Based on a Three Terminal Device Integrated in a Low-Loss Single Mode SOI Waveguide," IEEE Journal of Lightwave Technology, vol. 15, no. 3, pp. 505-518, Mar. 1997.

[23] A. Vonsovici, R. Orobtchouk, A. Koster, "Numerical Simulation of a Silicon-on-Insulator Waveguide Fabry-Perot Interferometer for Intensity Light Modulators at 1.3μm," IEEE Journal of Lightwave Technology, vol. 15, no. 11, pp. 2124-2129, Nov. 1997.

[24] J. Lorenzo, R. Soref, "1.3 μm Electro-Optic Silicon Switch," Applied Physics Letters, vol. 51, issue 1, pp. 6-8, 6 Jul. 1987.

[25] Y. Liu, E. Liu, G. Li, S. Zhang, J. Luo, F. Zhou, M. Cheng, B. Li, H. Ge, "Novel Silicon Waveguide Switch Based on Total Internal Reflection," Applied Physics Letters, vol. 64, issue 16, pp. 2079-2080, 18 Apr. 1994.

[26] Y. Liu, E. Liu, S. Zhang, G. Li, J. Luo, " Silicon 1x2 Digital Optical Switch Using Plasma Dispersion," Electronics Letters, vol. 30, issue 2 , pp. 130 –131, 20 Jan. 1994.

[27] C. Zhao, E. Liu, G. Li, Y. Gao, C. Guo, "Zero-Gap Directional Coupler Switch Integrated Into a Silicon-on-Insulator for 1.3- μm operation," Optics Letters, vol. 21, issue 20, pp. 1664-1666, Oct. 1996.

[28] C. Zhao, A. Chen, E. Liu, G. Li, "Silicon-On-Insulator Asymmetric Optical Switch Based on Total Internal Reflection," IEEE Photonics Technology Letters, vol. 9, no. 8, Aug. 1997.

# 2 Device Design

## *2.1 Overview of Device Operation*

The attenuator developed for this thesis uses the free-carrier absorption effect to attenuate an optical signal propagating through it. A PIN diode was integrated into a rib waveguide structure, thereby allowing continuously adjustable attenuation. A silicon on insulator (SOI) structure was used, which is a crystalline silicon layer overtop of a thin layer of silica on a silicon wafer. A cladding layer of SiO2 was applied over the core for protection and additional confinement. Vertical confinement was provided by the large difference in refractive index between the silicon waveguide and the silica layers. A rib waveguide structure was used to minimize input and output coupling losses while ensuring single mode operation. Absorption of the optical signal was achieved by the injection of a free-carrier plasma into the waveguide. The free-carriers were injected into the waveguide region by forward biasing the PIN diode structure. The optical mode was supported in the intrinsic central rib section, which was surrounded by highly doped P and N regions. By varying the forward bias current, the attenuation was varied.

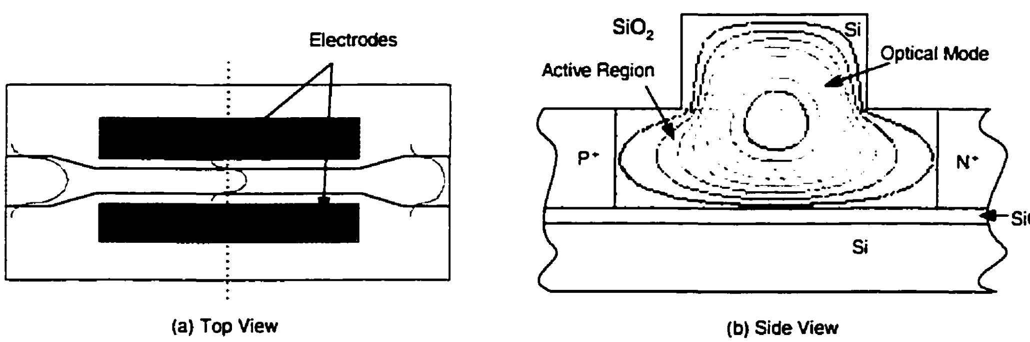


**Figure 2-1 Top view (a) of the free-carrier based attenuator showing location of electrodes. The dotted line shows where the cross section of the side view (b) is taken. Electrons and holes are injected into the intrinsic region to attenuate the optical signal where it overlaps with the distribution of free carriers.**

## *2.2 Silicon On Insulator Technology*

The top silicon layer must be high quality defect-free crystal in order for the carriers to propagate through the active region efficiently and for the optical signal to propagate with low loss. If the silicon were amorphous, propagation losses would increase and the free-carrier lifetimes and diffusion lengths would decrease due to scattering effects from grain boundaries in the amorphous material. Several techniques have been developed in the fabrication of silicon on insulator as a result of the need for a buried oxide layer in crystalline silicon [1]. One method uses homoepitaxial techniques to grow a thin layer of crystalline silicon overtop an oxidized silicon wafer. An amorphous layer of silicon deposited on an oxide layer then crystallized using either laser energy, or a high-energy electron beam (e-beam) or crystallization from the melt (ZMR). An alternative process is the separation by implantation of oxygen (SIMOX), where a bulk silicon wafer is implanted with oxygen to produce a buried oxide layer. The bond and etchback (BE-SOI) process can also be used, where an oxidized wafer is bonded to a bare wafer which is subsequently thinned. The most recent method is the Smart Cut process, where the implantation of hydrogen causes an oxidized wafer bonded to a non-oxidized wafer to break apart leaving behind a SOI wafer. The use of each technique is dictated by the specific application, each having its own set of advantages and disadvantages.

Silicon grown epitaxially on an oxidized wafer is done using a metal organic chemical vapor deposition reactor (MOCVD). Windows are cut into the oxide to provide seeding, which orients the crystal plane of the epitaxially grown silicon. The wafer is loaded into the reactor while a gas mixture of $SiH_2Cl_2$, $H_2$, and HCl flows through the chamber. The crystalline silicon grows both laterally and vertically to form a continuous layer overtop of the oxide. A disadvantage of this technique is that the size and location of the windows must be taken into account during mask layout and fabrication of devices.

Silicon can also be grown epitaxially without using seeding windows, however this will result in polycrystalline film due to the mismatch in thermal expansion coefficients between the silicon and the silicon dioxide. The films are stress-free during growth, however at room temperature relaxation in the silicon film takes place causing crystallographic defects such as dislocations. There are three main techniques used to recrystallize the over layer of silicon; laser recrystallization, e-beam recrystallization and ZMR. In laser recrystallization, a small beam of high-energy continuous wave light from $CO_2$ or Argon lasers has proven to produce crystalline silicon. Silicon is transparent to the 10.6μm wavelength light produced by $CO_2$ lasers, whereas the silica readily absorbs this wavelength. The silicon is heated indirectly from the energy absorbed by the silica layer. On the other hand, direct heating can be achieved with the use of argon lasers since silicon readily absorbs the 488 and 514nm wavelengths. A polycrystalline silicon film can also be crystallized using a beam of high energy electrons. Advantages of using e-beam recrystallization over lasers include precise control of the scanning beam and a more uniform absorption of energy. The uniformity of the recrystallization is improved since the silicon's absorption of energy is independent of crystalline state and reflectivity. ZMR produces a narrow zone of molten silicon using incoherent light sources. A heated strip of material such as graphite or a halogen lamp is scanned across the wafer which raises the temperature of the silicon. This method is quicker than laser or e-beam recrystallization since a whole wafer can be done in a single pass, whereas the former requires several passes of a small beam.

SIMOX technology produces a thin layer of silicon dioxide underneath a crystalline layer of silicon by implanting oxygen at high doses. This process is then followed by a high temperature anneal to form a crystalline silicon layer overtop of a silica layer with a thickness of a few hundred angstroms. The shape and quality of the layers depends on the implant dosage and temperature during the implant process. The critical dosage for production of a pronounced silica layer is $10^{18}/cm^3$. If the oxygen dosage is less than this, no substantial oxide layer will form, only silica precipitates. Implantation temperatures are usually in the range of 600 to 650°C. If the wafer temperature during the implant is too low, the amorphized silicon from the implantation will not fully recrystallize during the anneal. At higher temperatures, the implant damage suffered by the silicon over layer will be somewhat repaired during the implantation process, and fully re-crystallize during the anneal. If the wafer temperature is too high, silica precipitates will form in the silicon over layer.

The BE-SOI method first oxidizes a silicon wafer using wet or dry oxidization techniques, leaving a top layer of silica in the range of 0.5-1.5μm thick. This wafer and a second unoxidized wafer are polished mirror flat and made hydrophilic by a chemical surface treatment to assist in the bonding process. When these two wafers are brought into contact they immediately bond, the strength determined by hydrogen bonds. The wafers are then heated to achieve a higher bond energy as the hydrogen bonds are replaced by silicon-oxygen bonds. Before bonding, the wafers must be clean to prevent the formation of voids. The top wafer is then ground back to quickly remove all but the last several microns of silicon. This is followed by a chemical etch to achieve the correct thickness with high accuracy. The Smart Cut process is similar to BE-SOI but before bonding the oxidized wafer is implanted with hydrogen with a concentration in the range of $10^{16}$ to $10^{17}/cm^3$. Hydrogen has a larger implantation range than oxygen thus it travels deeper into the silicon substrate. The implantation is followed by hydrophilic bonding to another bare wafer with a subsequent heat treatment. During the heat treatment, the damage suffered by the silicon is repaired, and microcavities are formed at a depth corresponding to the depth of hydrogen implantation. The wafer implanted with hydrogen splits into two parts, leaving behind a thin layer of silica buried in crystalline silicon. The excess silicon is then removed by grinding and a chemical etch.

ZMR-SOI, SIMOX, BE-SOI and Smart Cut SOI are currently commercially available. The losses in single mode rib waveguides produced in each of the first three processes were measured by Zinke et al [2]. These results concluded that ZMR-SOI resulted in the highest loss (too high for optical applications), followed by SIMOX and BE-SOI. ZMR-SOI and SIMOX-SOI have higher optical absorption and scattering loss than BE-SOI. This is because BE-SOI and Smart Cut SOI result in a better quality silicon top layer and silicon-silica interface since no re-crystallization of the silicon over layer is required and a sharp junction is created in the bonding process. Smart Cut SOI is expected to perform similarly to BE-SOI since the silicon-silica interface is produced identically in both processes. Therefore, most photonic devices are fabricated from one of the latter two techniques.

## *2.3 Optical Design*

The goal of the optical design was to minimize losses incurred in the off state. The main sources of the off-state losses are the mode mismatch between the asymmetric waveguide mode and the circular fibre mode and free-carrier absorption from the heavily doped P and N regions. The losses due to the mode mismatch were minimized through a combination of an optimally shaped input facet with a linear taper to the active region. The losses due to free-carrier absorption were reduced by choosing a low doping concentration and wide intrinsic region width. The waveguide shape and taper design will be discussed next. Free-carrier effects will be discussed in the electrical design section.

### 2.3.1 Single Mode SOI Waveguides

For single mode propagation in waveguides, square or rectangular structures are often used. In materials that have a small difference between the core and cladding indices, a relatively circular mode profile results. Due to the large refractive index difference between silica and silicon, a single mode square waveguide in silicon buried in silica would have dimensions of 0.3μm according to the theory of slab waveguides. This would result in large coupling losses if standard telecom fibres were butt-coupled to the ends of the device because of the large mismatch since the mode field diameter (MFD) of a standard single mode fibre is 10.5μm. An alternative single mode structure is a rib waveguide, shown in Figure 2-2. The rib height is given by $2b\lambda$ and rib width given by $2a\lambda$, where $\lambda$ is the wavelength of light propagating through the guide. This structure supports single mode propagation in a larger waveguide allowing for more efficient coupling. However, the trade-off with this design is that the mode is pear-shaped and can never fully match the circular fibre mode.

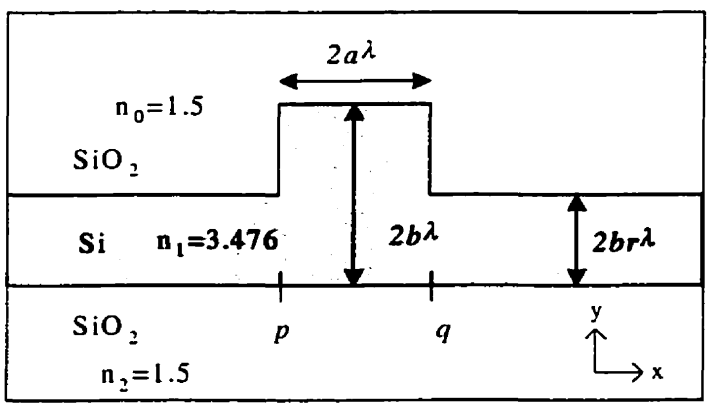


**Figure 2-2: Silicon on insulator rib waveguide structure. The outer slab extends very far in the y-direction. The substrate is assumed to be very thick. The rib waveguide allows for single mode propagation of a large mode.**

The single-mode condition for rib waveguides was calculated by Petermann [3]. For analysis, the rib waveguide can be separated into two different asymmetric slab waveguides, one with height $2b\lambda$ and the other with height $2br\lambda$, as shown in Figure

2-2. These calculations are restricted to rib waveguides with $2b\lambda \leq 4br\lambda$ with $r \leq 0.5$ where $r$ is the ratio of slab height to rib height. These restrictions only allow $HE_{0n}$ and $EH_{0n}$ modes to be guided where $n$ = 0,1,2.... The field components transverse with respect to the y-direction can be expressed as a sum of the fields in two slab waveguides with heights $2b\lambda$ and $2br\lambda$. If the cross-section is large enough, such that

$$k_o \cdot 2br\lambda \cdot n_1 >> 1 \qquad 2.1$$

where $k_o$ is the free space wavenumber, then the x-component of the electric field will go to zero for the HE mode and the x-component of the magnetic field will go to zero for the EH mode. Therefore, the HE and EH modes are obtained by summing over the x-components of the magnetic and electric fields, respectively since they do not equal zero. The transverse fields of the two slab waveguides are then matched at $p$ and $q$ in Figure 2-2. The remaining electric and magnetic field components are expanded. These are the x-component of the magnetic field in the thin slab and the z-component of the electric field in the thick slab of the HE mode, and the x-component of the electric field in the thin slab and the z-component of the magnetic field in the thick slab of the EH mode. The assumption is made that the matching of the x-components of the fields yields simultaneous matching of the z-components.

The x-direction dependence of the electric and magnetic fields in an asymmetric slab waveguide is given by

$$\left.\begin{matrix} E_x \\ H_x \end{matrix}\right\} \approx \sin(\chi_v x + \alpha), \qquad 2.2$$

where $\chi_v$ is a solution of the eigenvalue equations of the asymmetric slab waveguide,

$$\tan \kappa d = \kappa(\gamma + \beta)/(\kappa^2 - \gamma\beta) \qquad 2.3$$

$$\tan \kappa d = n_1^2 \kappa (n_3^2 \gamma + n_2^2 \beta)/(n_2^2 n_3^2 \kappa^2 - n_1^4 \gamma\beta) \qquad 2.4$$

In equations 2.3 and 2.4, $\kappa$, $\gamma$, and $\beta$ are abbreviations for expressions involving the refractive index and the free-space propagation constant. The eigenvalue equations can be solved approximately in the case of large waveguide heights $2b\lambda$ and $2br\lambda$,

$$\chi_{v(2b\lambda)} = \frac{(v+1)\pi}{2b\lambda} \cdot w_{2b\lambda} \qquad 2.5$$

$$\chi_{v(2br\lambda)} = \frac{(v+1)\pi}{2br\lambda} \cdot w_{2br\lambda} \qquad 2.6$$

where $v$=0,1,2... and

$$w_{2b\lambda} = \left[1 + \frac{1}{k_o 2b\lambda}\left(\frac{\gamma_o}{\sqrt{n_1^2 - n_0^2}} + \frac{\gamma_2}{\sqrt{n_1^2 - n_2^2}}\right)\right]^{-1}, \qquad 2.7$$

$$w_{2br\lambda} = \left[1 + \frac{1}{k_o 2br\lambda}\left(\frac{\gamma_o}{\sqrt{n_1^2 - n_0^2}} + \frac{\gamma_2}{\sqrt{n_1^2 - n_2^2}}\right)\right]^{-1}, \qquad 2.8$$

$$\gamma_{0,2} = \begin{cases} 1 & for \quad HE \\ (n_0 n_2 / n_1)^2 & for \quad EH \end{cases}. \qquad 2.9$$

The calculations can be simplified for waveguides with large widths such that $w_{2b\lambda} = w_{2br\lambda} = 1$. Effective widths $2b\lambda_{eff}$ and $2br\lambda_{eff}$ can be substituted for $2b\lambda$ and $2br\lambda$ in equations 2.5 and 2.6, respectively such that for $w_{2b\lambda} = w_{2br\lambda} = 1$, $\chi_v$ will remain unchanged yielding $2b\lambda_{eff} = 2b\lambda / w_{2b\lambda}$ and $2br\lambda_{eff} = 2br\lambda / w_{2br\lambda}$. The waveguide normalized frequency has been solved by the effective index method and is introduced as:

$$V = \frac{\pi w_{2b\lambda}}{2b\lambda} a\sqrt{\delta}, \quad with \qquad 2.10$$

$$\delta = \left(\frac{2b\lambda \cdot w_{2b\lambda}}{2br\lambda \cdot w_{2br\lambda}}\right) - 1. \qquad 2.11$$

The modes of the rib waveguide will propagate in the z-direction with propagation constant $\beta_z$, related to the eigenvalue $\chi$. The condition for single mode rib waveguides has been solved numerically by plotting $\chi$ as a function of $V$, shown in Figure 2-3. If $\chi$ describing $HE_{01}$ and $EH_{01}$ approaches the line $\chi = V$, then this mode ceases to be guided and the rib waveguide becomes single mode, guiding only the $HE_{00}$ and $EH_{00}$ modes since the higher order modes will be cut off. In other words, the higher order modes in the horizontal direction will not fit laterally under the rib. In addition, the higher order modes in the vertical direction, $EH_{10}$ and $HE_{10}$, will also be cut off because they will be coupled to the leaky fundamental modes of the slab section. This occurs for $r \geq 0.5$ since the effective index of the slab mode becomes greater than the effective index of any higher order vertical mode in the central rib region. The first order mode in the vertical and horizontal direction are shown in Figure 2-4. Petermann has calculated the single mode limit numerically and has defined this limit to be $V_s$, such that for $V \leq V_s$, the rib guide becomes single mode.

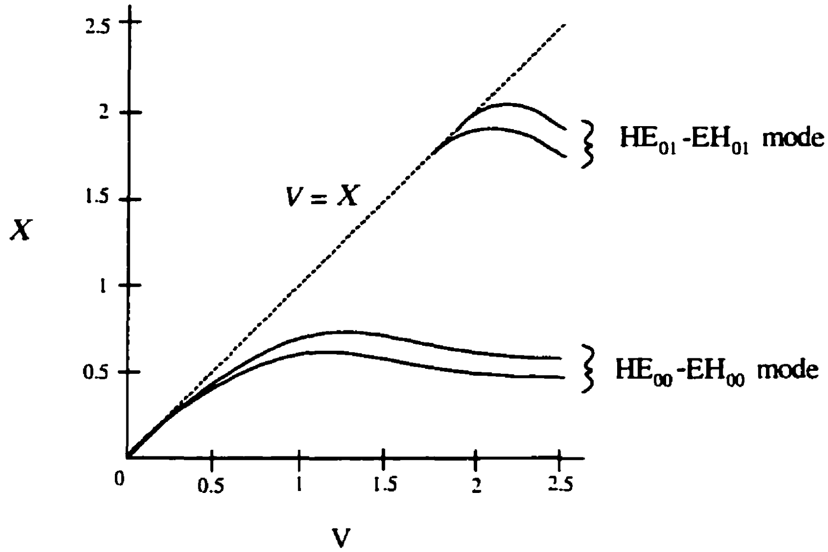


**Figure 2-3: The eigenvalue $\chi$ vs. the normalized frequency $V$. As $\chi$ approaches the line $V=\chi$, this mode ceases to be guided and the rib guide becomes single-mode, only supporting the $HE_{00}$ and $EH_{00}$ modes.**

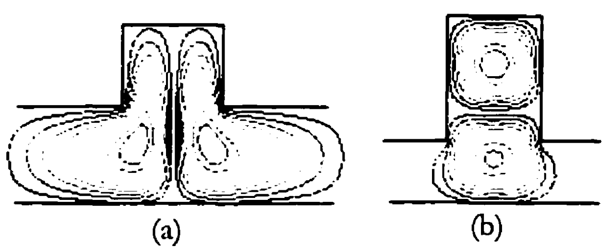


**Figure 2-4: Higher order modes of multi-mode rib waveguides. By decreasing the width of the rib of the waveguide shown in (a), the two lobes of the higher order mode shown will not be supported laterally under the rib. Instead they are greatly attenuated. By increasing the thickness of the outer slab regions of the waveguide shown in (b), the lower lobe of the higher order mode will couple out into the leaky slab mode.**

Soref [4] has done further work to find the limits of the waveguide dimensions that will result in single mode operation. This analysis is applicable to large rib waveguides satisfying the condition:

$$2b\sqrt{n_1^2 - n_2^2} \geq 1 \qquad 2.12$$

An approximation to the numerical solution obtained by Petermann was made; this resulted in a new waveguide normalized frequency:

$$V_s = \frac{\pi}{2}(1 + 0.3\sqrt{\delta}). \qquad 2.13$$

Using 2.10 and 2.13, the aspect ratio ***a/b*** is

$$\frac{a}{b} \leq 0.3 + \frac{r}{\sqrt{1-r^2}}. \qquad 2.14$$

This equation, along with 2.12 and $r \geq 0.5$, gives the waveguide dimensions that result in single mode rib waveguides; allowing only the $HE_{00}$ or $EH_{00}$ mode to propagate.

The stability of propagation of the single mode was tested using a beam propagation algorithm by Soref. The structure tested had $n_0 = 1.0$, $n_1 = 3.5$, $n_2 = 1.45$, $2b\lambda = 4\mu m$, $r = 0.625$, $a/b = 1$, and $\lambda = 1.3\mu m$. A higher order mode was launched by an off-axis excitation, and it was found that as the mode propagated the energy of the higher order mode leaked out the slab waveguide laterally until sufficient distance was traveled such that the field intensity shape returned to that of the fundamental mode.

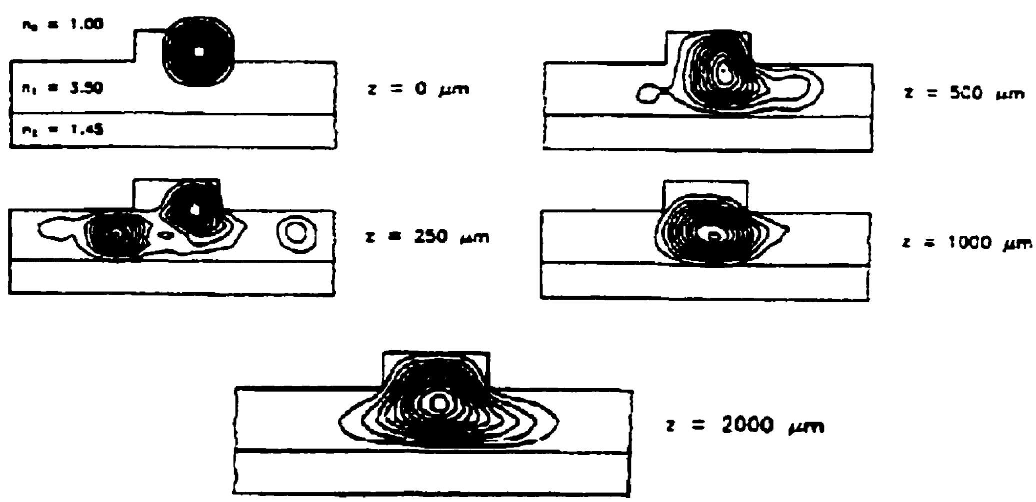


**Figure 2-5: Higher order mode excitation and propagation through a single mode rib waveguide [4]. As the propagation distance increases, more energy from the higher order mode leaks out laterally in the slab until the fundamental mode is arrived at.**

The theory in this section was used to narrow the calculation space in the attenuator design. Numerical calculations such as the beam propagation method were also used for more precise results.

### 2.3.2 Fibre-Waveguide Mode Mismatch

In this design, low-loss coupling from the waveguide to the input and output fibre is desirable. Since a small active region will reduce the on-state power consumption, the input and output sections should also be as small as possible if the same waveguide structure is used throughout. By using a small-core fibre for input and output coupling, the waveguide dimensions can be reduced considerably.

A small-core specialty fibre having a MFD of 4μm was used to couple the light into and out of the attenuator. For optimal coupling, the waveguide height and width should be approximately the same as the fibre core diameter and the index difference between the core and the cladding should be similar. If single mode fibre were used, the center rib of the input waveguide would need to be 9μm tall by 9μm wide, resulting in a multi-mode guide. This would greatly increase the operating power of the device since the P and N regions would be very far apart. Therefore, by using small-core fibre, the P and N regions can be brought closer together decreasing the power consumption.

Two different interface designs were investigated, one using a single mode coupling section, and the other using a multi-mode coupling section. In both cases, to find the optimal configuration for the input and output waveguides, the overlap integral between the 4μm Gaussian fibre mode and the waveguide mode must be calculated for a number of height and width combinations. The overlap integral was calculated using the Optiwave BPM CAD™ overlap integral utility, which uses the following relation to calculate the power overlap integral between two fields:

$$POI = \frac{\left| \int_{mesh} E_1(x,y) \cdot E_2^*(x,y)\,dxdy \right|^2}{\int_{mesh} \left| E_1(x,y) \right|^2 dxdy \cdot \int_{mesh} \left| E_2(x,y) \right|^2 dxdy} \qquad 2.15$$

A two dimensional integral of the product of one field and the conjugate of the other field is calculated over x and y, the transverse and lateral directions, respectively. Dividing this by the product of the normalized fields gives the power overlap integral. The integration step is taken to be the size of the mesh in the x and y directions used during the initial simulation of the fields.

### 2.3.2.1 *Single Mode Interface*

Single mode behavior is assured if the relations given in section 2.3.1 are followed. Using the two-dimensional mode solver and the scanning overlap integral tool provided in the Optiwave BPM-Cad software package, the optimal single mode configuration was found. This is shown in Figure 2-6 for the TE mode and Figure 2-7 for the TM mode.

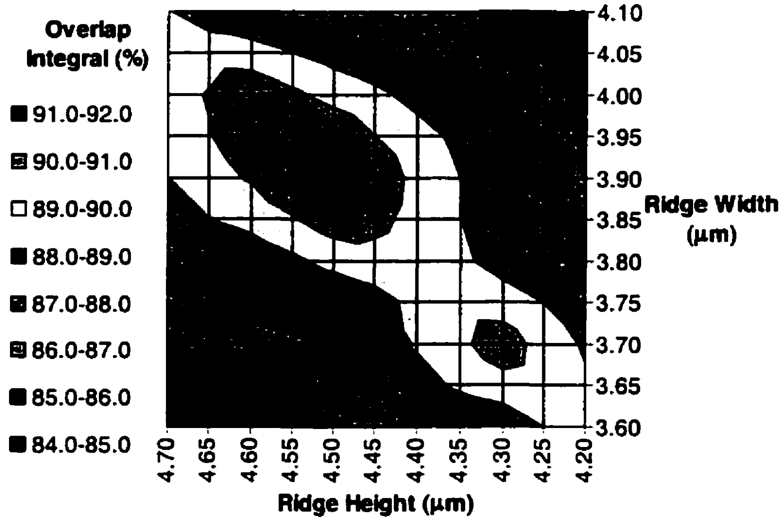


**Figure 2-6: Overlap integral for the TE mode as a function of single mode rib waveguide dimensions. The ratio of slab height to rib height was kept constant at 0.5.**

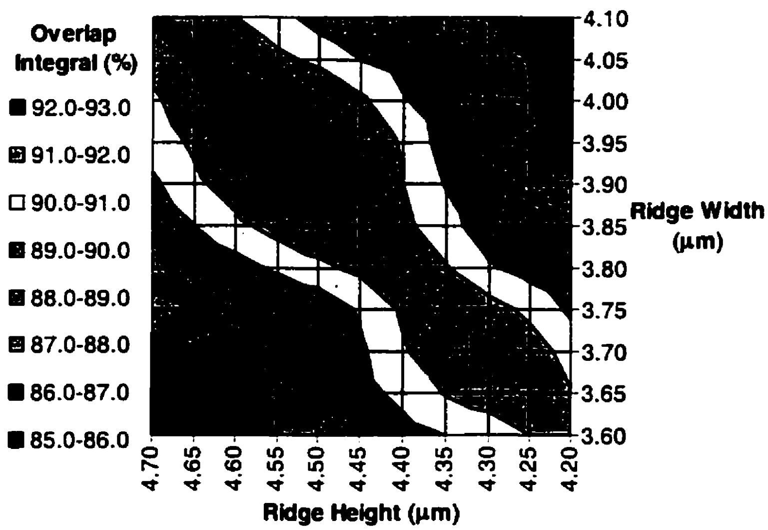


**Figure 2-7: Overlap integral for the TM mode as a function of single mode rib waveguide dimensions. The ratio of slab height to rib height was kept constant at 0.5.**

The overlap integral scanner tool in Optiwave's BPM Cad software package was used to calculate the overlap integrals presented. This tool scans one field over the other such that the maximum overlap is achieved. This ensures that the two fields are centered on each other. The single mode configuration that gives the highest overlap integral and least difference in overlap between the TE and TM modes has a ridge width of 3.9μm, ridge height of 4.5μm, and slab height of 2.25μm. This gives a loss per facet of 0.38dB for the TE mode and 0.32dB for the TM mode. For both facets combined, this would give a total loss and PDL due to coupling of 0.7dB and 0.06dB, respectively. Figure 2-8 shows the waveguide and specialty fibre MFDs.

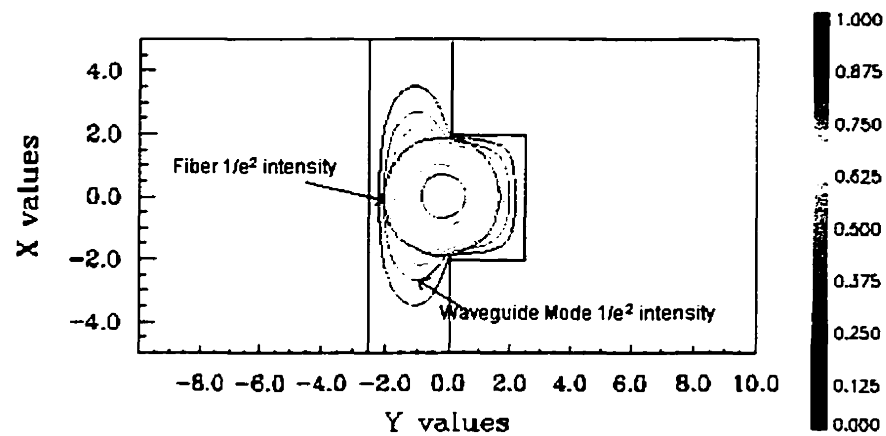


**Figure 2-8: Plot of the waveguide mode and the MM2 fibre MFD. The waveguide shown is the optimal coupling configuration that gives the lowest loss for a single mode waveguide, its dimensions are 3.9μm wide by 4.5μm high by 2.25μm deep.**

### *2.3.2.2 Multi-Mode Interface*

The coupling losses can be decreased significantly if an adiabatic taper is used to couple light into and out of the device. The overlap integral was calculated again, however this time the single mode waveguiding conditions given in section 2.3.1 were ignored. In the simulations, the following trends in mode shape with changes in waveguide dimensions were noticed:

- as the ratio r is increased, the amount of mode power in the slab part of the waveguide increased
- as the top layer width is increased, the amount of mode power in the slab part of the waveguide increases and the amount of mode power in the top layer rib section decreases
- as the total thickness is increased, the entire mode is shifted upwards

These trends were helpful in determining the optimal waveguide mode shape. The results of these simulations are shown in Figure 2-9 for the TE mode and Figure 2-10 for the TM mode.

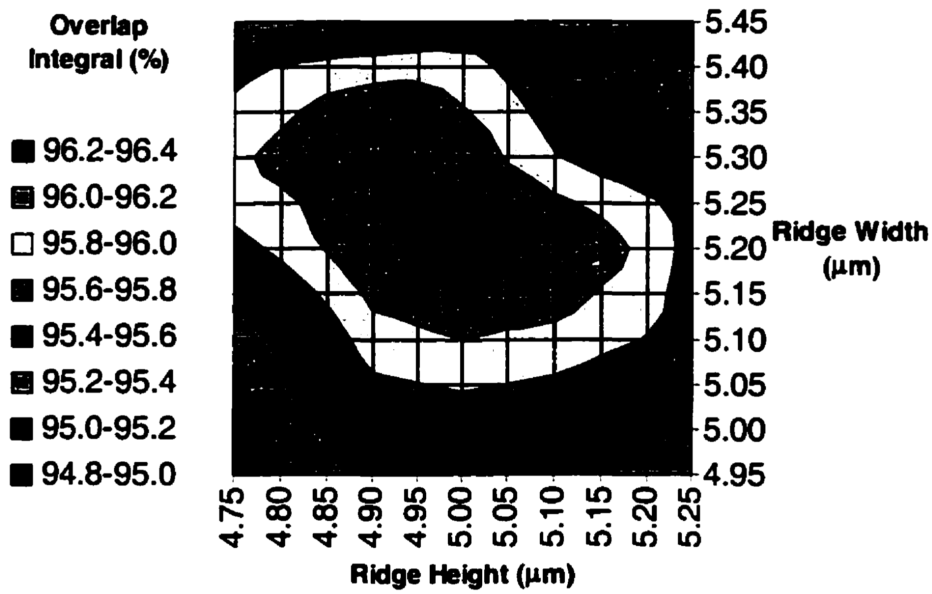


**Figure 2-9: Coupling loss as a function of rib waveguide dimensions for the TE mode. The ratio of slab height to rib height was kept constant at 0.5.**

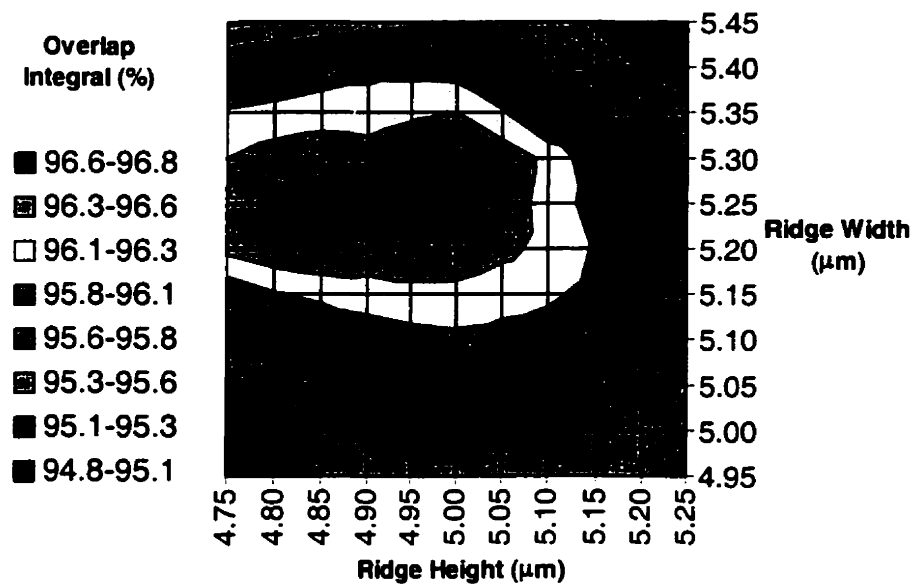


**Figure 2-10: Coupling loss as a function of rib waveguide dimensions for the TM mode. The ratio of slab height to rib height was kept constant at 0.5**

The multi-mode configuration that gives the highest overlap integral and least difference in overlap between the TE and TM modes had an overall height of 5.0μm, a slab height of 2.5μm and a rib width of 5.3μm. This resulted in a 96.203% overlap integral for the TE mode and a 96.220% overlap integral for the TM mode. The coupling loss has been reduced to 0.17dB/facet and PDL of 0.001dB. Figure 2-11 shows the waveguide and specialty fibre MFDs for the multi-mode configuration. The fibre mode $1/e^2$ intensity line follows that of the multi-mode waveguide mode much more closely than the single mode waveguide.

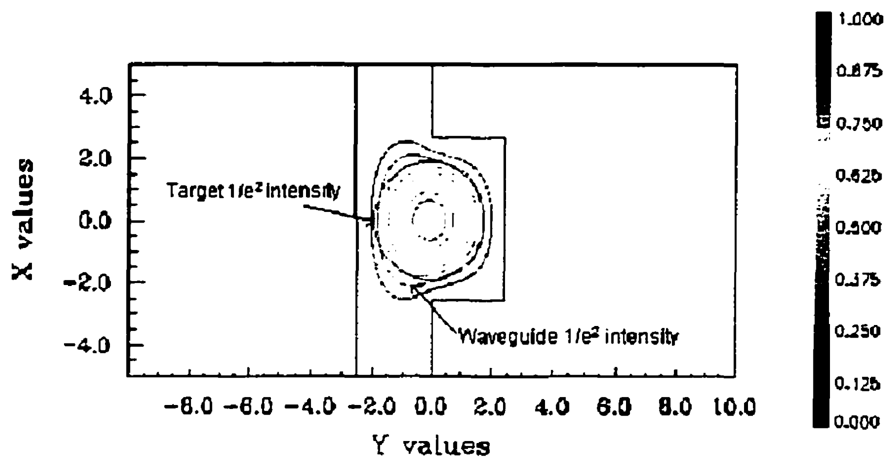


**Figure 2-11: Plot of the waveguide mode for the multi-mode configuration and the MM2 fibre MFD. The waveguide shown is the optimal coupling configuration that gives the lowest loss for a single mode waveguide, its dimensions are 3.9μm wide by 4.5μm high by 2.25μm deep.**

Single mode operation of the device must be achieved, even with multi-mode input and output coupling facets. Tapers can be used for an adiabatic mode transformation from the multi-mode input section to the single mode active region.

### 2.3.3 Waveguide Tapers

The tapers desired in this design should adiabatically concentrate the large lowest-order mode at the multi-mode input to a smaller mode in the single mode active region. This will ensure that the device is only operational when the lowest-order mode is propagating. Also, a small mode is desirable because this will reduce the on-state power consumption because the P and N regions can be placed closer together.

The single mode conditions discussed in section 2.3.1 are followed for the active region.

There are several different taper designs to choose from. Linear, exponential, and sine tapers are a few examples. These tapers could be lateral, that is tapering the top ridge only, or vertical, by tapering the overall height of the slab and the ridge, or a combination of both. Generally, vertical tapers are more difficult than lateral tapers since lithography techniques are optimized for changes in the lateral direction. Vertical tapers involve wet etching by dipping the wafer into an etchant, making it impossible to process a full wafer with many devices. Vertical tapers can also be realized by a mode transformation from a top rib waveguide that gradually decreases in width to zero down to a lower waveguide. However, the decrease in width of the top waveguide down to a sharp point is difficult to process. Due to these difficulties, the lateral taper leads to the lowest loss and easiest to manufacture. Examples of vertical and lateral tapers are shown in Figure 2-12.

Even though the input and output sections are multi-mode, the overall device will be single mode because the higher order modes will be stripped off in the taper region. Power coupled to $EH_{01}$ will not transfer to $EH_{00}$ efficiently. By removing the single mode condition, the fundamental mode size increased so as to match to a fibre. The fact that other modes are supported is undesirable, however this can be dealt with if certain launch conditions are met. Furthermore, if the taper only supports the two fundamental modes and the first odd modes, proper excitation and efficient coupling are not difficult. However, if the next even modes exist, coupling becomes difficult since the fundamental modes can easily couple into these modes.

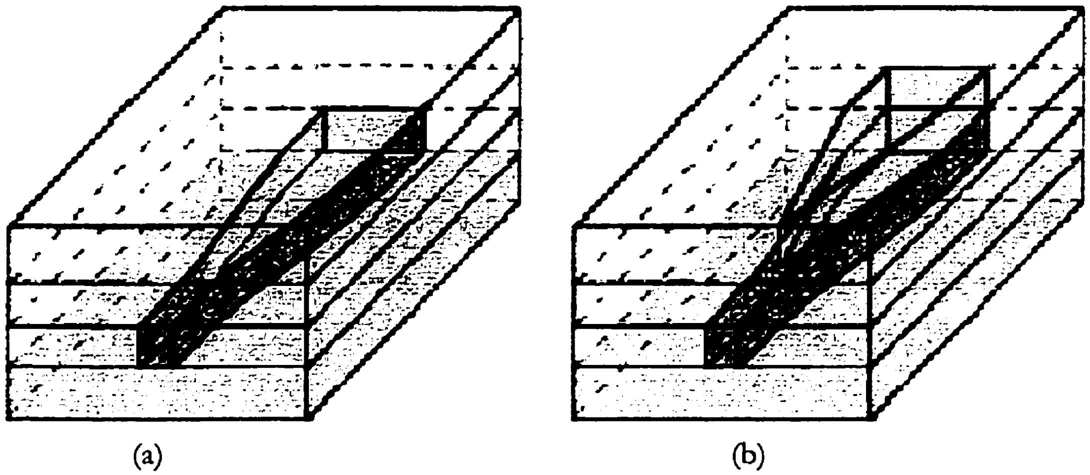


**Figure 2-12: Taper designs. In the lateral taper (a), only the top rib width is decreased. The taper in (b) is a combination of a lateral and a vertical taper where the width of the top and bottom ribs are decreased.**

Baets et al [5] has calculated radiation losses for mode transformations and has given some design rules for waveguide tapers. The three-dimensional guide is first reduced to a two-dimensional problem by using the effective index method. A beam propagation method (BPM) is then used to calculate the adiabatic power transfer between the lowest-order modes of the input and output waveguides for linear tapers. In this sense, the input guide is the multimode coupling section and the output guide is the single mode active region. Abrupt and tapered transitions were analyzed; these are shown in Figure 2-13.

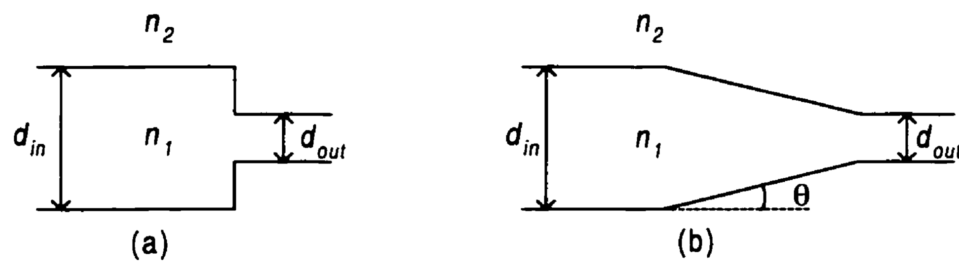


**Figure 2-13: Two-dimensional waveguide mode transformers. An abrupt transition is shown in (a) and a linear tapered transition is shown in (b).**

Abrupt transitions will first be considered. If the input waveguide is excited with its fundamental mode and adiabatic power transfer is assumed, the power in the output waveguide is:

$$P_{out} = \left| \int_{-\infty}^{\infty} \Psi_{in}(x) \cdot \Psi^{*}_{out}(x) \right|^2 \qquad 2.16$$

where $\Psi_{in}$ and $\Psi_{out}$ are the lowest order modes at the input and output waveguides, respectively. The normalized frequencies of the input and output waveguides are given by:

$$\begin{aligned} V_{in} &= k_o d_{in} \sqrt{n_1^2 - n_2^2}, \\ V_{out} &= k_o d_{out} \sqrt{n_1^2 - n_2^2} \end{aligned} \qquad 2.17$$

where $d_{in}$ and $d_{out}$ are the input and output waveguide widths. The output power has been plotted by Marcuse [11] as a function of the geometric mean of the normalized frequencies, $V_m = \sqrt{V_{in} \cdot V_{out}}$, for different reduction ratios, where the reduction ratio, $N = d_{in}/d_{out}$, is the ratio of input and output normalized widths. These curves are shown in Figure 2-14. A minimum occurs for $V_m$ = 2.5 for all values of $N$. The sharpness of the minimum decreases for decreasing reduction ratios. The reduction ratio and mean normalized frequency for a waveguide with an input starting width of 5.3μm to an output width of 4.3μm is 1.2 and 60.7, respectively.

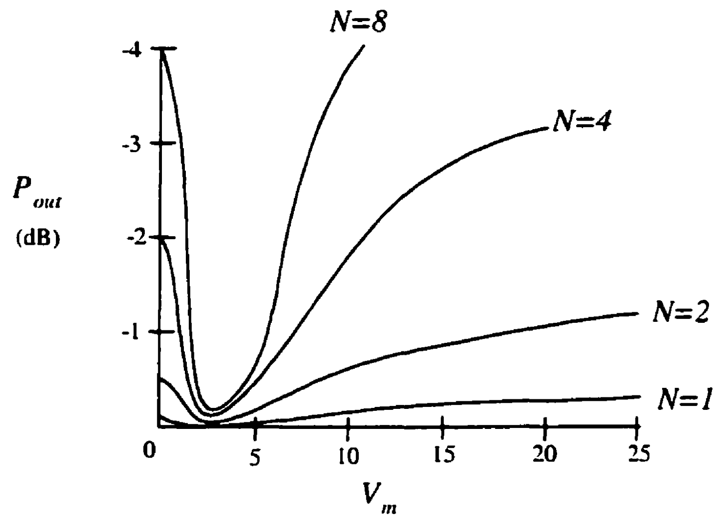


**Figure 2-14: Power transfer between fundamental modes in an abrupt transition for different reduction ratios . All curves show a minimum for $V_m$=2.5. Better power transfer is achieved for lower reduction ratios.**

An abrupt junction would result in high losses; greater than 1dB for two tapers according to Figure 2-14. Therefore, a taper is necessary to decrease mode transformation losses.

The radiation losses for tapered waveguides have also been computed by Baets [5]. These have been found to be dependant on the mean normalized frequency, the reduction ratio and the effective taper angle, given by:

$$\sin\theta_{eff} = \frac{\sin\theta}{N.A.} \tag{2.18}$$

where $N.A. = \sqrt{n_1^2 - n_2^2}$ is the numerical aperture and $\theta$ is the taper half angle. The transmission losses of abrupt transitions for high $V_m$ values can be reduced by a linear taper. In the case of the abrupt transition, the normalized frequency changed immediately from $V_{in}$ to $V_{out}$. In the case of a linearly tapered transition, the normalized frequency changes slowly from $V_{in}$ to $V_{out}$, and the effective width of the fundamental mode first decreases and then increases again. This mode transformation will lead to radiation losses unless the taper half angle is very small. Figure 2-15 shows radiation losses for linear tapers of varying half angles for a reduction ratio of $N$ = 2.

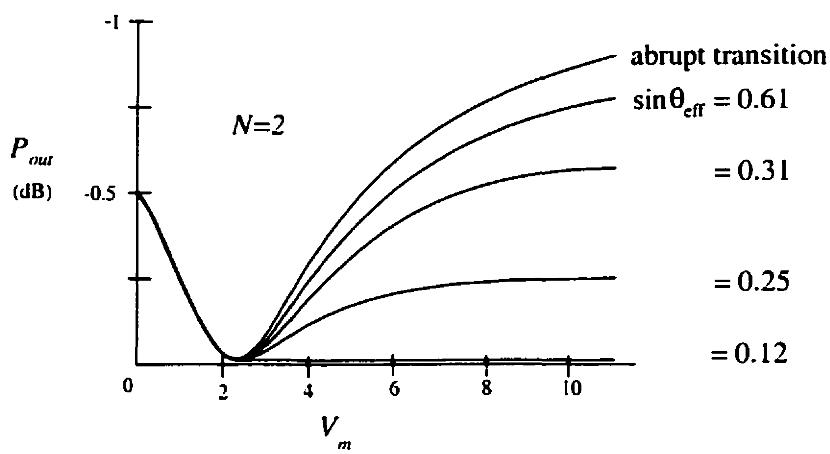


**Figure 2-15: Radiation losses for tapers of varying angles for a reduction ratio of 2. As the taper angle is decreased the radiation losses decrease. $\theta_{eff}$ is measured in degrees.**

The losses due to mode mismatching can be greatly improved with the use of tapers. Radiation losses decrease with taper angle; therefore the lowest taper losses will be achieved with a longer taper.

Tapers were simulated using Optiwave's 3D BPM simulator. Three different taper designs were simulated for varying lengths, shown in Figure 2-16. It can be seen that for small *N*, one can not improve much over linear tapers by using tapers of a different shape.

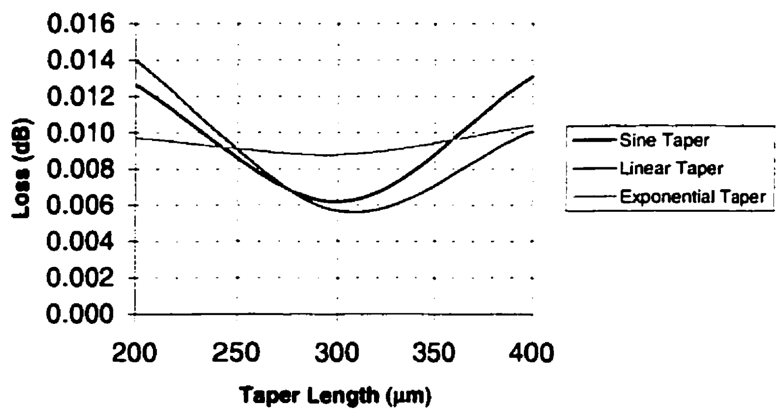


**Figure 2-16: 3D BPM simulation results for sine, linear, and exponential tapers. The loss shown is the total loss resulting from two tapers; one at the input and one at the output of the device. The linear taper has the lowest loss of <0.006dB. For taper lengths less than 300μm, loss increases due to radiation losses.**

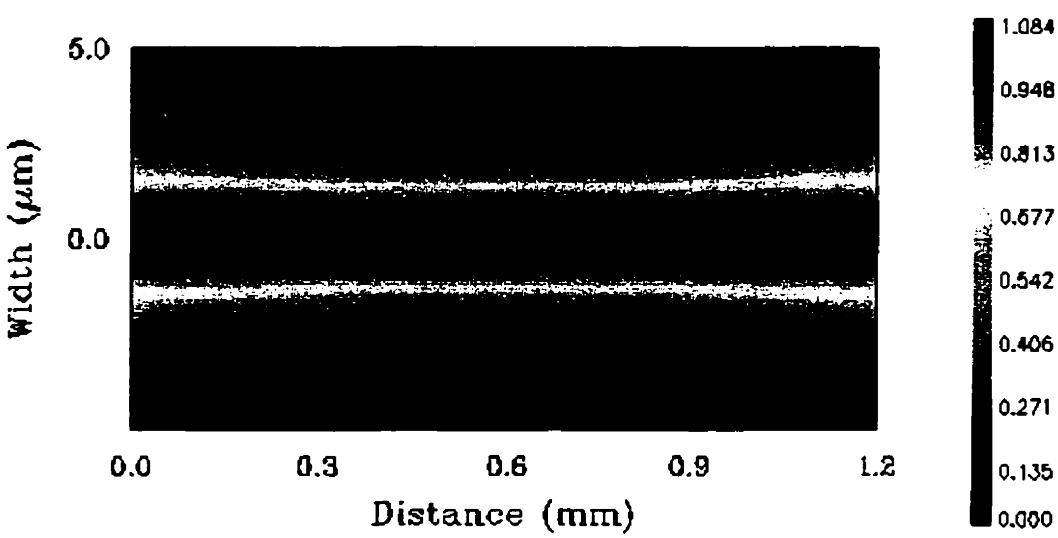

**Figure 2-17: Results of 3D BPM simulation of optimal taper design. Optical intensity in a 300μm taper, followed by a 500μm single mode straight section and another 300μm linear taper is shown.**

As can be seen from Figure 2-16, the optimal taper length for the design is 300μm using a linear taper. This results in $sin\theta_{eff} = 5.4x10^{-4}$, small enough to reduce the losses from an abrupt junction. For a shorter taper, radiation losses are high even though $sin\theta_{eff}$ is small since this transition has a large $V_m$. If the taper is longer than 300μm, losses increase due to coupling from the fundamental mode into higher order modes. This is because the input waveguide can support multiple modes. The waveguide does not become single mode until the output of the taper. An optical density plot in the x-z plane from a 3D BPM simulation of the device with input and output tapers is shown in Figure 2-17.

## *2.4 Electrical Design*

The goal of the electrical design was to minimize the off-state losses incurred by the doped sections while maximizing the attenuation characteristics and minimizing the power consumption in the on-state. This was done by choosing the appropriate doping concentration, separation, and length of the doped sections.

### 2.4.1 Free-Carrier Absorption

Free-carrier absorption is an indirect electronic absorption process. A carrier is excited to a higher energy state in the same band by a photon and one or more phonons. A change in the carrier's wavevector is produced by the wavevector of the phonon. This results in a non-vertical transition within the conduction or valence band. There are two processes that can occur in free carrier absorption, shown in Figure 2-18.

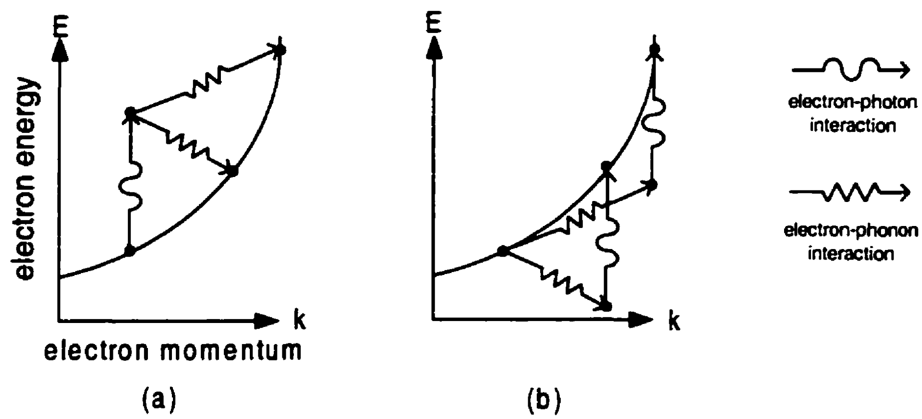


**Figure 2-18: Free-carrier absorption process [6]. A photon can be absorbed first followed by phonon emission or absorption (a) or phonon scattering occurs first (b). both processes result in a change in the carrier's wavevector.**

The photon can be absorbed first by the electron and enter an intermediate state with no change in momentum. The electron then either emits or absorbs a phonon to reach its final state in the conduction band. Another absorption process that can take place starts with the electron brought to an intermediate state by phonon scattering followed by absorption or emission of a phonon by the electron. The electron then reaches its final state by photon absorption.

Free-carrier absorption has been modeled both theoretically using the classical Drude theory of free-electrons [6] and by a Kramers-Kronig transform of experimental absorption spectra by Soref et. al. [7]. Both methods describe different material properties and are useful in determining device characteristics. Before these are described, it is important to consider the effects of high concentrations of free-carriers in semiconductors.

### *2.4.1.1 Effects of High Carrier Concentration on Carrier Behavior*

As the free-carrier concentration in a semiconductor increases, the characteristics describing their behavior change. Both the mobility and the lifetime are affected by their density. The carrier mobility decreases with increasing carrier concentration due to carrier-carrier scattering effects, and can be described by the following equation [8]:

$$\mu = (m^*)^{1/2} N^{-1} T^{3/2}, \qquad 2.19$$

where m* is the carrier's effective mass, N is the free-carrier concentration and T is the temperature. This relation is plotted in Figure 2-19.

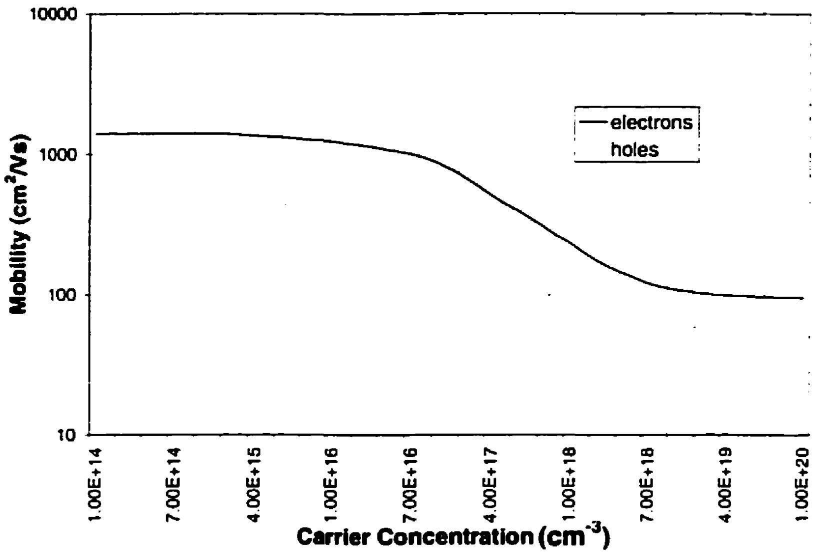


**Figure 2-19: Drift Mobility of electrons and holes vs. carrier concentration in silicon at 300K [8]. As the free-carrier concentration increases, the mobility decreases due to carrier-carrier scattering effects.**

The free-carrier lifetime will also decrease with increasing injected free-carrier concentration due to Auger recombinations. Up to approximately $10^{17}/cm^3$ carrier concentration the carrier lifetime is the non-radiative recombination lifetime, $\tau$=100ns. This will decrease with increasing carrier concentration due to the Auger recombination process. Auger recombination is the process in which the energy released by a recombining electron is absorbed by another conduction electron, which emits this energy non-radiatively and produces phonons. The effective recombination lifetime at high injection levels is approximately inversely proportional to the square of the free-carrier density. The decrease in free-carrier lifetime with increasing free-carrier density is shown in Figure 2-20 and can be described by [8]:

$$1/\tau_{eff} = 1/\tau_a + CN^2, \qquad 2.20$$

where $\tau_{eff}$ is the effective free-carrier lifetime, $\tau_a$ is the ambipolar lifetime, $N$ is the carrier concentration and C is the Auger recombination coefficient, which has been experimentally determined by Sinton [9] to have a value of $1.6\text{x}10^{-30}cm^6/s$.

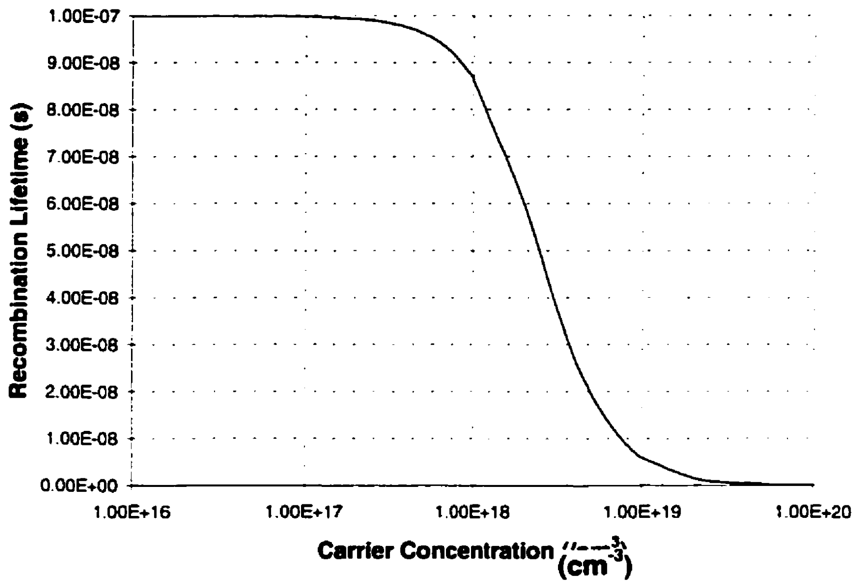


**Figure 2-20. Free-carrier recombination lifetime as a function of free-carrier concentration. As the concentration increases, the lifetime decreases due to Auger recombination.**

### *2.4.1.2 Classical Theoretical Drude Model of Free-Carrier Absorption*

Free carriers in a semiconductor cause a change in the real and imaginary part of the refractive index. Thus, a change in the absorption coefficient and real refractive index results. This phenomenon is described by the classical Drude theory of free-carrier absorption or refraction, which models the plasma of electrons and holes as a classical oscillator, ignoring the effects of ionized impurities [10].

The high-frequency conductivity of a material can be described by a model of an electron with effective mass $m_e$ under an external force. It can be assumed that the electron flows in a viscous medium with friction constant $1/\tau$, where $\tau$ is the relaxation time. The damping constant is then $1/\tau = \omega_o$.

The equation of motion of an electron in the presence of the electric field of light is given by:

$$m_e(\dot{v}+\omega_o v) = -qE = q\varepsilon_\lambda E_o e^{i(\mathbf{k}\cdot\mathbf{r}-\omega t)}, \qquad 2.21$$

where $v$ is the electron's velocity, $\dot{v}$ is its acceleration, $E_o$ is the amplitude of the light's electric field, $q$ is the electronic charge, and $\varepsilon_\lambda$ is the unit vector in the direction of the light's polarization. The solution of 2.20 is obtained by imposing the same time dependence as the electric field on the electron's velocity:

$$m_e(-i\omega + \omega_o)v = -q\varepsilon_\lambda \boldsymbol{E}\,. \qquad 2.22$$

The expression for current density can be found by solving for $v$ and using $v(\omega=0)=eE/m_e\omega_o$:

$$\boldsymbol{J} = \sigma\boldsymbol{E} = \Delta N q v = \sigma_o \omega_o \frac{\omega_o + i\omega}{\omega_o^2 + \omega^2}\boldsymbol{E}\,, \qquad 2.23$$

where $\Delta N$ is the change in electron density and $\sigma_o$ is the low frequency conductivity given by:

$$\sigma_o = \frac{\Delta N q^2 \tau}{m_e}\,. \qquad 2.24$$

Maxwell's equations and the expression for the complex conductivity given in 2.23 can be used to determine the change in real refractive index and absorption with a change in electron concentration. From Maxwell's equations:

$$\nabla \times \boldsymbol{E} = -\mu_o \frac{\partial \boldsymbol{H}}{\partial t} \text{ and } \nabla \times \boldsymbol{H} = \varepsilon_s \varepsilon_o \frac{\partial \boldsymbol{E}}{\partial t} + \boldsymbol{J}\,,$$

$$-\nabla \times \nabla \times \boldsymbol{E} = \mu_o \frac{\partial}{\partial t}\left( \varepsilon_o \varepsilon_s \frac{\partial \boldsymbol{E}}{\partial t} + \sigma\boldsymbol{E} \right)$$

$$= \frac{\varepsilon_s}{c^2}\frac{\partial^2 \boldsymbol{E}}{\partial t^2} + \frac{\sigma}{\varepsilon_o c^2}\frac{\partial \boldsymbol{E}}{\partial t}\,, \qquad 2.25$$

where $\varepsilon_s$ is the static relative permittivity, the main contribution of which comes from the lattice. The time and space derivatives are obtained from 2.21 and the relation:

$$\nabla \times \nabla \times \boldsymbol{E} = \nabla(\nabla \cdot \boldsymbol{E}) - \nabla^2 \boldsymbol{E}\,. \qquad 2.26$$

Therefore,

$$\left[ \left(\frac{\omega}{c}\right)^2 \varepsilon_s + \frac{i\omega\sigma}{\varepsilon_o c^2} \right] \boldsymbol{E} = k^2 \boldsymbol{E} - k(k \cdot \boldsymbol{E})\,, \qquad 2.27$$

where $\boldsymbol{E}$ is perpendicular to $\boldsymbol{k}$. The refractive index can now be solved for:

$$k = \frac{\omega}{c}(n_r + in_i)\,;$$

$$(n_r + in_i)^2 = \varepsilon_s + i\frac{\sigma}{\varepsilon_o \omega}\,. \qquad 2.28$$

By separating the real and the imaginary parts of 2.28 and using 2.23, the real and imaginary permittivity can be found:

$$\varepsilon_1 = n_r^2 - n_i^2 = \varepsilon_s - \frac{1}{\varepsilon_o \omega}\mathrm{Im}(\sigma) = \varepsilon_s\left(1 - \frac{\omega_p^2}{\omega_o^2 + \omega^2}\right) \qquad 2.29$$

and

$$\varepsilon_2 = 2n_r n_i = \frac{1}{\varepsilon_o \omega}\mathrm{Re}(\sigma) = \varepsilon_s \frac{\omega_o}{\omega}\frac{\omega_p^2}{\omega_o^2 + \omega^2}, \qquad 2.30$$

where $\omega_p$ is the plasma frequency, given by:

$$\omega_p^2 = \frac{\Delta N q^2}{m_e \varepsilon_s \varepsilon_o}. \qquad 2.31$$

The change in real refractive index with a change in carrier concentration can now be found. The permittivity, $\varepsilon_l$, is modified from its static value $\varepsilon_s$ by additional negative terms due to the presence of free carriers. This term is proportional to the free-carrier concentration and is negligible when the concentration is small, when the electron-phonon coupling is large, or when the frequency of the incident light is high. The contribution to the permittivity by free carriers is large when the incident light frequency approaches the plasma frequency, $\omega_p$. Using equation 2.29, the change in permittivity due to free carriers can be written as:

$$\Delta\varepsilon = \frac{\Delta N q^2}{m_e \varepsilon_o}\frac{\tau^2}{1 + \omega^2\tau^2}. \qquad 2.32$$

If the frequency of the electromagnetic wave is very high, then $\omega\tau \gg 1$ and the change in $\varepsilon_l$ is independent of $\tau$, but decreases as $\omega^{-2}$. The change in refractive index can be written from equation 2.32 and using the approximation $\varepsilon_l = (n + \Delta n)^2 \cong (n^2 + 2n\Delta n)$;

$$\Delta n = \frac{-\Delta N q^2 \lambda^2}{8\pi^2 m_e \varepsilon_o c^2 n}. \qquad 2.33$$

The theory presented here assumed that the free-carrier plasma consists solely of electrons. If the free-carrier plasma consists of both electrons and holes then equation 2.33 must take into account their difference in masses;

$$\Delta n = \frac{-q^2\lambda^2}{8\pi^2 \varepsilon_o c^2 n}\left(\frac{\Delta N_e}{m_e} + \frac{\Delta N_h}{m_h}\right). \qquad 2.34$$

where the subscripts $e$ and $h$ refer to electrons and holes, respectively.

The change in absorption can be determined from the imaginary part of the permittivity as given in equation 2.30. Using the relation $\alpha = 2\omega n_i/c$ and equation 2.30, the absorption change can be written as:

$$\Delta\alpha = \frac{\Delta N q^2}{m_e \varepsilon_o c n_r} \frac{\tau}{1+\omega^2\tau^2} \qquad 2.35$$

If the incident light's frequency is high, such that $\omega\tau \gg 1$, 2.35 becomes:

$$\Delta\alpha = \frac{\Delta N q^2}{m_e \varepsilon_o c n_r \omega^2} \frac{1}{\tau}$$

$$= \frac{\Delta N e^2 \lambda^2}{m_e \varepsilon_o c n_r 4\pi^2} \frac{q}{m_e \mu_d}, \qquad 2.36$$

where $\mu_d$ is the drift mobility. If the free carrier plasma consists of electrons and holes, their differences in effective masses and drift mobilities must be taken into account. The change in absorption is then:

$$\Delta\alpha = \frac{q^3\lambda^2}{4\pi^2\varepsilon_o c^3 n}\left(\frac{\Delta N_e}{m_e^2\mu_e} + \frac{\Delta N_h}{m_h^2\mu_h}\right). \qquad 2.37$$

### *2.4.1.3 Experimental Soref Model of Free-Carrier Absorption*

The change in refractive index and absorption coefficient with a change in free-carrier concentration has also been determined by Soref by a numerical Kramers-Kronig analysis of experimental impurity-doping spectra taken from the literature. The optical wavelength region studied was between 1.0 and 2.0μm.

The Kramers-Kronig dispersion relations describe the coupling between the absorption coefficient and the refractive index. These relations also hold for the coupling between the changes in absorption coefficient and refractive index :

$$\Delta n(\omega) = \frac{c}{\pi}\left(P\int_0^\infty \frac{\Delta\alpha(\omega')}{\omega'^2-\omega^2} d\omega'\right), \qquad 2.38$$

where the photon energy is $\hbar\omega$. The change in absorption coefficient due to a change in the free-carrier concentration can be written as:

$$\Delta\alpha(\omega,\Delta N) = \alpha(\omega,\Delta N) - \alpha(\omega,0) \qquad 2.39$$

The data used from for this analysis was taken from data of the effects of impurity doping on the optical properties of silicon. It was assumed in this analysis that it is equivalent optically if the carriers come from impurity ionization or from injection. Experimental results from several sources describing the change in the absorption spectrum of silicon with a change in impurity atom density were analyzed. The change in index was calculated from these experimental results using the Kramers-Kronig transforms described above.

Three important carrier effects were taken into account that change the optical properties of silicon, these are free-carrier absorption, Burstein-Moss bandfilling, and Coulombic interaction of carriers with impurities. Burstein-Moss bandfilling occurs in heavily doped semiconductors. The Fermi level moves inside the band, increasing the band gap and shifting the absorption edge to shorter wavelengths. The Coulombic interaction of carriers with impurities shifts the spectrum to longer wavelengths. With a high impurity density, impurity atoms introduce local variations in the potential energy of an electron due to the difference of the nuclear potentials of the impurity atom and the host atom. This results in an extension of the energy band edges, also known as band tails. Overall, a shift to longer wavelengths is seen due to the three carrier effects [10].

Results from Soref's analysis and the Drude model are shown in Figure 2-21 and Figure 2-22. Soref found that free holes are more effective in causing an index perturbation than free electrons up to a carrier concentration of $4x10^{19}/cm^3$. At a hole concentration of $10^{17}/cm^3$, the change in index created by holes is 3.3 times that of electrons. This differs from the Drude theory result where the change in index created by holes is 0.66 times that of electrons over the entire concentration range. Similarly, holes have a larger effect on the change in absorption than electrons up to a concentration of $5x10^{17}$. The Drude model predicts that the holes have a larger effect across the entire concentration range. Overall, there exists large (order of magnitude) differences in the change in refractive index and absorption coefficient between the Drude model and the Soref model. This discrepancy will be seen again later in the device calculations.

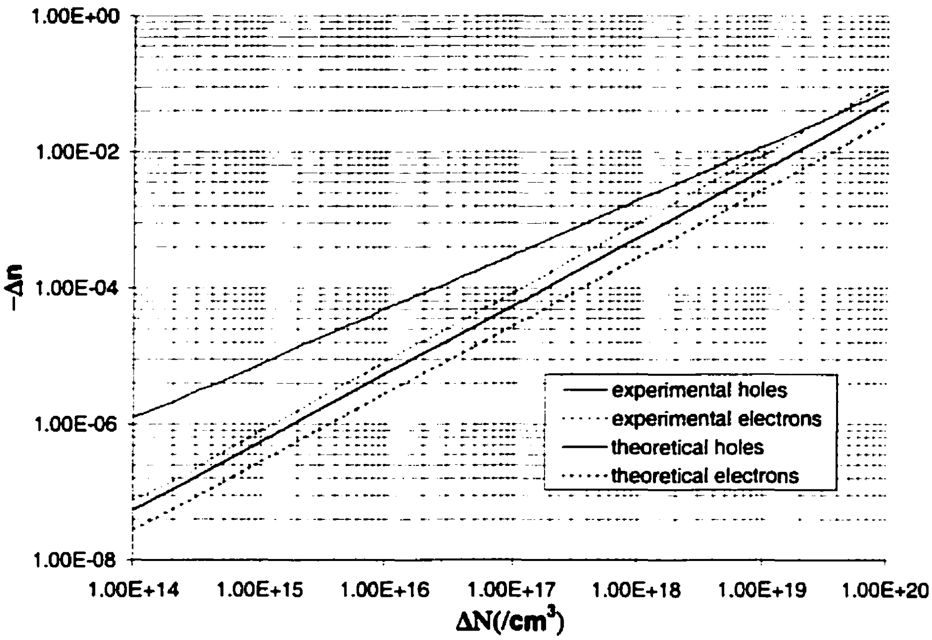


**Figure 2-21: Change in refractive index with carrier concentration according to the Soref (experimental) and Drude (theoretical) models in crystalline silicon at a wavelength of 1.55μm [7].**

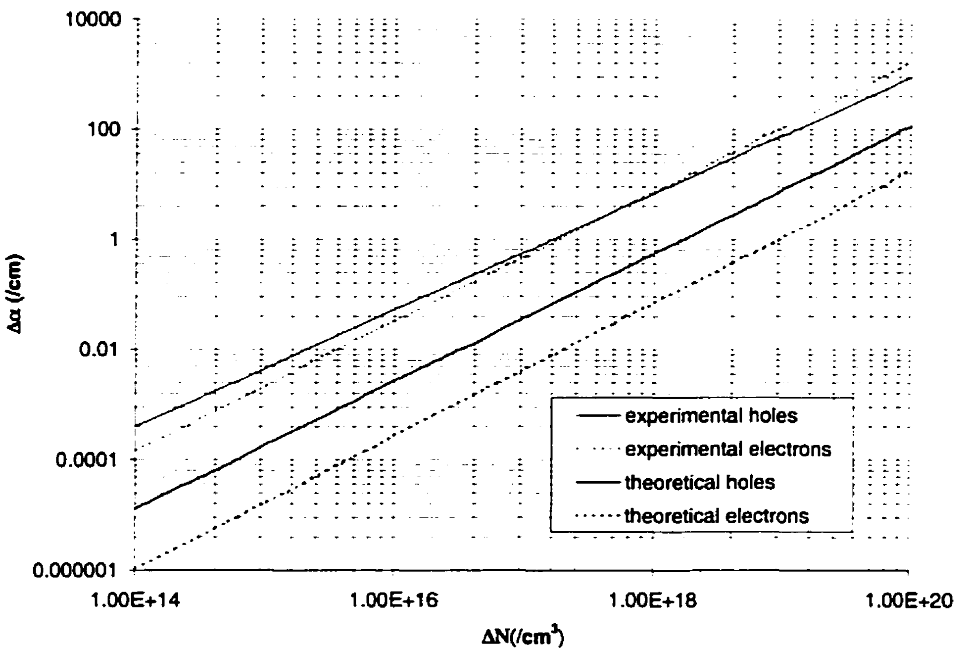


**Figure 2-22: Change in absorption with carrier concentration according to the Soref (experimental) and Drude (theoretical) models in crystalline silicon at a wavelength of 1.55μm [7].**

From this analysis, the change in index and absorption due to a change in free-carrier concentration at a wavelength of 1.55μm can be expressed as:

$$\Delta n = -8.8\times10^{-22}\cdot\Delta N_e + 8.5\times10^{-18}\cdot\Delta N_h \quad 2.40$$

$$\Delta\alpha = 8.5\times10^{-18}\cdot\Delta N_e + 6.0\times10^{-18}\cdot\Delta N_h. \quad 2.41$$

The equations resulting from Soref's analysis accurately predict changes in index and absorption for a given concentration, however this is only valid at a wavelength of 1.55μm. It will be see that both the Drude model and the Soref model are valuable in predicting the characteristics of silicon with high carrier concentration.

### 2.4.2 Off-State Absorptive Losses

Due to free-carrier absorption in the heavily doped P and N regions, there will be losses when the attenuator is in the off-state i.e. when no current is applied to the device. These losses can be minimized by choosing a sufficiently low doping concentration and by spacing the doped sections far enough apart to reduce the overlap between the optical mode and the highly doped P and N regions. It must be kept in mind, however, that these parameters will also affect the diode's electrical characteristics and attenuation performance.

Both the Drude and Soref models of free-carrier absorption predict that as the doping concentration is increased, the refractive index decreases and the absorption coefficient increases. Therefore, with a high doping concentration there will be high losses in the off state if the doped sections are placed too close together. Part of the mode traveling through the intrinsic region will overlap with the P and N regions if they are placed to close together, resulting in high off-state losses. The ridge width of the active region should not be decreased since this leads to an expansion of the mode into the slab, which would increase the spacing of the active regions. Several doping concentrations and doped section separations were simulated with BPM CAD™ using Soref's model of free-carrier absorption for the absorption coefficients and refractive indices of the doped sections. The length of absorption regions of 1mm and 1cm were simulated, shown in Figure 2-24 and Figure 2-23, respectively. In these simulations, it was assumed that the P and N regions form abrupt junctions with the intrinsic region.

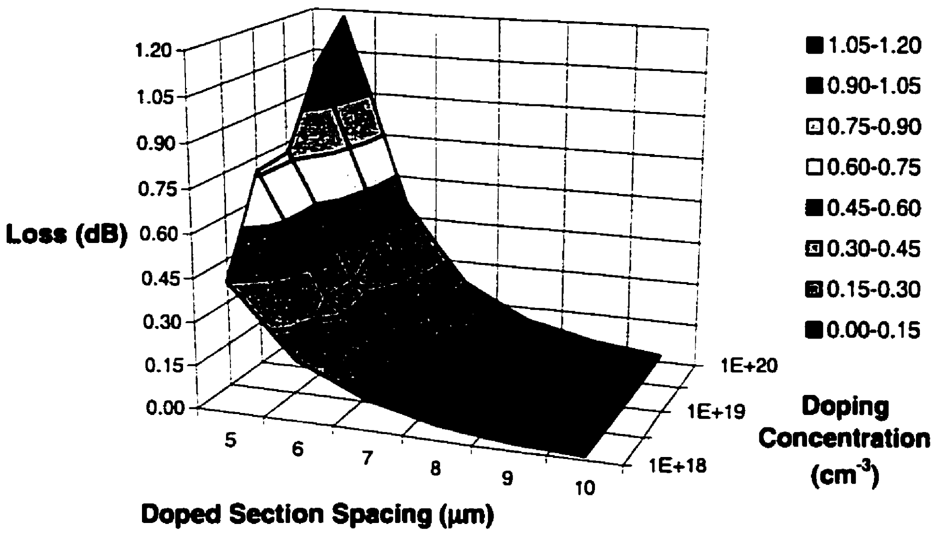


**Figure 2-23: Simulated results of the effect of doped section spacing and doping concentration on the off-state losses for a 1mm long device.**

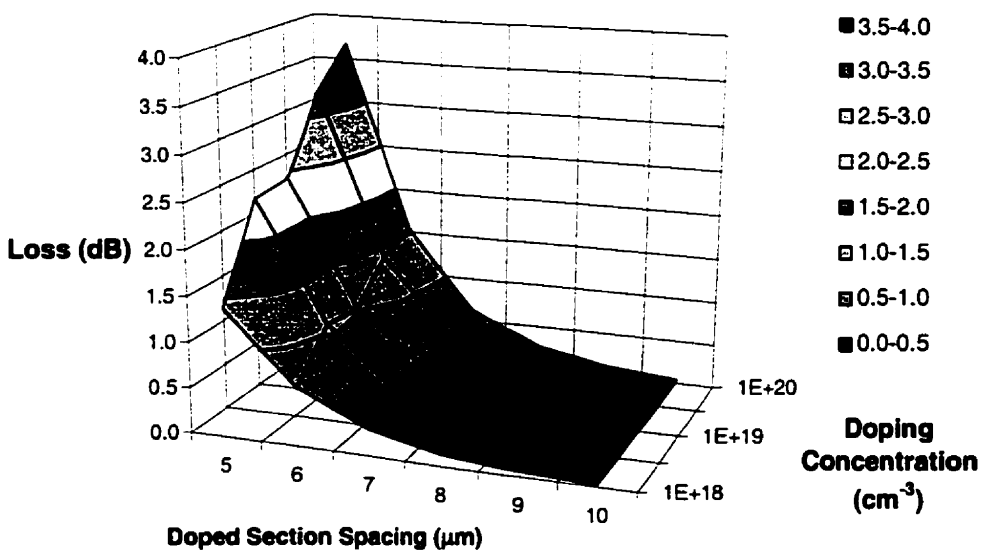


**Figure 2-24: Simulated results of the effect of doped section spacing and doping concentration on the off-state losses for a 1cm long device.**

To keep the off-state losses below 1dB, the loss due to absorption from the side regions should be less than 0.66dB, since 0.34dB has been lost due to mode mismatching with the input fibre.

These simulated results can be used to determine the optimal doping concentration and doped section spacing. They must be chosen to minimize the off-state losses and on-state power consumption while maximizing the device attenuation characteristics.

### 2.4.3 Diode Electronics

A PIN Diode is a PN junction with an intrinsic region in between the highly-doped P and N regions. Figure 2-25 shows the impurity distribution, space charge density and electric field distribution of a PIN diode.

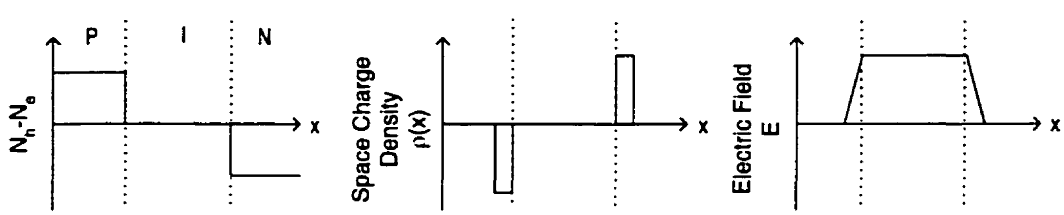


**Figure 2-25: Impurity distribution, space charge density, and electric field of a PIN diode [8].**

Under forward bias, holes will enter the intrinsic region from the P-I contact and electrons from the N-I contact. These holes and electrons will flow into the intrinsic region where they recombine. The carriers that are lost due to recombination must be injected from the P and N regions to satisfy the charge neutrality. This flow of injected carriers in the intrinsic region is the recombination current. The current density is given by:

$$J = \int_{-d}^{d} eRdx \qquad \textbf{2.42}$$

where $R$ is the recombination rate, equal to $N/\tau$. If $N'$ is the average injected electron concentration in the I region, then

$$J = \frac{eN'd}{\tau_a} \qquad \textbf{2.43}$$

where d is the intrinsic region width and $\tau_a$ is the ambipolar lifetime. If the carrier concentration throughout the intrinsic region is assumed to be constant, the diffusion current can be neglected. Since the injected carrier density is much higher than the intrinsic carrier density in the I region, the PIN diode is normally operated in high injection under forward bias. The total drift current is then:

$$J = e\mu_e N' E' + e\mu_h N' E'$$

$$= \frac{q}{kT}\frac{(b+1)^2}{2b} qD_a N' E', \qquad 2.44$$

where $b = \mu_e/\mu_h$, $D_a = 2D_e$ is the ambipolar diffusion coefficient, and E' is the average electric field in the intrinsic region. The voltage drop across the intrinsic region is:

$$V_I = E'd$$

$$= \frac{kT}{e}\frac{2b}{(1+b)^2}\left(\frac{d}{L_a}\right)^2, \qquad 2.45$$

where $L_a = \sqrt{D_a \tau_a}$ is the ambipolar diffusion length. The total applied voltage in forward bias will be equal to the sum of the voltage drop across the intrinsic region and the voltage drops across the P-I junction and the I-N junction:

$$V_A = V_P + V_I + V_N. \qquad 2.46$$

The sum of the drops across the junctions ($V_P + V_N$) is equal to the voltage drop across a PN junction. It can be shown that the voltage drop across the intrinsic region is very small and can be ignored [8]. For an injected carrier density of $10^{14}$ to $10^{18}/cm^3$, the ambipolar diffusion length will vary from 13.2µm to 5.3µm since it is proportional to the square root of the mobility and the lifetime which decrease with increasing carrier density. For an intrinsic region width of 7µm, $V_I$ will be from 0.003 to 0.02V for an injected carrier density of $10^{14}$ to $10^{18}/cm^3$, respectively. This voltage drop is small compared to the voltage drop across the junctions which is about 1V at the junction threshold, before current begins to flow. Therefore, the device will behave as a PN junction in the high injection regime.

The IV characteristics of the PIN diode with a small intrinsic region under high current injection can be found by using a modified PN junction diode equation. In these calculations, it is assumed that the P and N regions form abrupt junctions with the intrinsic region. The diode equation is given by:

$$I = I_o(e^{qV/kT} - 1) \qquad 2.47$$

where $I_o$ is the reverse-bias saturation current given by the equation:

$$I_o = qa\left(\frac{D_h}{L_h}p_n + \frac{D_e}{L_e}n_p\right). \qquad 2.48$$

In this equation, $a$ represents the diode junction area, which is the product of the doped region's length, multiplied by its height. The minority carrier concentrations in the depletion layers are given by $n_p$ and $p_n$ respectively and can be calculated using:

$$n_p = \frac{n_i^2}{p_p}, \qquad 2.49$$

$$p_n = \frac{n_i^2}{n_n}, \qquad 2.50$$

where $n_n$ and $p_p$ are the doping concentrations in the N and P regions, respectively.

Under high injection conditions, the minority carrier concentration in the depletion layers approaches the majority carrier concentration of the P and N regions and must be considered. This can be done by observing what happens to the Fermi levels when there is a high level of carriers in the depletion region. In the derivation of the diode equation, it was assumed that the separation of the Fermi levels everywhere must be less than or equal to the applied voltage,

$$n_p p_n \le n_i^2 \exp\frac{qV}{kT}, \qquad 2.51$$

where $n_i$ is the intrinsic carrier concentration. Substituting $n_p = p_p$ in 2.48 and $p_n = n_n$ in equation 2.49 will cause the current to become roughly proportional to $e^{qV/2kT}$ [8]. The diode equation for this device is then

$$I = I_o(e^{qV/2kT} - 1). \qquad 2.52$$

This equation can be used to determine the IV characteristics and power consumption of the attenuator with varying intrinsic region width and doping concentrations.

### 2.4.4 Device Attenuation Characteristics

As already mentioned, the current flow in the active region is due to the drift current from compensation of electron-hole recombinations. The rate of injected carriers can be expressed as:

$$R = \frac{\Delta N}{\tau} \tag{2.53}$$

where $\Delta N$ is the density of injected free-carriers, and $\tau$ is the recombination lifetime. When the device is forward biased, holes and electrons will be injected through the junction area into the active region volume. The carrier injection rate can also be expressed as:

$$R = \frac{I}{qda} \quad \text{or} \quad I = \frac{q\Delta N da}{\tau} \tag{2.54}$$

where $I$ is the forward bias current. The change in absorption coefficient with forward bias current can be found by equating 2.37 and equation 2.54:

$$\alpha = \frac{I\tau q^2\lambda^2}{4\pi^2 c^3 \varepsilon_o n d a}\left(\frac{1}{2m_e^2\mu_e} + \frac{1}{2m_h^2\mu_h}\right) + \alpha_{off} \tag{2.55}$$

where it has been assumed that equal amounts of holes and electrons are injected into the intrinsic region under forward bias. It is also assumed in these calculations that the attenuation is uniform across the device. The intrinsic absorption coefficient, $\alpha_{off}$, has been measured by Sze [8] and is about 0.023cm$^{-1}$. The change in absorption coefficient using Soref's model can also be found by equating 2.41 and 2.54.

$$\alpha = \left(1.45\times10^{17}\cdot\frac{I\tau}{qda}\right) + \alpha_{off} \tag{2.56}$$

The absorption coefficient is then multiplied by an overlap factor, which is the amount of overlap between the optical mode and the active region, shown in Figure 2-26.

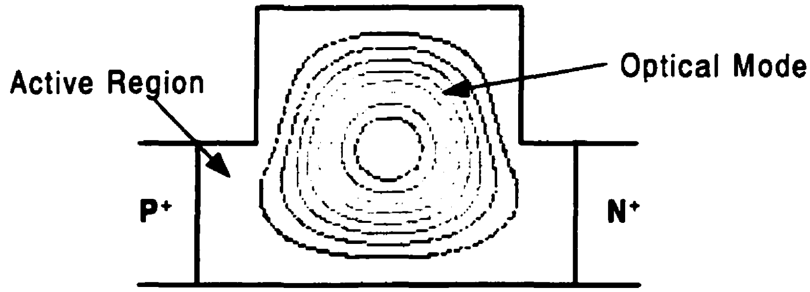


**Figure 2-26: Overlap of active region with optical mode. Only the section of the optical mode overlapping with the injected current area will experience attenuation.**

The overlap factor will depend on both the waveguide dimensions and the separation and depth of the doped sections. The mode shape will change with waveguide dimensions thus changing the overlap. It will also change as a function of current due to the change in refractive index. This is not a large effect since a carrier concentration of $10^{18}/cm^3$ causes a decrease in refractive index of $1.5x10^{-3}$ according to the Soref model and $8.3x10^{-4}$ according to the Drude model. The attenuation for a given absorption coefficient and overlap factor can be calculated using:

$$A = 10 \cdot \log(e^{-\delta\alpha z}) \qquad 2.57$$

where $A$ is the attenuation in dB, $z$ is the length of the device, $\alpha$ is the absorption coefficient, and $\delta$ is the overlap factor.

The attenuation was calculated for several intrinsic region widths using the optimal single-mode active region dimensions calculated in section 2.3.3. The intrinsic region width was varied from 6 to 8μm. These calculations were done using both the Drude model and Soref's model of free-carrier absorption. Results of these calculations are shown in Figure 2-27 and Figure 2-28.

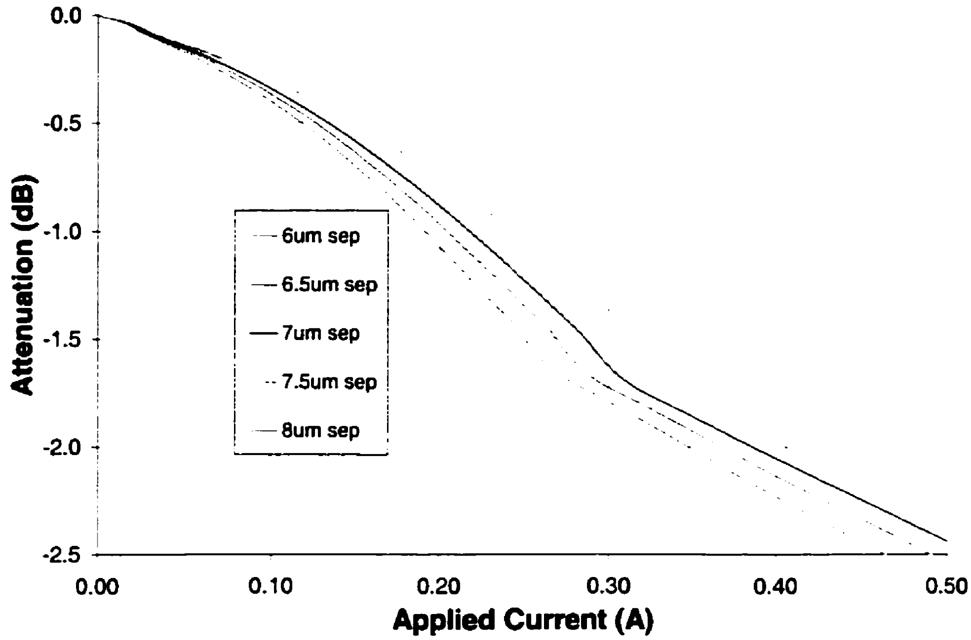


**Figure 2-27: Attenuation vs. applied current for varied intrinsic region width of a 1cm long device using the Drude model. The kink in the graph is due to the non-linearity of the carrier lifetime at that concentration.**

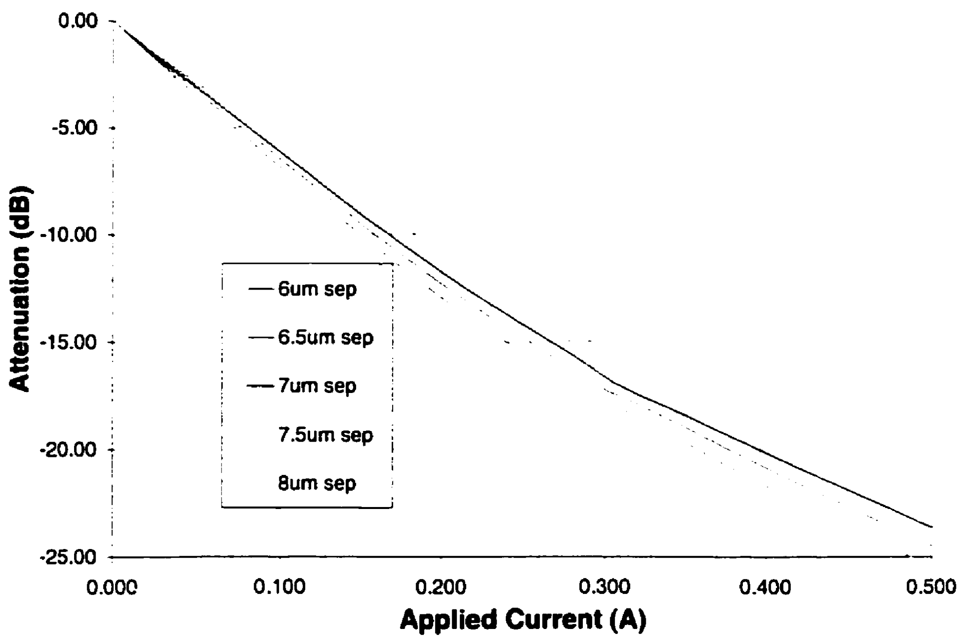


**Figure 2-28: Attenuation vs. applied current for varied intrinsic region width of a 1cm long device using the Soref model.**

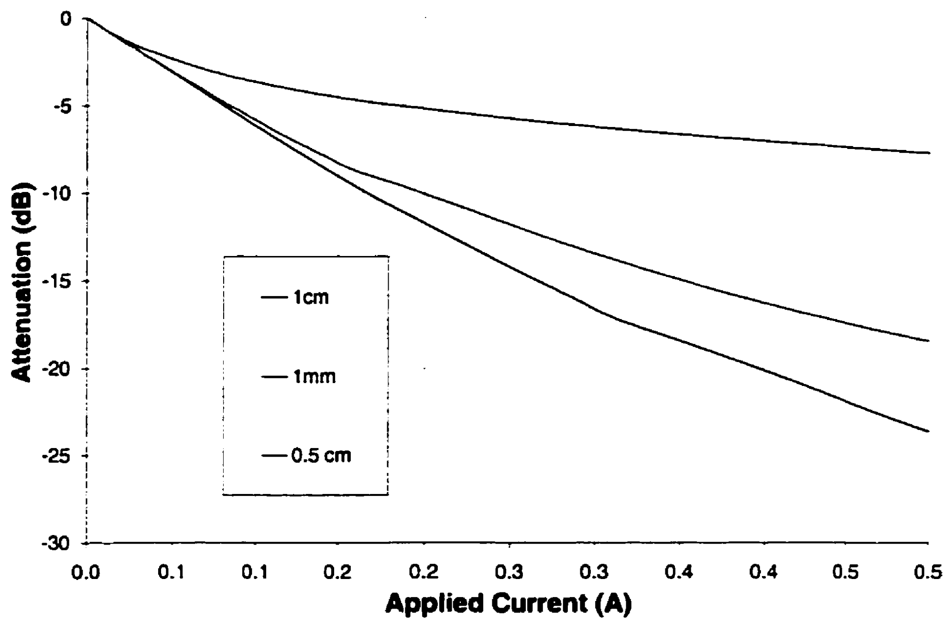


**Figure 2-29: Attenuation vs. applied current for different active region lengths. The attenuation for a given current level is greater for a longer device.**

It can be seen that as the intrinsic region width is increased, the attenuation level decreases for a given applied current, which is intuitive from equations 2.55 and 2.56. For an intrinsic region width of 7μm, the Drude model predicts an attenuation level of 2.5dB, where Soref's model predicts an attenuation level of 25dB. The Soref model is more accurate since it draws from experimental evidence and thus will be used for further calculations.

The effect of active region length was also simulated, shown in Figure 2-29. It can be seen that as the length of the device is increased, the attenuation level increases, which is intuitive from equation 2.57. Therefore, to achieve a high level of attenuation a longer active region length is desirable.

The device power consumption can be calculated using equation 2.51. There are three factors affecting the device power consumption; the width of the intrinsic region, the doping concentration of the P and N sections, and the active region length. These calculations are shown in Figure 2-30, Figure 2-31 and Figure 2-32.

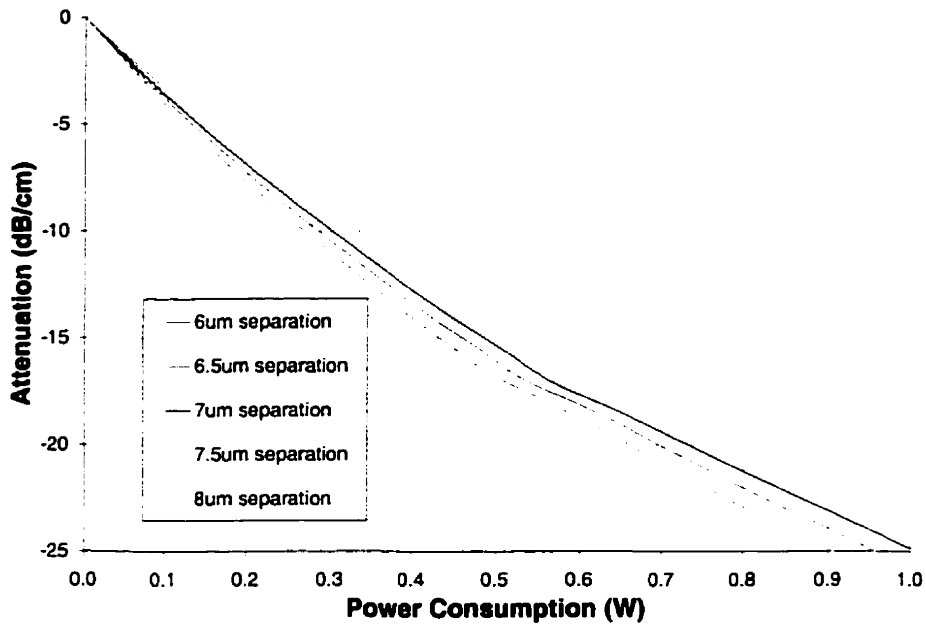


**Figure 2-30: Attenuation vs. power consumption for varying intrinsic region widths. A doping concentration of $10^{18}/cm^3$ for the P and N regions was used for these calculations.**

It can be seen that the power consumption for a given attenuation level decreases as the intrinsic region width increases, which arises from the dependency of the attenuation on the inverse of the intrinsic region width (equation 2.56). The power consumption is dependent on the doping concentrations as a result of equations 2.49 and 2.50, and it can be seen that as the doping concentration increases, the power consumption increases for a given attenuation level. The reverse saturation current, given in equation 2.48, is proportional to the active region area, making the power consumption dependant on the active region length. Therefore, a longer device is more desirable since it requires less power to achieve a given attenuation level.

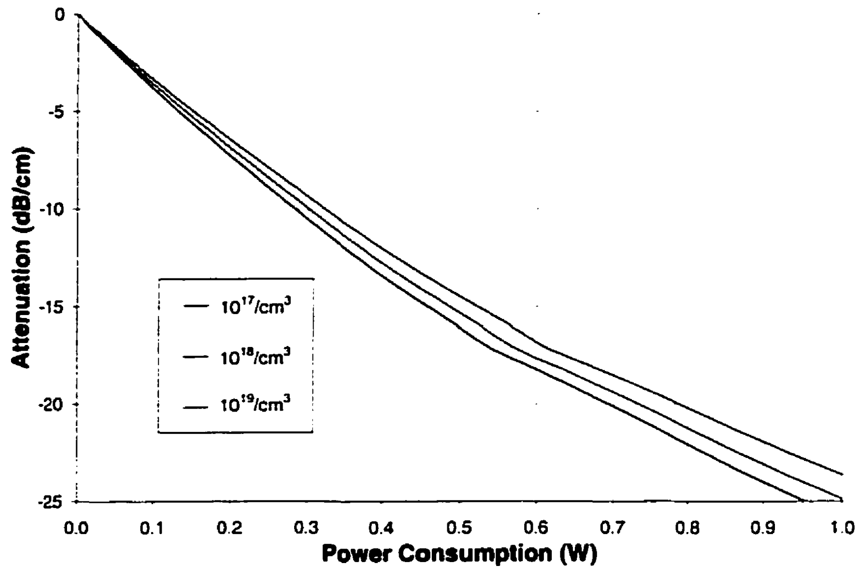


**Figure 2-31: Attenuation vs. power consumption for varying P and N region doping concentrations. An intrinsic region width of 7μm and a device length of 1cm were used for these calculations.**

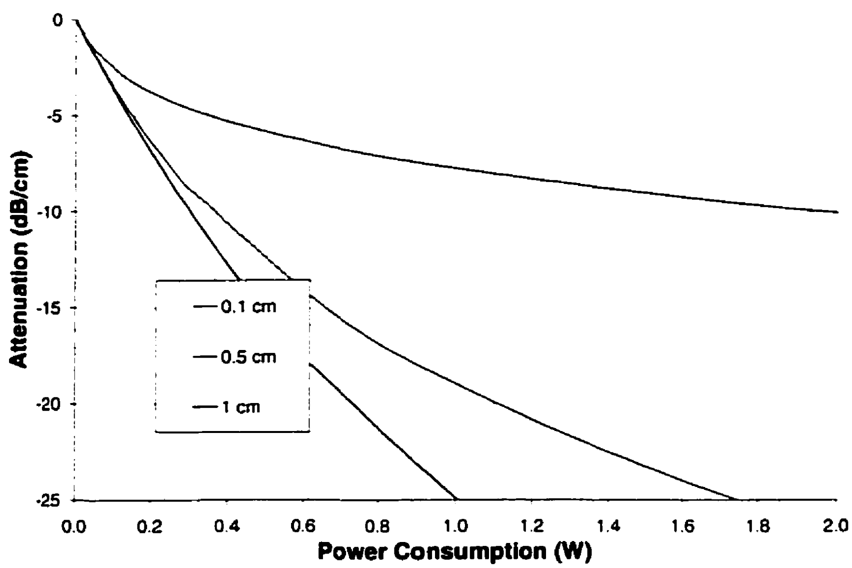


**Figure 2-32: Attenuation vs. power consumption for different device lengths. An intrinsic region width of 7μm and a doping concentration of $10^{18}/cm^3$ was used for these calculations.**

## 2.4.5 Optimal Device Configuration

The best possible configuration has many trade-offs and is partly driven by its application. What is desired is an attenuator with minimal loss in the off-state with a high level of attenuation and low power consumption in the on-state. To minimize off-state losses, the intrinsic region width must be sufficiently wide such that the mode passing through the active section in the off-state does not significantly overlap with the doped regions. The active region length must also be short such that any off state absorption will be minimal since the free carrier absorption present in the off state due to the doped regions is exponentially proportional to the active region length. Also, the doping concentration in the P and N sections must also be low since if there is some overlap of the optical mode, the loss resulting from free-carrier absorption in the active region will be minimal.

On the other hand, the power consumption in the on-state will be minimal if the intrinsic region is narrow, the active region is long and the doping concentration is low. This combination will require less power to achieve a high carrier concentration in the intrinsic region, thus achieving a high level of attenuation. Conversely, the carrier concentration in the intrinsic region can never be higher than that of the P and N regions, thus the doping concentration in the P and N regions must be sufficiently high to deliver a high enough carrier concentration to the intrinsic region under forward bias. Also, the attenuation level in the on-state will be higher for a given level of applied current if the intrinsic region is narrow and the active region is long. For a long narrow intrinsic region, a higher carrier density can be achieved and thus a higher level of attenuation for a given level of current.

One method of ranking a device's performance based on its parameters is to introduce a Figure of Merit. What is desirable is a large attenuation with low power consumption and low off-state losses. Taking these constraints into consideration, a figure of merit can be given to each configuration:

$$\text{Figure of Merit} = \text{FOM} = \frac{A}{P \cdot \ell} \qquad \textbf{2.58}$$

where A is the attenuation, P is the power consumption and $\ell$ is the off-state loss for a device with a doping concentration of $10^{18}/\text{cm}^3$, an applied forward current of 250mA. Since high attenuation and low power consumption are desirable, a high figure of merit is desirable. Obviously there are limits to this FOM formula; infinite power is not acceptable in order to achieve zero off-state losses, and neither is increasing the intrinsic region width indefinitely. The FOM was calculated for three doped section lengths, five intrinsic region widths, and three doping concentrations. The results of these calculations are shown in Figure 2-33.

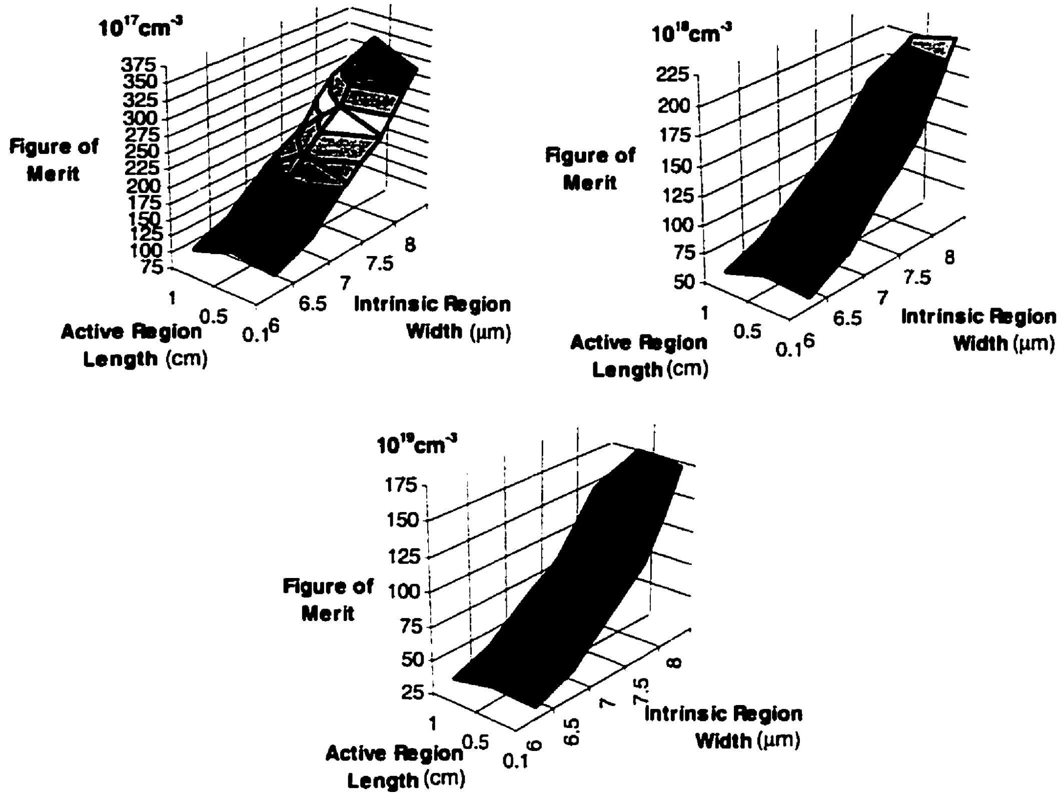


**Figure 2-33: Figure of Merit calculations for devices varying in intrinsic region width, active region length, and doping concentration. Devices having a wide intrinsic region, low doping concentration, and active region length of 0.5cm have the highest FOM.**

As the intrinsic region width increases and the doping concentration decreases, the figure of merit increases due to a decrease in insertion loss and power consumption. Obviously there are limits to this FOM formula; infinite power is not acceptable in order to achieve zero off-state losses. Also, one can not increase the intrinsic region width indefinitely. The figure of merit of a device was taken into account when determining the optimal device configuration.

The target specifications for the attenuator for the purposes of this thesis are as follows: maximum off-state loss of 1dB, attenuation level of 20dB, and maximum power consumption of 1W. The optimal design to meet these specifications has an intrinsic region width of 7μm with an active region length of 1cm and doping level of

$10^{18}/cm^3$. This design also gives a high Figure of Merit. The optimal design is shown in Figure 2-34.

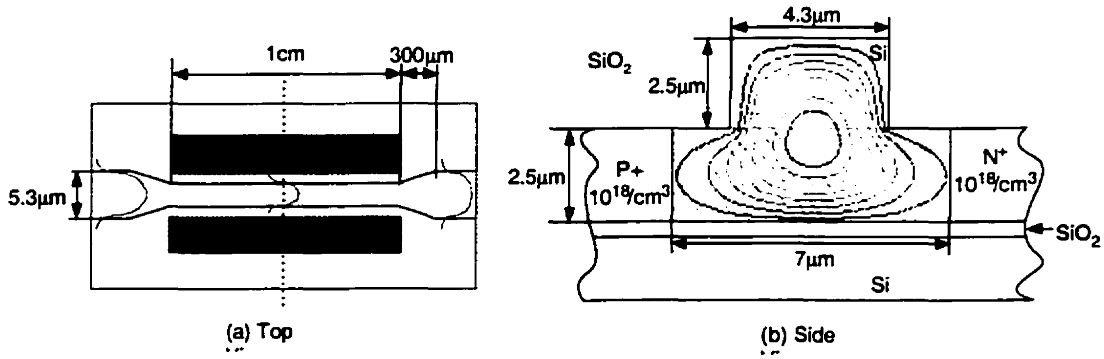


**Figure 2-34: Optimal device design for on-state power consumption of 1W, 20dB attenuation range, and 1dB off-state loss using the theoretical results presented.**

The theory and calculations discussed in this chapter will be compared to experimental results in the next chapter from fabricated devices. The design shown above will be proven to be optimal.

### *References*

[1] J.P. Coligne, "Silicon on Insulator Technology: Materials to VLSI," Kluwer Academic Publishers, Boston, 1991 ISBN 0-7923-9150-0.

[2] T. Zinke, U. Fischer, A. Splett, B. Schüppert, K. Petermann, "Comparison of Optical Waveguide Losses in Silicon-on-Insulator," IEE Electronics Letters, vol. 29, no. 23, Nov. 11, 1993.

[3] K. Petermann, "Properties of Optical Rib-Guides with Large Cross Section," Archiv fur Electronik und Ubertragungstechnik, (Germany), vol. 30, pp. 139-140, 1976.

[4] R. A. Soref, J. Schmidtchen, K. Petermann, "Large Single Mode Rib Waveguides in GeSi-Si and Si-on-$SiO_2$," IEEE Journal of Quantum Electronics, vol. 27, no. 8, pp. 1971-1974, Aug. 1991.

[5] R. Baets, P.E. Lagasse, "Calculation of Radiation Loss in Integrated-Optic Tapers and Y-Junctions," Applied Optics, vol. 21, no. 11, pp. 1972-1978, June 1982.

[6] P.K. Basu, "Theory of Optical Processes in Semiconductors – Bulk and Microstructures," Clarendon Press, Oxford, 1997, ISBN 0-19-851788-2, pp. 122-129.

[7] R.A. Soref, B. R. Bennett, "Electro-optical Effects in Silicon," IEEE Journal of Quantum Electronics, vol. 23, no. 1, pp. 123-129, Jan 1987.

[8] S.M. Sze, "Physics of Semiconductor Devices", 2dn Ed. John Wiley & Sons, New York, 1981, ISBN 0-471-05661-8, pp. 27-30, 89-93, 207-209.

[9] R. A. Sinton and R. M. Swanson, "Recombination in highly injected Si," IEEE Trans. Electron Devices, vol. 34, 1380, 1987.

[10] N. W. Ashcroft, N. D. Mermin, "Solid State Physics," Saunders College Publishing, New York, 1976, ISBN 0-03-083993-9, pp. 2-27.

[11] "Theory of Dielectric Optical Waveguides", Marcuse

# 3 Experimental Devices

Several devices were received from a supplier for analysis. The dimensions of these devices varied, and none were fabricated at the optimal configuration arrived at in the previous chapter. However, analysis of these devices proved the theory developed in Chapter 2 and provides useful information about the devices' characteristics.

The dimensions of the tested devices are shown in Figure 3-1. Tapers were used to reduce the size of the optical mode traveling from the input facet to the active region.

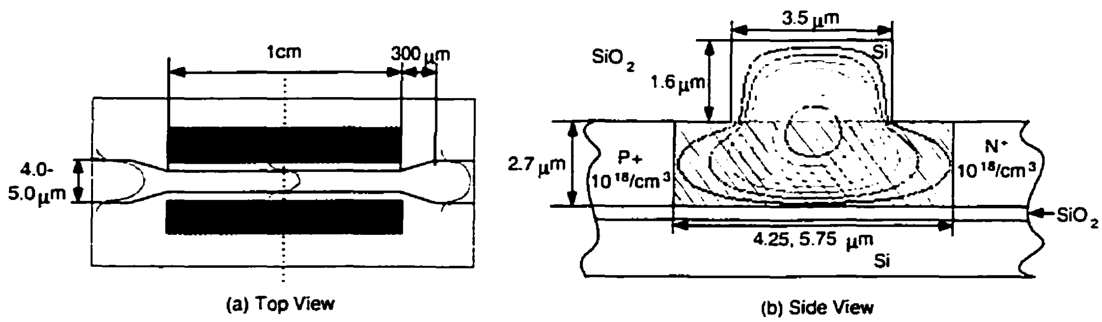


**Figure 3-1: Tested devices. The input facets ranged from 4.0 to 4.8μm. The doped sections were placed 4.25 and 5.75μm apart.**

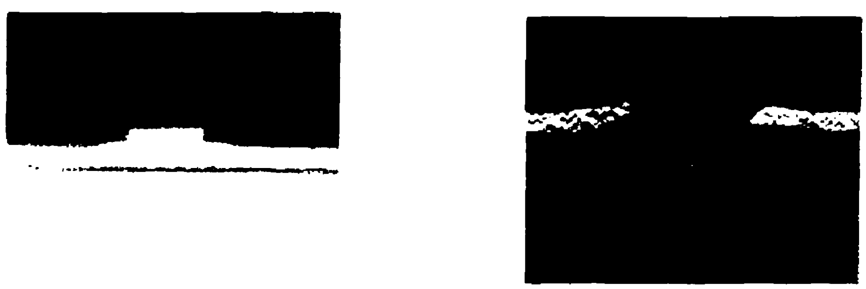

(a) (b)

**Figure 3-2: (a) end-facet of 5.0μm waveguide (b) 4.25μm wide intrinsic region showing metallization over doped sections.**

In these devices, both the passive coupling and attenuating regions are single mode. The input top ridge width was varied from 4.0μm to 4.8μm in 0.2μm steps. The intrinsic region had two different widths; 4.25μm and 5.75μm. 100X magnification pictures of the end facet and middle of the devices are shown in Figure 3-2

## 3.1 Device Preparation

The devices obtained were cleaved into chips consisting of three attenuators and three passive waveguides. Once received, the end facets were polished and anti-reflection (AR) coated to eliminate losses due to Fresnel reflections at the interface between the fibre and the waveguide.

Glass caps were glued on the top and the bottom of the chip so they could be easily held in a jig and were protected against breakage. They were then polished one chip at a time in a special jig on a Seiko-Giken polishing machine to create a smooth end-face. Several diamond polishing pads were used with different grit size, resulting in a polishing quality better than 0.05μm.

Without AR coating there would be losses due to Fresnel reflections since the refractive index of the waveguide is not equal to the refractive index of the fibre. The Fresnel equations give the reflection and transmission coefficients. The reflection (transmission) coefficient is the ratio of the reflected (transmitted) electric field amplitudes to the incident electric field amplitudes. For normal incidence, these are given by [1]:

$$r = \frac{E_r}{E_i} = \frac{1-n}{1+n} \qquad 3.1$$

where $n = n_2/n_1$ is the relative refractive index. The fraction of power in the incident wave that is reflected or transmitted is given by the reflectance and the transmittance, respectively. These are given by [1]:

$$R = \frac{P_r}{P_i} = r^2 \qquad 3.2$$

$$T = \frac{P_t}{P_i} = 1 - R \qquad 3.3$$

The refractive indices of the silicon waveguide and of the fibre core at a wavelength of 1500nm are 3.476 and 1.56, respectively. Therefore the percentage of optical power traveling from the silicon waveguide into the fibre therefore would be equal to 85.52%, giving a loss of 0.68dB per facet. AR coating the waveguide facets after polishing can reduce these losses.

A multi-layer AR coating is best described by first considering the reflections from a single film deposited on a substrate of index $n_s$, illustrated in Figure 3-3. A beam of light from a material of index $n_o$ incident on the surface of the film of higher index $n_f$ will divide into two parts, one that is reflected and one that is transmitted.

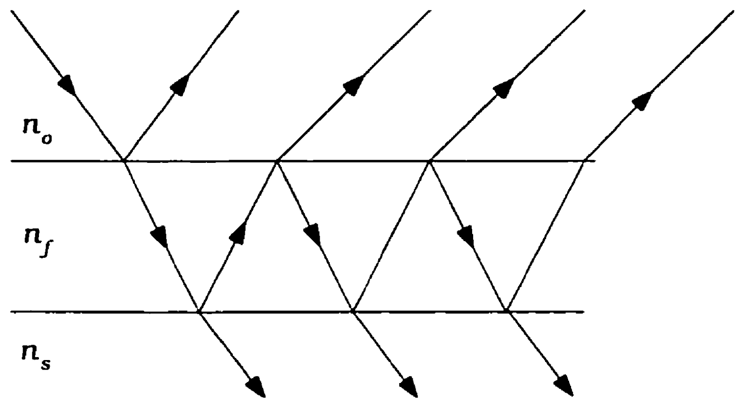


**Figure 3-3: Reflections from a single film. It is assumed that $n_f > n_o$. The rays may also pass through the film. The multiple reflected beams will recombine and interfere constructively or destructively depending on the relative phase difference.**

The beam transmitted through the thin film will be reflected from the second interface and may experience multiple reflections within the film depending on the angle of incidence. The multiple reflected beams will recombine and interfere. Since they have traveled different paths, a relative phase difference results that can produce either constructive or destructive interference. The additional optical path traveled by the beams reflected from the second interface is:

$$\Delta = n(2t) \tag{3.4}$$

where $t$ is the thickness of the film and $n = n_o/n_f$. If $n_s > n_f$, then there will be no relative phase shift between the two reflected beams since a $\pi$ phase change occurs on external reflections. The type of interference will only depend on the optical path difference. If the incident material is air, and the film thickness is $\lambda_f/4$ where $\lambda_f$ is the wavelength in the film, then $2t = \lambda_f/2$ and the optical path difference will be $2n_ft = \lambda_o/2$ since $\lambda_o = n_fn_s$. Destructive interference will occur at the wavelength $\lambda_o$. The reflectance is given by

$$R = \left( \frac{n_o n_s - n_f^2}{n_o n_s + n_f^2} \right)^2 . \quad 3.5$$

This equation was obtained by applying the transfer matrix describing the reflection from two interfaces to equation 3.1. The reflectance will be zero if the index of the film is $n_f = \sqrt{n_o n_s}$ .

Since durable coating materials with arbitrary refractive indices are not generally available and a single film only produces zero reflectance at one wavelength, multi-layer films are often used to create a broader low reflectance region. For a three-layer film having quarter- wave thicknesses and indices $n_1$, $n_2$, and $n_3$, it can be shown that zero reflectance occurs when the film indices satisfy

$$\frac{n_1 n_3}{n_2} = \sqrt{n_o n_s} . \quad 3.6$$

By increasing the number of films, the wavelength range of low reflectance can be broadened.

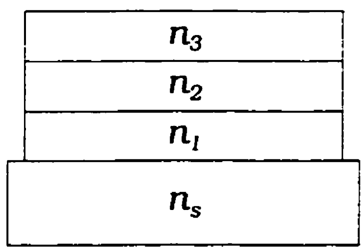


**Figure 3-4: Three layer antireflection coating. The substrate being coated has index $n_s$. All film layers have a thickness of $\lambda_f/4$.**

By using AR coatings, the reflectance at a wavelength of choice can be decreased, and therefore the losses at both the input and output of the device can be reduced.

## *3.2 Experimental Set-up*

The insertion losses, polarization dependent loss (PDL), attenuation with applied current, wavelength flatness, and response time were measured for several devices. The experimental set-up is shown in Figure 3-1.

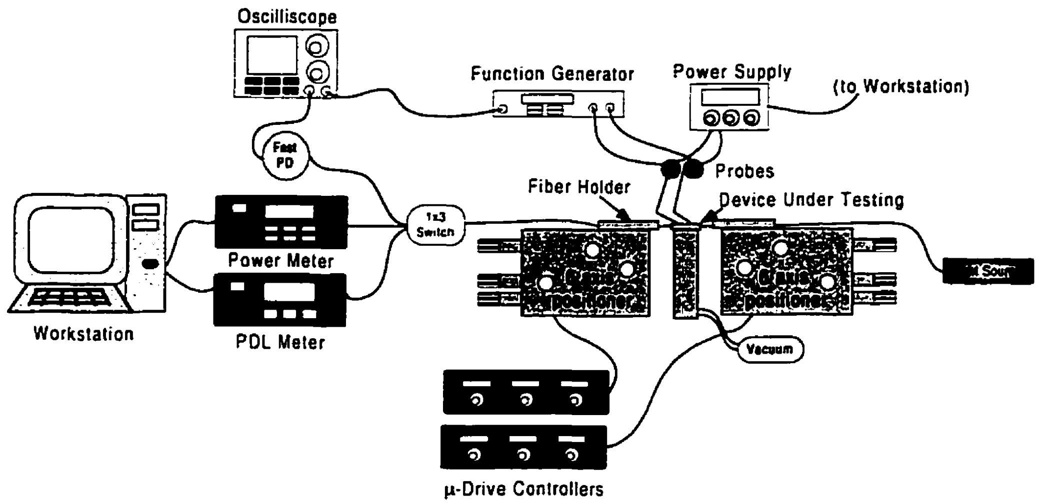


**Figure 3-1: Experimental Set-up. The device was not probed during insertion loss measurements.**

The chip was held in a vacuum chuck and aligned to the fibres using two six-axis piezo-controllable positioners. Index-matching oil was used between the fibre and the waveguide to fill any air gaps. For the insertion loss measurements, a HeNe laser was first used for rough alignment of the fibre to the end of the guide on each side. When partially aligned, the visible light can be seen propagating down a few millimeters of the coupling section of the waveguide. A 1550nm diode laser was used for the insertion loss measurements since the device is optimized for that wavelength. The insertion losses were then read from a Newport 2032-C power meter. PDL was measured using a JDS PS3 meter.

Current was applied to the devices by a power supply connected to probes. The probes were applied to metal contact pads on the edges of the chips. The insertion losses, PDL and applied current were recorded on the workstation through GPIB interfaces. A program was written to control the current applied to the device while reading the attenuation and PDL.

To measure wavelength flatness a JDS Uniphase Swept Wavelength System (SWS) was used. Different current values were applied to measure the losses with wavelength at different attenuation levels on the SWS.

The response time was measured by applying a square wave to the current injected into the device by an HP function generator. A fast photodiode was used to measure the fluctuations in the device's output power. The output current pulses of the fast photodiode and the function generator were observed and compared on the oscilloscope. From these observations, the response time of the devices was calculated.

## *3.3 Experimental Results*

### 3.3.1 Insertion Losses

Figure 3-5 shows insertion loss measurements for devices on two different chips.

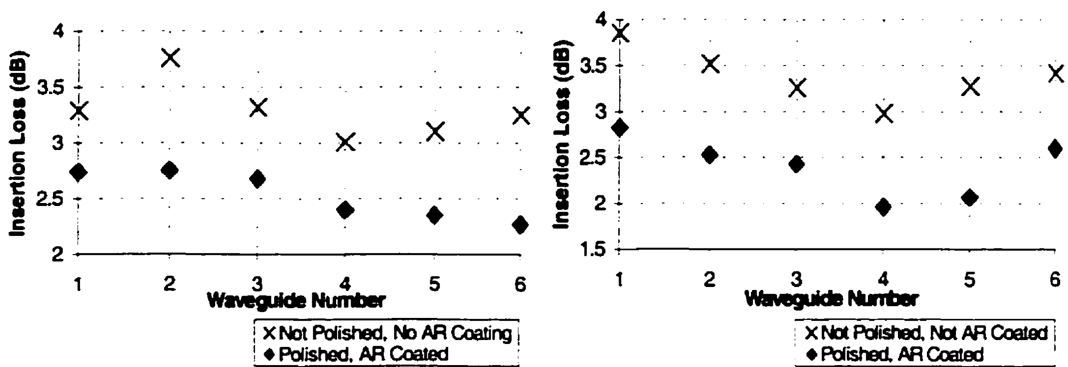


**Figure 3-5: Insertion loss measurements for two different chips. Waveguide numbers 1 to 3 are attenuators. The remaining are passive waveguides used for comparative loss measurements. Losses decreased as a result of AR coating the facets.**

All insertion loss measurements are summarized in Tables 1-4. The insertion losses were dependant on the facet preparation, interface width, and intrinsic region width.

#### *3.3.1.1 Facet Preparation*

The insertion losses were measured at three stages of device preparation; before polishing, after polishing, and after AR coating to determine the gain from these procedures. Table 2 shows insertion loss measurement statistics for passive waveguides of all interface widths. The differences in losses between unpolished, non-AR coated and AR coated waveguides were calculated for each interface width of the passive waveguides. From these data, it can be seen that the losses decreased considerably after AR coating. Polishing the end facets did not have any significant effect on the insertion losses which was expected since the devices were cleaved upon receiving. Polishing was still required after the glass caps were glued on the top and bottom of the chips such that the glass caps were flush with the ends of the chips.

**Table 2: Insertion Loss Measurement Statistics: Passive Waveguides, all interface widths**

| *Type* | *Number of Samples Measured* | *Average Loss Difference (dB)* | *Standard Deviation (dB)* |
|---|---|---|---|
| Not Polished, Not AR Coated | 24 | -- | -- |
| Polished, Not AR Coated | 9 | -0.025 | 1.3E-3 |
| Polished, AR Coated | 21 | -1.03 | 0.154 |

### *3.3.1.2 Interface Width*

Five different interface widths were tested varying from 4.0μm to 4.8μm to determine the best interface width for low coupling losses. The mode field shapes of a specialty fibre and a waveguide with a 4.0μm interface width is shown in Figure 3-6. The passive waveguides were measured after AR coating for a comparison of the losses due to mode mismatch. Table 3 shows the results of these measurements.

The losses due to mode mismatch were modeled, shown in Figure 3-7, for comparison against the experimental data.

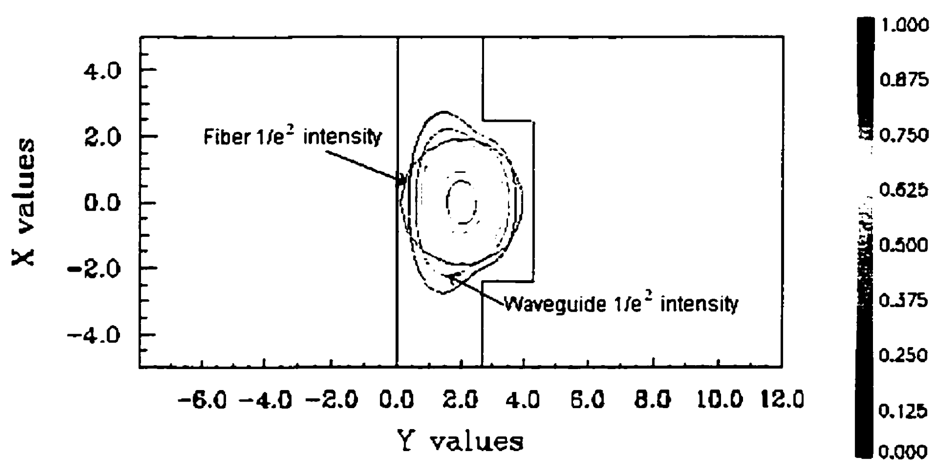


**Figure 3-6: Waveguide and fibre MFD for experimental devices. The mode field of the waveguide has a different shape than that shown in Figure 2-11 of Chapter 2 since this waveguide has a thinner ridge and a thicker slab.**

The losses due to mode mismatch were found by calculating the overlap integral of the fibre and waveguide mode fields for each interface width. These values are different from those calculated in Chapter 2 since these waveguides have different shapes.

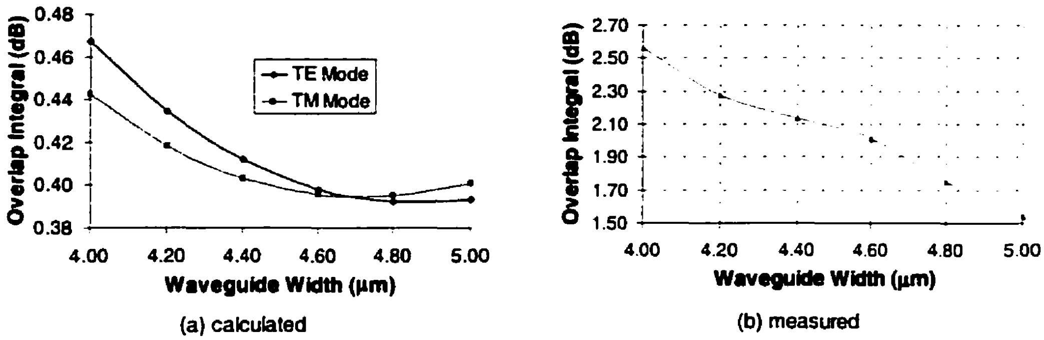


**Figure 3-7: (a) calculated and (b) measured losses due to mismatch of 4µm specialty fibre mode and waveguide mode of tested devices. The calculated losses varied from 0.39dB/facet to 0.47dB/facet. Experimental data followed the same trend, varying from 2.56dB/facet to 1.75dB/facet.**

It can be seen that the measured data follows the same trend as the calculated overlap integrals. However, there is an order of magnitude difference between the measured and calculated difference in losses between the best and worse case overlap integrals. This indicates that the losses are not due to the interface width alone, there is another contributing factor such as free-carrier absorption from the doped sections. As the interface width increases, the mode will overlap more with the doped section resulting in higher losses. Nonetheless, the fibre mode best matches the waveguide mode with the 4.8µm wide interface. The calculated losses show a minimum for the TM mode and least difference in TE and TM mode loss at a waveguide width of approximately 4.8µm.

**Table 3: Insertion Loss Measurement Statistics: Passive Waveguides AR coated**

| *Interface width (µm)* | *Number of Devices Measured* | *Average Loss (dB)* | *Standard Deviation (dB)* |
|---|---|---|---|
| 4.0 | 6 | 2.56 | 0.167 |
| 4.2 | 24 | 2.28 | 0.003 |
| 4.4 | 10 | 2.13 | 0.012 |
| 4.6 | 6 | 2.01 | 0.086 |
| 4.8 | 3 | 1.75 | 0.073 |

### *3.3.1.3 Intrinsic Region Width*

To determine the effect of the intrinsic region width on insertion losses, the losses were measured for AR coated devices having the same interface width, but different intrinsic region widths.

**Table 4: Insertion Loss Measurement Statistics: Active devices, polished, AR coated, 4.2μm interface width**

| *Intrinsic width* | *Number of Devices Measured* | *Average Loss (dB)* | *Standard Deviation (dB)* |
|---|---|---|---|
| 5.75μm | 6 | 2.66 | 0.027 |
| 4.25μm | 6 | 2.86 | 0.056 |

The AR coated devices with diodes placed 4.25μm apart had insertion losses 0.2 ± 0.029dB greater than those AR coated devices with diodes placed 5.75μm apart. As expected from the theory of Chapter 2, the insertion losses increase as the width of the intrinsic region decreases. The insertion loss difference calculated theoretically for these diode spacings was 0.54dB.

The experimental data of Table 4 includes losses due to mode mismatch. For an interface of 4.2μm this was measured to be 2.28dB, leaving 0.58dB and 0.38dB losses due to absorption in the active region for intrinsic region widths of 4.25μm and 5.75μm, respectively.

The doping concentrations and profiles of the devices tested were not disclosed by the supplier due to proprietary information issues. Therefore, a wide range of doping concentrations and diode spacings were used for theoretical analysis of the insertion losses and attenuation characteristics. As seen in chapter 2, the insertion losses of the attenuator in the off-state depends on both the doping concentration and the intrinsic region width. This was calculated for the structure of the devices tested, shown in Figure 3-8. These calculated off-state losses are higher than for the structure calculated in Chapter 2 since the slab is thicker, the ratio of slab height to rib height is greater, and the rib is not as wide. This causes the mode to spread out more in the slab region, resulting in more overlap with the doped section and thus higher losses.

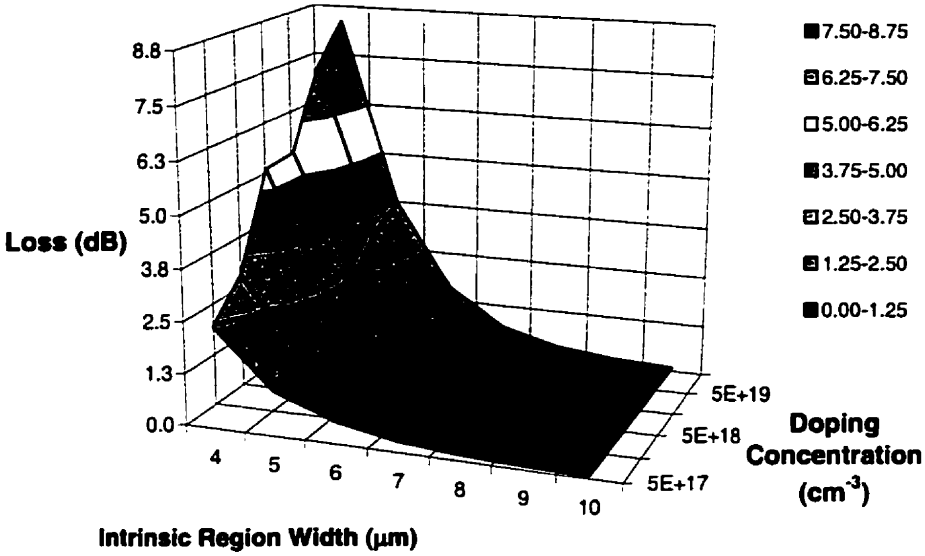


**Figure 3-8: Insertion losses with intrinsic region width and doping concentration for the structure of the devices tested. The structure of these devices is different from those discussed in Chapter 2 since these devices have a different shape. Therefore the mode is a different shape, resulting in different loss values for the same doped section spacing and concentration.**

The range at which an impurity reaches full concentration in a junction in a semiconductor can vary from a few hundred angstroms to 1μm. If the junction is fabricated by ion implantation, this range is depending on the type of impurity and its implantation energy. If the junction is fabricated by diffusion, the depth at which the impurity reaches full concentration is dependant on the diffusion temperature, impurity type and exposure time. Therefore, the intrinsic region widths may actually be different from 4.25μm and 5.75μm depending on how the junction was formed. The measured losses due to absorption is smaller than the calculated losses since the calculations assumed an abrupt junction. If the losses for a diffused junction were simulated, the losses due to absorption would also be smaller since the doped sections do not reach the full concentration until further away from the intrinsic region.

There is a large number of doping concentration and intrinsic region width combinations to arrive at the insertion loss due to off-state absorption measured. For an insertion loss of 0.38dB, the diode separation and corresponding doping concentration can range from 6.54μm at $5\mathrm{x}10^{17}/\mathrm{cm}^3$ to 7.65μm at $10^{20}/\mathrm{cm}^3$. For an insertion loss of 0.58dB, the diode separation and corresponding doping concentration can range from 5.92μm at $5x10^{17}/cm^3$ to 7.23μm at $10^{20}/cm^3$. These ranges of doping concentrations and intrinsic region widths will be used in the attenuation and power consumption theoretical analysis of these devices.

### *3.3.1.4 Tolerance Analysis – Insertion Losses*

The attenuator insertion losses in the off-state is dependent upon a number of factors. At the input of the device, the coupling losses could increase or decrease depending on the waveguide shape. The polishing and AR coating quality could affect the input coupling efficiency. The shape of the waveguide, width of the intrinsic region, and diode doping concentration in the attenuation region of the device can affect the propagation losses. The quality of silicon used could also influence the insertion losses by scattering due to defects. The etch quality of the waveguide ridge could also affect the losses. Several calculations were done to analyze the effects of typical fabrication tolerances on the insertion losses. The active devices with an interface width of 4.2μm and intrinsic region widths of 4.25μm and 5.75μm were analyzed theoretically to compare with the experimental devices. A ±0.2μm tolerance was used for uncertainties due to mask writing, lithography, and etching. Results of the tolerance analysis calculations are shown in Table 5 and Table 5 for the cases with the lowest and highest losses, respectively.

**Table 5: Insertion loss tolerance analysis - worst case scenario**

| *Parameter* | *Amount Changed* | *Effect (dB)* |
|---|---|---|
| Rib Width | -0.2μm | +0.041 |
| Slab Height | +0.2μm | +0.086 |
| Rib Width, Slab Height | -0.2μm, +0.2μm | +0.128 |
| AR Coating | +1 standard deviation | +0.154 |
| Intrinsic Region Width, 4.25μm | -0.4μm | +0.614 |
| Intrinsic Region Width, 5.75μm | -0.4μm | +0.196 |
| Active Region, 4.25μm | +0.2μm rib, +0.2μm slab | +1.31 |
| Active Region, 5.75μm | +0.2μm rib, +0.2μm slab | +0.211 |
| Doping Concentration, 5.25μm | +30% | +0.114 |
| Doping Concentration, 6.75μm | +30% | +0.026 |
| Device Length | +1mm | +0.11 |

**Table 6: Insertion loss tolerance analysis - best case scenario**

| *Parameter* | *Amount Changed* | *Effect (dB)* |
|---|---|---|
| Rib Width | +0.2μm | -0.022 |
| Slab Height | -0.2μm | -0.038 |
| Rib Width, Slab Height | +0.2μm, -0.2μm | -0.055 |
| AR Coating | -1 standard deviation | -0.154 |
| Polish | -1 standard deviation | -0.001 |
| Intrinsic Region Width, 4.25μm | 6.65μm | -0.859 |
| Intrinsic Region Width, 5.75μm | 8.15μm | -0.256 |
| Active Region, 4.25μm | -0.2μm rib, -0.2μm slab | -0.282 |
| Active Region, 5.75μm | -0.2μm rib, -0.2μm slab | -0.045 |
| Doping Concentration, 4.25μm | -30% | -0.176 |
| Doping Concentration, 5.75μm | -30% | -0.048 |
| Device Length | -1mm | -0.11 |

The first parameters considered in the analysis were the waveguide dimensions at the interface. According to Figure 3-7, as the width of the rib is decreased, the losses due to mode mismatch at the input increases. Also, as noticed in the BPM overlap integral simulations, as the lower slab height increases, the losses due to mode mismatch increases. When these dimensions are changed as such, the mode spreads out more into the slab region of the waveguide and becomes less circular in shape. The total height could also change, which would affect the coupling losses as well. The largest increase and decrease in mode mismatch losses due to processing tolerances are +0.128dB and –0.055dB, respectively.

The AR coating quality could also increase or decrease the insertion losses. From Table 2, the insertion losses of polished devices with and without AR coating had standard deviations of 0.001dB and 0.054dB, respectively. Using these measured statistics, the quality of AR coating would lead to an increase or decrease of 0.054dB. Therefore, the effect of the polish quality on the insertion losses is negligible according to the measured statistics since the quality of polish was fairly constant.

The next parameter considered was the intrinsic region width. Consider a long projected range of the impurity during junction formation. The impurity may not reach full concentration until 0.5μm into the junction. Assuming a constant doping concentration of $10^{18}/cm^3$, this would result in a decrease in insertion losses of 2.79dB for the 4.25μm marked waveguide width and 0.63dB for the 5.75μm marked waveguide. If the intrinsic region width were decreased by 0.4μm due to processing tolerances (0.2μm on each side), the intrinsic region width would actually be 3.85μm and 5.35μm for devices marked with 4.25μm and 5.75μm intrinsic region widths, respectively. This would increase the losses by 0.614dB and 0.196dB for the 4.25μm and 5.75μm marked devices, respectively. Conversely, if the processing tolerances increased the intrinsic region width by 0.4μm, the doped sections would be 4.65μm and 6.15μm apart resulting in a decrease in insertion losses of 0.859dB and 0.256dB, respectively.

The effect on the insertion losses due to the shape of the waveguide in the attenuating region was also taken into account. If the rib width and slab height are increased, the amount of mode power in the slab section of the waveguide increases. This would lead to an increase in absorptive losses in the active region due to absorption in the P and N regions since more of the mode overlaps with these regions. An increase in rib width and slab height of 0.2μm would result in an increase in propagation losses of 1.31dB for a 4.25μm intrinsic region width, and 0.21dB for a 5.75μm intrinsic region width. Alternatively, a decrease in rib width and slab height would result in a decrease in propagation losses of 0.282dB for a 4.25μm intrinsic region width and 0.0451 for as 6.75μm intrinsic region width. This is because the amount of optical power in the slab region has decreased.

As seen in Figure 3-8, the range of doping concentration can also have an effect on the insertion losses. A processing tolerance of ±30% is assumed. By increasing the doping concentration from $1.0x0^{18}cm^{-3}$ to $1.3x10^{18}cm^{-3}$, the losses increase by 0.17dB for the 4.25μm intrinsic region width and 0.03dB for a 5.75μm intrinsic region width. This is because the losses due to absorption in the intrinsic region are proportional to the doping concentration of the material. Therefore, as the doping concentration of the P and N regions is increased, the insertion losses increase and vice-versa. As the intrinsic region width is increased, the effect of doping concentration on the absorption losses decreases.

The last parameter to be considered is the device length. Since the amount of free-carrier absorption in the off-state is proportional to the length of the device, increasing the device length would therefore increase the absorptive loss. The length of the experimental devices was determined by measuring the length of the metallization on either side of the centre ridge. This assumed that the dopant was deposited under the full length of the metallization. If the dopant extended beyond the metallization or vice-versa the device length was not determined properly and the loss calculations are effected. A measurement uncertainty of 1mm in determining the device length by a microscope measurement is assumed here. By varying the device length by 1mm, the loss due to absorption can vary by 0.11dB.

Any of the changes in the parameters analyzed could occur simultaneously, increasing the insertion losses significantly. The most significant increases in insertion losses are due to the effects of the intrinsic region width and shape of the mode in the attenuating region. The critical parameters to control, therefore, are the doping process and etching of the centre rib such that the intrinsic region width and mode shape do not vary significantly. The worst case scenario would amount to a total increase in loss of 2.99dB. The best case scenario would amount to a total decrease in loss of 2.05dB.

### 3.3.2 Wavelength Dependence

According to the Drude model of free-carrier absorption, the attenuation is proportional to the square of the wavelength:

$$\Delta\alpha = \frac{q^3\lambda^2}{4\pi^2\varepsilon_o c^3 n}\left(\frac{\Delta N_e}{m_e^2\mu_e} + \frac{\Delta N_h}{m_h^2\mu_h}\right) \qquad 3.7$$

A theoretical plot of the wavelength dependency on the attenuation is shown in Figure 3-9. The wavelength flatness was also measured experimentally, shown in Figure 3-10. Wavelength flatness is defined here as the change in attenuation with wavelength over the shown range. The wavelength dependence on injected current is shown for the Drude model and the measured devices in Figure 3-12.

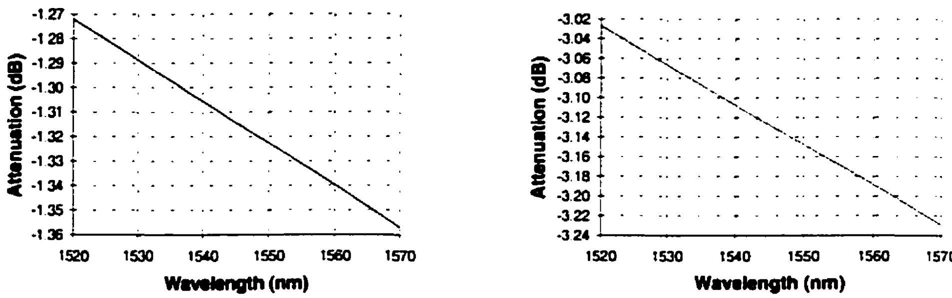


(a) (b)

**Figure 3-9: Wavelength dependency on attenuation calculated using the Drude model of free-carrier absorption. The wavelength variation for 100mA of applied current (a) is 0.09dB. As the applied current is increased, the wavelength variation also increases; for 200mA of applied current the wavelength variation increases to 0.2dB. The attenuation depth in both (a) and (b) are not correct since the Drude model does not accurately predict the level of attenuation, as discussed in Chapter 2.**

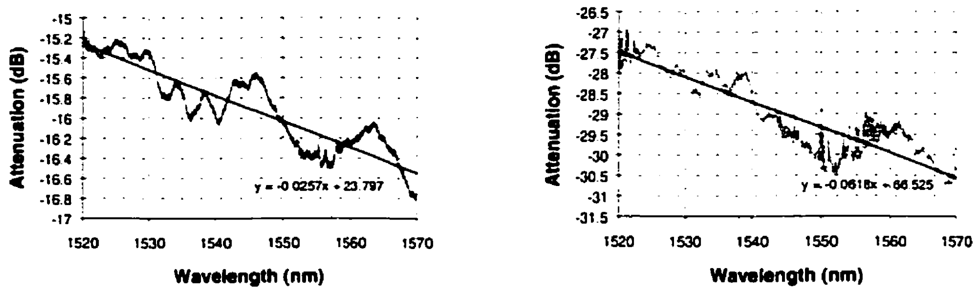


(a) (b)

**Figure 3-10: Wavelength flatness measured for a device with 4.25μm separated diodes. 100mA (a) and 200mA (b) applied current levels are shown. In (a) the wavelength flatness is 1.6dB, and in (b) the wavelength flatness is 3.7dB. This shows a trend similar to the theoretical wavelength flatness; as the applied current is increased, the wavelength flatness decreases. The fluctuations in power are due to the tunable laser used in the experiment and other effects such as Fabry-Perot reflections, AR coating quality, etc.**

Since the Drude model was used to calculate the wavelength flatness, there are discrepancies in attenuation level and wavelength flatness between the calculations and the measurements since it does not predict attenuation as accurately as the Soref model. However, the Soref model can not be used to predict the wavelength flatness since it is only valid at a wavelength of 1.55μm. Soref's model is only valid at this one wavelength since it was derived from analytical data of the effects of impurity doping on the optical properties of silicon, measured at 1.55μm. The Soref model could be improved by analyzing these effects at different wavelengths. Without this, the Drude model is an important tool in predicting attenuation changes with wavelength and the degree of wavelength flatness with injected current level.

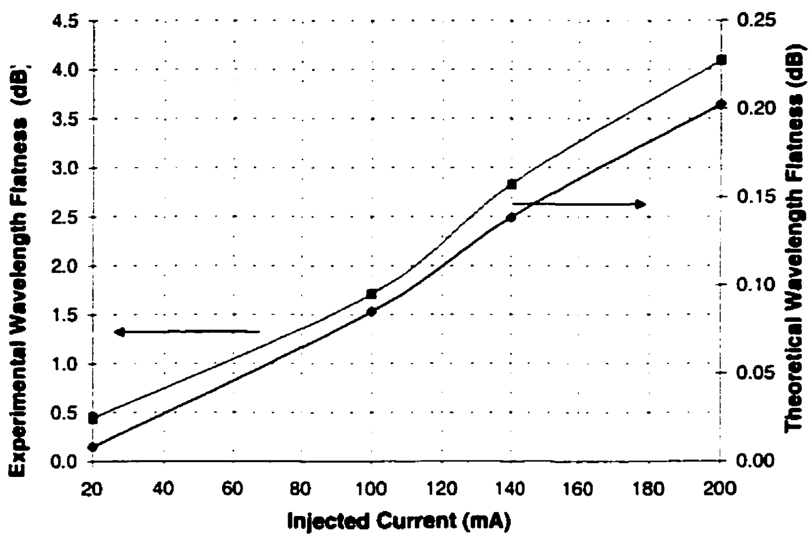


**Figure 3-11: Wavelength flatness vs. injected current level for experimentally measured devices and theoretical calculations. The experimental data follows the same upward trend as the theoretical data. The Drude model is thus useful in predicting a wavelength flatness trend with increasing injected current.**

### 3.3.3 Attenuation Characteristics

The attenuation with applied current was modeled for these devices using the method developed in Chapter 2. The change in attenuation level with applied current for the 4.25 and 5.75 μm separated diodes are shown in Figure 3-12 and Figure 3-13, respectively. These curves have been normalized to show the attenuation characteristics and therefore do not reflect the insertion losses of the devices. Also shown in these plots are the theoretical attenuation curves, based on the intrinsic region widths shown for a 1cm long device with a doping concentration of $1\text{x}10^{18}/\text{cm}^3$. These can only serve as a guide since many parameters such as the doping concentration, doping profile, and device length were unknown.

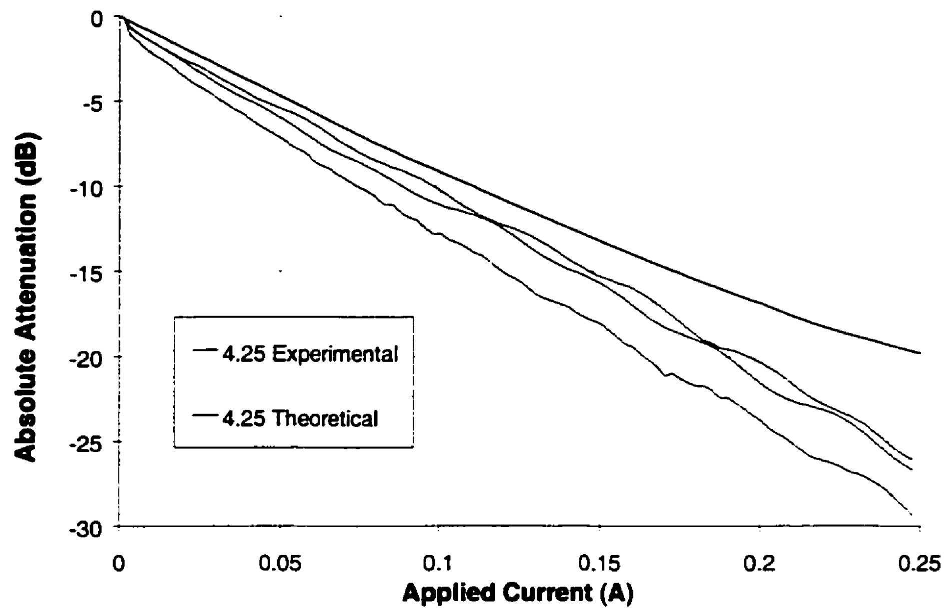


**Figure 3-12: Measured attenuation vs. applied current for three experimental devices with diodes marked at 4.25μm spacing. Also shown is the theoretically calculated attenuation curve. Notice the theoretical curve only reaches about 20dB of attenuation with 250mA of applied current, where the experimental devices reach attenuation levels of over 25dB.**

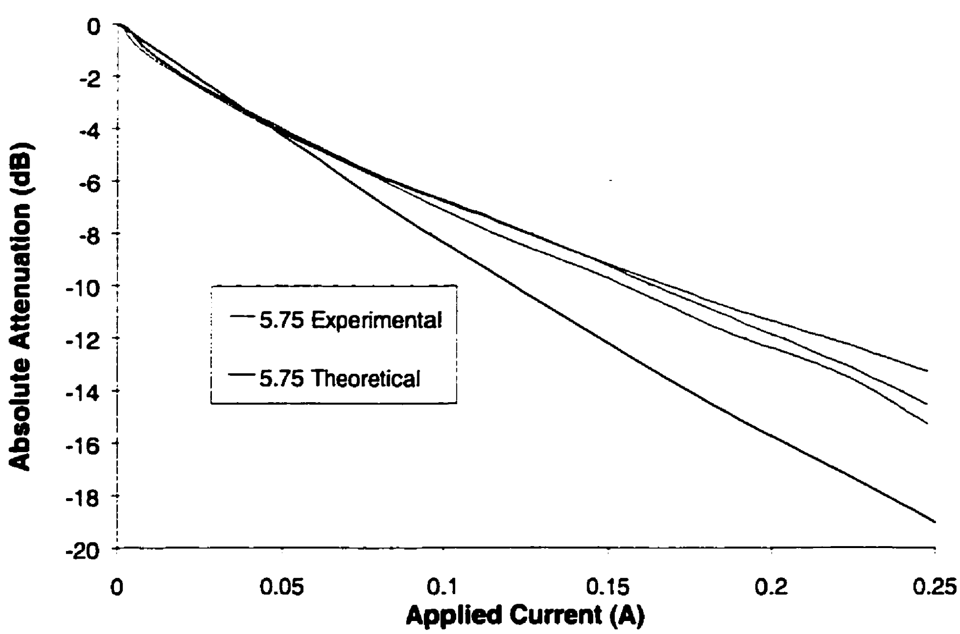


**Figure 3-13: Measured attenuation vs. applied current for three experimental devices with diodes marked at 5.75μm spacing. Also shown is the theoretically calculated attenuation curve. Notice in this case the theoretical curve reaches 19dB of attenuation with 250mA of applied current, where the experimental devices only reach attenuation levels of about 14dB.**

The theoretical curve for the 4.25μm separated diodes is above the experimental curves and the theoretical curve for the 5.75μm separated diodes is below the experimental curves. It is not fully understood why this occurs, however it is know that the attenuators with different diode spacings were not fabricated on the same wafer; the process may have changed between the two attenuator types. The 4.25μm intrinsic region width may actually be narrower than indicated and the 5.75μm intrinsic region width may be wider than indicated. Looking at the experimental curves, it is clear from Figure 3-12 and Figure 3-13 that the attenuation level for a given applied current increases as the intrinsic region width is decreased. This is in agreement with the theory provided in section 2.4.4.

Since the exact device dimensions and doping conditions were unknown, many parameters were varied in determining the best and worst-case scenarios in terms of attenuation characteristics. This is discussed in the next section.

#### *3.3.3.1 Tolerance Analysis – Attenuation Characteristics*

The device attenuation characteristics are dependent on a large number of variables. Unfortunately, a device with good attenuation characteristics as a result of closely spaced diodes will have high insertion losses, and vice-versa. Many of the same parameters that were varied in the insertion loss tolerance analysis were varied again since they also have an effect on the attenuation characteristics. The same manufacturing tolerances were applied here as were in the insertion loss tolerance analysis; ±0.2μm. Table 7 and Table 8 show results of calculations performed to determine the change in attenuation level at 200mA of applied current.

**Table 7: Attenuation characteristics tolerance analysis – best case scenario**

| *Parameter* | *Amount Changed* | *Effect (dB)* |
|---|---|---|
| Ridge Width | -0.2μm | +2.3 |
| Slab Height | +0.2μm | +1.0 |
| Intrinsic Region Width | -0.2μm | +0.3 |
| Device Length | +1mm | +0.2 |

**Table 8: Attenuation characteristics tolerance analysis - worst case scenario**

| *Parameter* | *Amount Changed* | *Effect (dB)* |
|---|---|---|
| Ridge Width | +0.2μm | -2.3 |
| Slab Height | -0.2μm | -1.0 |
| Intrinsic Region Width | +0.2μm | -0.3 |
| Device Length | -1mm | -0.3 |

The important parameters considered in the tolerance analysis of the device attenuation characteristics are those which affect the shape of the optical mode and the overlap of the optical mode with the distribution of free-carriers. These parameters are the waveguide ridge width, the slab height, and the intrinsic region width. The length of the active region was also an important factor in the device's attenuation characteristics and was also considered.

The first parameter considered in this tolerance analysis was the slab height. As observed in Chapter 2, decreasing the slab height will decrease the amount of mode energy in the slab region of the waveguide and therefore decrease the overlap of the optical mode and the free-carrier distribution. This is given in equation 2.57,

$$A = 10 \cdot \log(e^{-\delta\alpha z}), \tag{3.8}$$

where $\alpha$ s the attenuation coefficient in cm$^{-1}$, $A$ is the amount of attenuation in dB, $z$ is the length of the device and $\delta$ is the amount of overlap between the optical mode and carriers. Decreasing the amount of optical power in the slab region of the waveguide will decrease the overlap and therefore have the effect of decreasing the attenuation for a given amount of applied current. Theoretically, a 0.2μm decrease in slab height would cause a decrease in attenuation of 1.0dB for both intrinsic region widths of 5.75μm and 4.25μm. Similarly, a 0.2μm increase in slab height would cause an increase in attenuation of 1.0dB for both intrinsic region widths.

The width of the waveguide ridge will also effect the mode shape and therefore the percentage of overlap with the distribution of free-carriers. It was calculated that for a 0.2μm decrease in ridge width there is a corresponding increase in attenuation of 2.3dB for both intrinsic region widths of 4.25μm and 5.75μm. This increase in attenuation occurs because as the ridge width is decreased, the amount of mode energy in the slab region of the waveguide increases and therefore increases the amount of mode energy overlapping with the free-carrier distribution. It was also calculated that if the ridge width is increased by 0.2μm, the amount of mode energy in the slab region decreases and the attenuation decreases by 2.3dB for both intrinsic region widths.

The width of the intrinsic region will not affect the shape of the optical mode, however it will affect the overlap of the optical mode with the free-carrier distribution. According to equation 2.55 and 2.56, the change in absorption coefficient is inversely proportional to the intrinsic region width. Therefore, as the intrinsic region width is decreased the attenuation will increase as can be seen from equation 3.8. Theoretically, if the intrinsic region width is decreased by 0.2μm, there will be an increase in attenuation of 0.3dB for both starting widths of 4.25μm and 5.75μm.

The last parameter to be considered is the length of the active region. Equation 3.8 predicts that as the device length is increased, the attenuation will increase with applied current. Since the device length was unknown, a 1mm tolerance was added to this parameter. It was calculated that an increase in length of 1mm will cause an increase in attenuation of 0.2dB for both 4.25μm and 5.75μm intrinsic region widths. Also, a decrease in length of 1mm will cause a decrease in attenuation of 0.3dB for both intrinsic region widths.

Many of the changes analyzed could occur simultaneously, causing an increase or decrease in the overall attenuation with applied current. The critical parameter to control in terms of attenuation characteristics, is the processing of the waveguide shape in the attenuating region of the device since the effect of ridge width and slab height have the greatest effects on the attenuation. The best case scenario would lead to a relative increase in attenuation with applied current of 3.8dB. The worst case scenario would lead to a relative decrease in attenuation with applied current of 3.9dB.

### 3.3.4 Current Voltage Characteristics

The current versus voltage plots for the devices with diodes placed 4.25μm and 5.75μm apart are shown in Figure 3-14 and Figure 3-15, respectively.

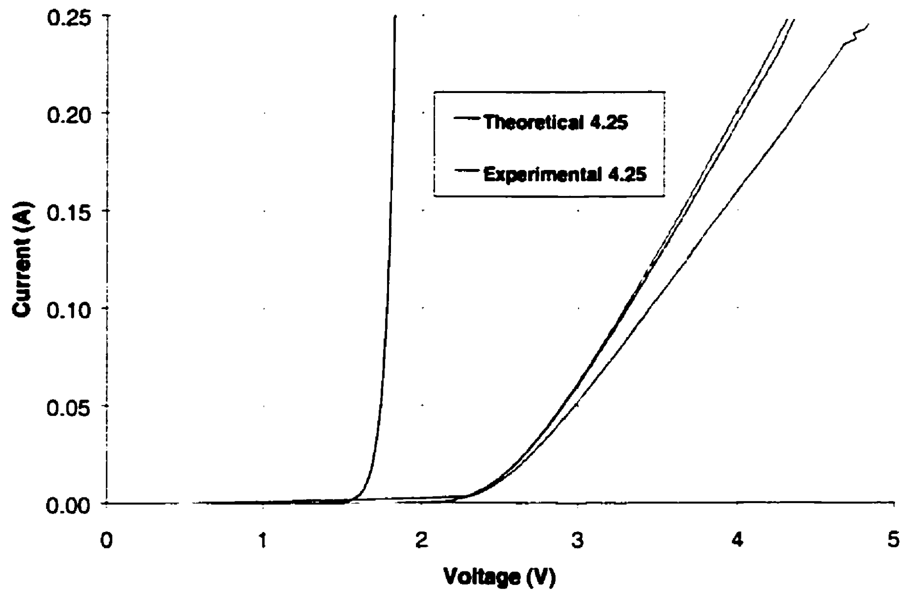


**Figure 3-14: I-V curves for experimental devices with diodes placed 4.25μm apart. Also shown is the theoretical IV curve. The difference in knee voltage and internal resistance between the theoretical and experimental curves are due to the device's contact potential and series resistance**

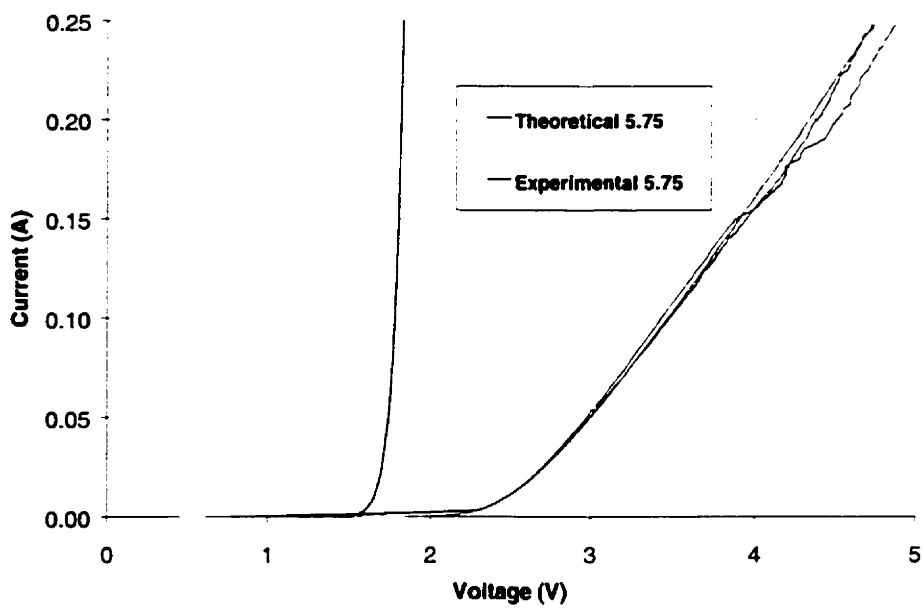


**Figure 3-15: I-V curves for experimental devices with diodes placed 5.75μm apart. Also shown is the theoretical IV curve.**

The deviations of the experimental curves from theory are mainly contributions from the series resistance and where the knee voltage occurs. The series resistance arises from voltage drops outside the depletion regions between the intrinsic region and the heavily doped P and N regions. The knee voltage, or the point at which the current increases rapidly with increasing voltage is theoretically equal to the contact potential for heavily doped junctions. There are a number of factors causing the knee voltage to deviate from this contact potential. Both the series resistance and the knee voltage are important parameters to discuss since they affect the device's power consumption

Realistically, there exists a resistance in the P and N regions of a PIN diode, which were previously assumed to be neutral. With an applied forward voltage, most of the voltage drop appears across the transition regions, however a small drop in voltage occurs in the neutral P and N regions on either side. Theoretically this voltage drop has been assumed to be very small and has been ignored. If the cross-sectional width of the doped sections are small compared to their area and the doping concentration is sufficiently high, the resistance will be low and only a negligible drop in voltage will occur in these areas. However, this is not always the case and a large resistance can arise under forward bias. The voltage drop across the transition regions depends on the forward current, which in turn is dictated by the voltage across the junction. As the forward bias increases, the series resistance will also increase. A large series resistance can be avoided by heavy doping of the P and N regions and decreasing the junction cross-sectional area. The series resistance for each device was calculated by taking the inverse slope of the linear region of the data in Figure 3-14 and Figure 3-15 is shown in Table 9 below. Uncertainties were calculated by variations in the slopes of the measured curves.

**Table 9: Calculated series resistance for experimental devices**

| *Device* | *Series Resistance (Ω)* |
|---|---|
| 4.25 – A | 9.47 ± 0.012 |
| 4.25 – B | 7.18 ± 0.004 |
| 4.25 – C | 6.99 ± 0.003 |
| 5.75 – A | 9.6 ± 0.13 |
| 5.75 – B | 8.81 ± 0.051 |
| 5.75 – C | 8.74 ± 0.063 |

The PIN diode equation (equation 2.52) derived in Chapter 2 is dependant on a large number of factors which can affect the knee voltage. Variations in the diode surface area, doping concentration, and diffusion length will cause the knee voltage to change. Furthermore, the diffusion coefficient and diffusion length are dependant on the free-carrier mobilities and lifetimes, respectively, which may be less than ideal due to traps or crystal defects. Theoretically, the effect of changing the surface area and the diffusion lengths by the manufacturing tolereances discussed is very small. An increase in surface area of $+0.4\mu m^2$ only leads to an increase in knee voltage of 0.07V and a 30% increase in doping concentration only results in an increase of 0.01V.

The type of contact will also affect the knee voltage. The theoretical model assumed ohmic contacts between the doped regions and the metal contact pads, with minimal resistance and no tendency to rectify signals. However, such an ideal metal-semiconductor contact can be difficult to fabricate and a Schottky barrier junction often results. A Schottky barrier junction includes a termination of the semiconductor crystal, in which the exterior of the semiconductor material contains surface states due to incomplete covalent bonds leading to charges at the metal-semiconductor interface. A thin oxide layer can also exist between the silicon and the metal which the electrons must tunnel through. This extra contact potential must be overcome before current flows through the diode and therefore will also increase the knee voltage.

### 3.3.5 Power Consumption

The power consumption versus attenuation plots for the devices with diodes placed 4.25μm and 5.75μm apart are shown in Figure 3-14 and Figure 3-15, respectively.

Since the experimental devices have a series resistance and knee voltage larger than the contact potential, their power consumption is much greater than the theoretical calculation. Reducing the series resistance and knee voltage by the methods discussed in the previous section can reduce the power consumption.

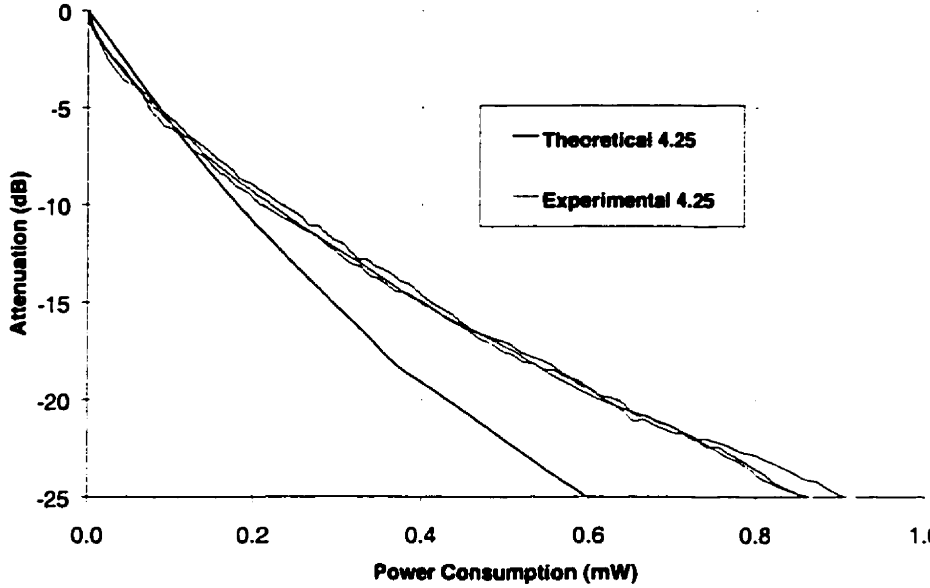


**Figure 3-16: Power consumption vs. attenuation for experimental devices with diodes placed 4.25μm apart. Also shown is the theoretical power consumption.**

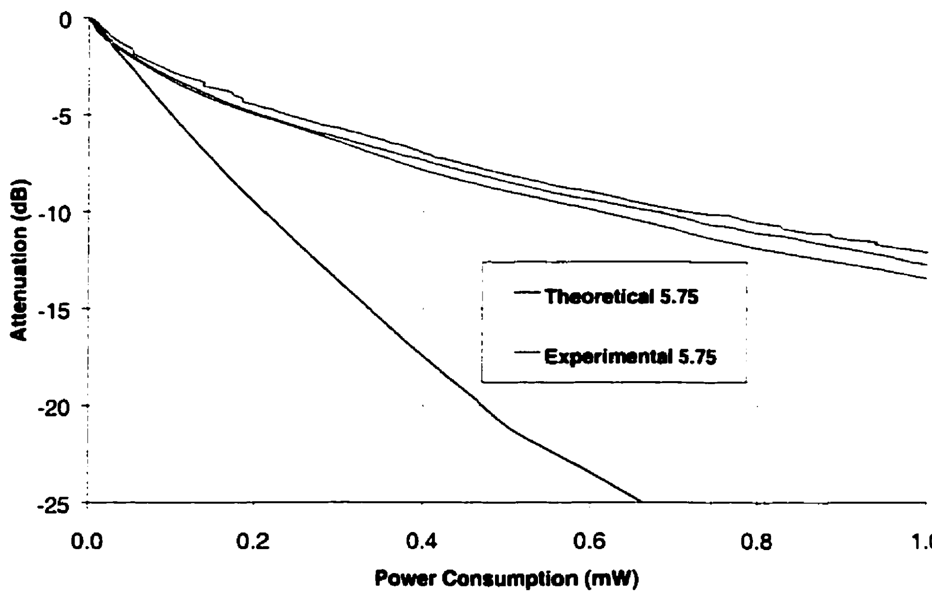


**Figure 3-17: Power consumption vs. attenuation for experimental devices with diodes placed 5.75μm apart. Also shown is the theoretical power consumption. The experimental power consumption is higher than the theoretical due to a higher knee voltage and series resistance.**

Along with the series resistance and knee voltage, there are three main factors affecting the device power consumption. These are the width of the intrinsic region, the doping concentration of the P and N sections, and the active region length. These were discussed in section 2.4.4 of Chapter 2. The difference between the theoretical curves and the experimental power consumption curves suggest that the devices were longer than expected, and/or the intrinsic region was wider than expected, and/or the doping concentration was heavier than expected, or a combination of these. Table 10 shows the relative change in power consumption with a change in these parameters at an attenuation level of 15dB for both intrinsic region widths.

**Table 10: Power consumption tolerance analysis**

| *Parameter* | *Amount Changed* | *Effect (W)* |
|---|---|---|
| Intrinsic Region Width | -0.2μm | -0.02 |
| Doping Concentration | -30% | -0.01 |
| Attenuation Region Length | -1mm | -0.05 |

From these calculations it can be seen that the most critical parameter to control the power consumption is the device length, however as the length is increased the attenuation will increase as well. Reducing the series resistance and knee voltage by the methods discussed will also keep power consumption low.

### 3.3.6 Response Time

The response time can be modeled by a first-order low-pass filter with a step response [2]:

$$g(t) = u(t)\left[1 - e^{-2B_r t}\right] \qquad 3.9$$

where $B_r$ is the 3dB electrical bandwidth of the device and $u(t)$ is the unit step function which is 1 for $t \geq 0$ and 0 for $t < 0$. The response time $t_r$ of the device is defined as the time interval between $g(t) = 0.1$ and $g(t) = 0.9$. Therefore, if $B_r$ is given in MHz, then the rise time in nanoseconds is:

$$t_r = \frac{350}{B_r}. \qquad 3.10$$

The 3dB bandwidth was found by adjusting the driving frequency of the function generator to find the roll-off in attenuation level as the frequency was increased. The response shape is shown in Figure 3-18.

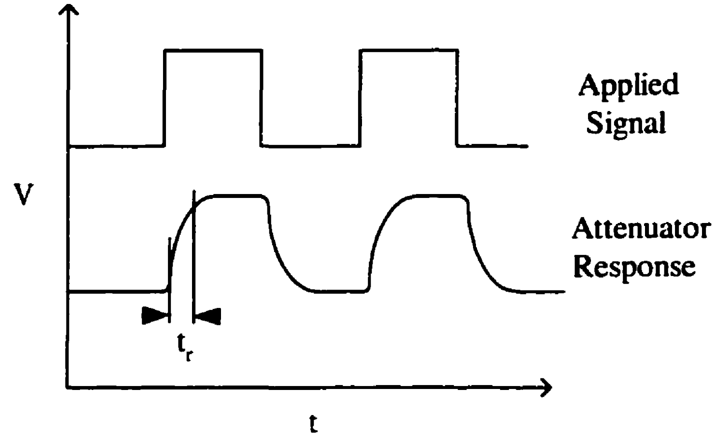


**Figure 3-18: Response curve of attenuator to a square pulse. The response time, $t_r$, is measured as the time taken for the device to increase in attenuation level from 10% to 90%.**

The 3dB bandwidth was measured to be 1.3 ± 0.05MHz for an increase in attenuation level of 25dB. The level of 25dB was chosen since at this level there is a sufficient difference in optical power level between the on state and the off state. This bandwidth remained constant for input power levels ranging from 1 to 10mW. Using equation 3.10, these devices have a response speed of 269 ± 10ns. Theoretically, the speed of response is limited to the slowest carrier lifetime. The slowest theoretical speed is the recombination lifetime at low carrier densities, which is 100ns as discussed in Chapter 3. Therefore, the experimental devices have some impurities forming traps or crystal defects causing scattering which increase the lifetime. This response time is not expected to change at higher power levels; however a heat sink or thermoelectric cooler may be required as the number of photon-electron interactions increase.

## *3.4 Experimental Device Summary*

In the analysis of these experimental devices, it is important to remember that only the waveguide dimensions of the experimental devices were known with some precision; all other parameters were either inferred from physical measurements or performance characteristics. The doping concentration was assumed to be in the range of $1\times10^{18}/cm^3$ to $1\times10^{20}/cm^3$; enough to give sufficient attenuation without excessive off-state losses. The intrinsic region width was only given as the CAD drawing width and not an exact measurement. The device length was measured by the length of the metallization, however this measurement is not certain since it is the doping which controls the length. The metallization could have covered more or less of the doped section length than what was measured. Furthermore, the two different intrinsic region widths were fabricated on different wafers and it was unknown if or how the process had changed between them.

All things considered, the experimental devices did validate the theory developed in Chapter 2. Several important parameters were found that affect the device's behavior, such as careful facet preparation to minimize insertion losses. The difference in attenuation level between the device with a 4.25μm intrinsic region and the device with a 5.75μm intrinsic region showed that the attenuation increases with decreasing intrinsic region width. The response time was close to that which was calculated. The wavelength flatness showed the same characteristics as predicted by the Drude model. Overall, the experimental devices did show that the PIN diode is a feasible device as an electronically controlled variable attenuator.

***References***

[1] F.L. Pedrotti, L.S. Pedrotti, "Introduction to Optics", Prentice Hall, New Jersey, 1993, ISBN 0-13-501545-6, pp. 397-401.

[2] B.E.A. Saleh, M.C. Teich, "Fundamentals of Photonics," John Wiley and Sons, Inc, New York, 1991, ISBN 0-471-83965-5, pp. 654.

# 4 Conclusions and Suggestions for Future Work

## *4.1 Conclusions of Results*

A free-carrier absorption attenuator was designed for low losses and low power consumption with the ability to achieve high attenuation levels. The theory developed in the design of the theoretical device was challenged by the comparison of the experimental devices' performance. Comparison was difficult since the exact specifications of many of the parameters of the experimental devices was unknown. However, the results gained were useful in proving the theory and gaining insight into the challenges of experimental analysis.

There were two main goals in the theoretical design of the free-carrier absorption attenuator. Optically, the goal was to minimize off-state losses incurred due to geometry of the device. Electrically, the goal was to minimize off-state losses incurred by the doped sections while maximizing the on-state attenuation characteristics and minimizing power consumption. The maximum loss budget was set at 1dB, the minimum attenuation at 20B, and the maximum power consumption at 1W.

Low-loss coupling from a small core fibre to a single mode waveguide was achieved through the use of adiabatic tapers. The input and output sections were larger than the single mode waveguide conditions would allow to increase the coupling efficiency between the small core fibre and the waveguide. Adiabatic tapers narrowed the top waveguide ridge down such that the device would operate single mode. A 300μm linear taper resulted in the lowest loss of less than 0.006dB. By using tapers, the total coupling loss was decreased from 0.74dB to 0.34dB while still allowing single mode propagation.

There were several trade-offs in the electrical design. Loss due to free-carrier absorption is at a minimum when the intrinsic region width is large, the active region length is short, and the doping concentration of the P and N regions is low. On the other hand, the attenuation level is maximized when the intrinsic region width is small, the active region is long, and the doping concentration is high. Also, power consumption is minimized when the intrinsic region width is small, the active region is long, and the doping concentration is low. The dimensions were tailored to meet the design specifications by reaching a compromise between insertion loss, attenuation and power consumption. This lead to a final active region design having an intrinsic region width of 7μm, length of 1cm and doping concentration of $10^{18}/cm^3$ in the P and N regions. The optimal design is shown in Figure 4-1.

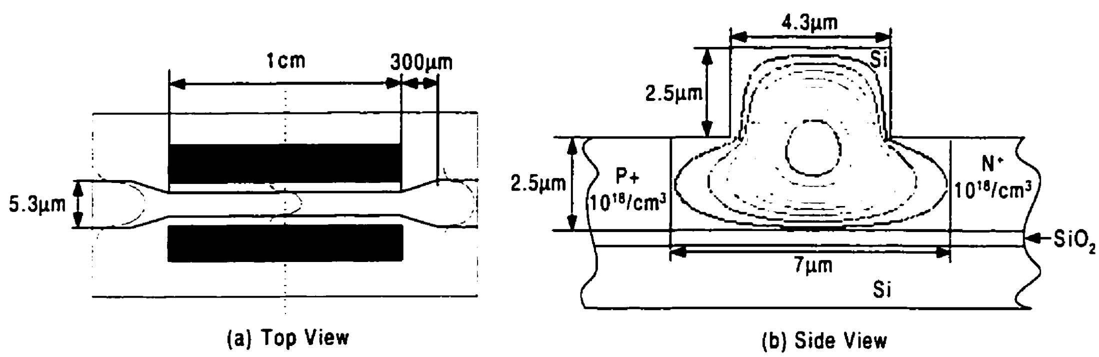


**Figure 4-1: Best device design for 1W on-state power consumption, attenuation range of 20dB, and off-state loss of 1dB.**

Facet preparation was important in reducing the insertion losses of the experimental devices. It was found that the loss could be decreased on average by more than 1.03dB by AR coating the facets, and that polishing the end facets after cleaving did not lead to any significant decrease in insertion loss. Gluing glass caps on the top and bottom of the device resulted in easier handling during polishing, coupling, and probing of the device.

When the calculated overlap integrals and experimental data pertaining to the effect of changing the interface width with coupling loss was compared, it was found that the experimental and theoretical curves followed the same trend. Both curves showed that as the waveguide interface width increased, the insertion loss due to mode mismatch decreased.

The experimental devices verified that as the intrinsic region width decreased, the insertion loss increased. The difference in insertion loss between the diode with an intrinsic region width of 4.25μm was on average 0.2dB greater than that of the diode with an intrinsic region width of 5.75μm. Theoretical tolerance analysis showed that the intrinsic region width and shape of the mode in the active region had the largest effect on off-state losses. The critical parameter to control in device fabrication is the doping process and etching of the centre rib.

The response time of the experimental devices was 269 ± 10ns, close to the theoretical time of 100ns. The discrepancy could be due to the presence of impurities causing traps or defects causing scattering, both of which would slow down the free-carriers and increase the response speed. If response time is critical, proper steps should be taken during processing to minimize defects and impurities.

Device attenuation was modeled using both the Drude model and the Soref model of free-carrier absorption. Since the Soref model gives a much higher attenuation with a given injected current level and more accurately predicted the experimental results, it was concluded that this model was more useful in determining attenuation with injected current level.

Wavelength flatness predicted by the Drude model was tested in a qualitative sense by the attenuation versus wavelength data of the experimental devices. The attenuation increases with wavelength, and the slope of this dependency increases with increased injection current level. This showed that the Drude model is an important tool in predicting attenuation changes with wavelength and degree of wavelength flatness with injected current level.

The attenuation characteristics of the experimental devices proved that the attenuation level increased with decreasing intrinsic region width. The devices with an intrinsic region width of 4.25μm had an attenuation level on average of 10dB higher than those devices with an intrinsic region width of 5.75μm. Theoretical tolerance analysis was also performed for the attenuation characteristics, and it was found that the critical parameter to control in device processing is the etching of the ridge in the active region since changes in the waveguide shape have the greatest effect on the maximum attenuation level.

The current voltage characteristics of the experimental devices showed the presence of a series resistance and a contact potential. The series resistance can be reduced by increasing the doping concentration of the P and N regions and/or by decreasing the junction cross-section area. These changes, however, would lead to higher off-state loss and lower maximum attenuation. Both the series resistance and the knee voltage increase the power consumption. Reducing these can keep power consumption down.

The free-carrier based waveguide attenuator has many good characteristics which makes it a promising candidate for many applications in optical communication systems. Advantages include low PDL, a powerless off-state and a fast response time. Disadvantages are high power consumption and wavelength sensitivity.

## *4.2 Suggestions for Future Work*

The opportunity remains to carry this work further. The optimal device design arrived at in Chapter 2 could be fabricated and tested against the theory developed and compared to the devices tested in this work. This would give better insight into the effects of the device geometry since this would accurately be known. The effect of optical input power on device performance could be investigated; looking in particular at operation under high input powers (>1W). Packaging and assembly considerations as well as environmental testing would also be needed to determine if the attenuator is a legitimate product.